JETP Letters, Vol. 78, No. 5, 2003, pp. 261–266. From Pis'ma v Zhurnal Éksperimental'noĭ i Teoreticheskoĭ Fiziki, Vol. 78, No. 5, 2003, pp. 707–712.

New Experimental Limits on Heavy Neutrino Mixing in ^{8}B-Decay Obtained with the Borexino Counting Test Facility¶

H. O. Back[a], M. Belata[b], A. de Bari[c], T. Beau[d], A. de Bellefon[d], G. Bellini[e, 1], J. Benziger[f], S. Bonetti[e], C. Buck[g], B. Caccianiga[e], L. Cadonati[f], F. Calaprice[f], G. Cecchet[c], M. Chen[h], A. Di Credico[b, 4], O. Dadoun[d, 7], D. D'Angelo[i, 4], A. Derbin[j, 6, 10], M. Deutsch[k, †], F. Elisei[l], A. Etenko[m], F. von Feilitzsch[i], R. Fernholz[f], R. Ford[f, 3], D. Franco[e], B. Freudiger[g, 4, 7], C. Galbiati[f, 4], F. Gatti[n], S. Gazzana[b, 4], M. G. Giammarchi[b], D. Giugni[e], M. Goeger-Neff[i], A. Goretti[b, 2], C. Grieb[i], C. Hagner[a], E. Harding[f], F. X. Hartmann[g], G. Heusser[g], A. Ianni[b, 4], A. M. Ianni[f, 4], H. De Kerret[d], J. Kiko[g], T. Kirsten[g], V. Kobychev[b, 8], G. Korga[e, 9], G. Korschinek[i], Y. Kozlov[m], D. Kryn[d], J. Lamblin[d], M. Laubenstein[b, 5], C. Lendvai[i, 4, 7], E. Litvinovich[m], P. Lombardi[e, 4], I. Machulin[m], S. Malvezzi[e], J. Maneira[h], I. Manno[o], D. Manuzio[n], G. Manuzio[n], F. Masetti[l], A. Martemianov[m, †], U. Mazzucato[l], K. McCarty[f], E. Meroni[e], L. Miramonti[e], M. E. Monzani[e], V. Muratova[j, 6], P. Musico[n], L. Niedermeier[i, 4, 7], L. Oberauer[i], M. Obolensky[d], F. Ortica[l], M. Pallavicini[n, 4], L. Papp[e, 9], L. Perasso[e], A. Pocar[f], R. S. Raghavan[p], G. Ranucci[e, 2], A. Razeto[b], A. Sabelnikov[e], C. Salvo[n, 3], R. Scardaoni[e], D. Schimizzi[f], S. Schoenert[g], H. Simgen[g], T. Shutt[f], M. Skorokhvatov[m], O. Smirnov[j, 11], A. Sonnenschein[f], A. Sotnikov[j], S. Sukhotin[m], V. Tarasenkov[m], R. Tartaglia[b], G. Testera[n], D. Vignaud[d], R. B. Vogelaar[a], V. Vyrodov[m], M. Wojcik[q], O. Zaimidoroga[j], and G. Zuzel[q]

[a] *Virginia Polytechnic Institute and State University, Blacksburg, VA, 24061-0435 USA*
[b] *L.N.G.S. SS 17 bis Km 18+910, I-67010 Assergi(AQ), Italy*
[c] *Dipartimento di Fisica Nucleate e Teorica Università di Pavia, 6 I-27100 Pavia, Italy*
[d] *Laboratoire de Physique Corpusculaire et Cosmologie, 75231 Paris Cedex 05, France*
[e] *Dipartimento di Fisica Università di Milano, 16 I-20133 Milano, Italy*
[f] *Dept. of Physics, Princeton University, Jadwin Hall, Princeton, NJ, 08544-0708 USA*
[g] *Max-Planck-Institut fuer Kernphysik, Postfach 103 980 D-69029, Heidelberg, Germany*
[h] *Dept. of Physics, Queen's University, Stirling Hall, Kingston, Ontario K7L 3N6, Canada*
[i] *Joint Institute for Nuclear Research, 141980 Dubna, Russia*
[j] *Technische Universitaet Muenchen, E15 D-85747 Garching, Germany*
[k] *Dept. of Physics, Massachusetts Institute of Technology, Cambridge, MA, 02139 USA*
[l] *Dipartimento di Chimica Università di Perugia, I-06123 Perugia, Italy*
[m] *RRC Kurchatov Institute, Moscow, 123182 Russia*
[n] *Dipartimento di Fisica Università and I.N.F.N. Genova, 33 I-16146 Genova, Italy*
[o] *KFKI-RMKI, Konkoly Thege ut 29-33 H-1121 Budapest, Hungary*
[p] *Bell Laboratories, Lucent Technologies, Murray Hill, NJ, 07974-2070 USA*
[q] *M. Smoluchowski Institute of Physics, Jagellonian University, PL-30059 Krakow, Poland*
e-mail: derbin@mail.pnpi.spb.ru, smirnov@lngs.infn.it

Received July 7, 2003

If heavy neutrinos with mass $m_{\nu_H} \geq 2m_e$ are emitted in the decays of ^{8}B in the Sun, then $\nu_H \longrightarrow \nu_L + e^+ + e^-$ decays should be observed. In the present work, the results of background measurements with the Borexino Counting Test Facility have been used to obtain bounds on the number of these decays. As a result, new limits on the coupling $|U_{eH}|^2$ of a massive neutrino in the range of 1.1 MeV to 12 MeV have been derived ($|U_{eH}|^2 \leq 10^{-3}$–10^{-5}). The obtained limits on the mixing parameter are stronger than obtained in previous experiments using nuclear reactors and accelerators. © *2003 MAIK "Nauka/Interperiodica".*

PACS numbers: 13.35.Hb; 14.60.Pq; 26.65.+t

1. Introduction. If neutrinos have mass, then a heavier one can decay to a lighter one [1, 2]. The simplest detectable decay modes in the framework of an extended standard model (SM) are radiative decay $\nu_H \longrightarrow \nu_L + \gamma$ and decay into an electron, a positron, and a light neutrino:

$$\nu_H \longrightarrow \nu_L + e^+ + e^-. \qquad (1)$$

The e^+e^- decay mode, which becomes possible if $m_{\nu_H} \geq 2m_e$, results from a W exchange diagram, as shown in Fig. 1. Because atmospheric, solar, and reactor neutrino oscillations have been discovered, this heavy neutrino cannot be connected with one of the three mass eigenstates forming the three known neutrino flavors. Moreover, this fourth neutrino has to be coupled in the $(e - W)$ vertex with U_{eH} and G_F constants, but it cannot be coupled (or coupled very weakly) to the Z boson.

Many extensions of the SM predict the existence of a sterile neutrino: a singlet fermion can be a mirror neutrino, goldstino in SUSY, modulino of the superstring theories, or a bulk fermion related to the existence of extra dimensions [3]. In general, the sterile neutrino may have an arbitrary mass and can mix with all three active neutrinos.

The decay rate for this mode in the center of mass system of the decaying neutrino is [1, 2]

$$\Gamma_{\text{c.m.}} \cong \frac{G_F^2}{192\pi^3} m_{\nu_H}^2 |U_{eH}|^2 |U_{eL}|^2 h\left[\frac{m_e^2}{m_{\nu_H}^2}\right], \qquad (2)$$

where U_{eH} is the mixing parameter of the heavy neutrino to the electron, $G_F^2/192\pi^2 = 3.5 \times 10^{-5}$ MeV^{-5} s^{-1}, $h[m_e^2/m_{\nu_H}^2]$ is the phase-space factor calculated in [2], and one can $|U_{eL}|^2 \simeq 1$. In the SM, the probability of the e^+e^- mode is much higher than for radiative decay: e.g., for $m_{\nu_H}^2 = 5$ MeV (and $|U_{eH}|^2 \sim 1$) one obtains $\tau(\nu_H \longrightarrow \nu_L e^+e^-) \approx 10$ s against $\tau(\nu_H \longrightarrow \nu_L\gamma) \approx 10^{10}$ s.

The possible decay of massive antineutrinos from a reactor $\nu_H \longrightarrow \nu_L + e^+ + e^-$ has been studied in [4–8]; the latter gives the strongest restrictions on the mixing parameter $|U_{eH}|^2 < (0.3\text{–}5) \times 10^{-3}$ in the mass region $m_{\nu_H} \sim 1.1\text{–}9.5$ MeV). Accelerator experiments performed in a beam of neutrinos from π and K decays constrain the coupling of still heavier neutrinos (see [9] and references therein). A heavy neutrino with mass up to 15 MeV can be produced in the Sun in the reaction $^8\text{B} \longrightarrow {}^8\text{Be} + e^+ + \nu$ and can then decay in flight. An upper limit $|U_{eH}|^2 \sim 10^{-5}$ was obtained by considering data on the positron flux in interplanetary space [10].

More restrictive bounds were obtained from SN1987A data [11–14]. On the other hand, Big Bang nucleosynthesis requires a fast decay branch ([11–14] and references therein). This fast mode could be realized by the decay of the heavy particle into a Goldstone boson and a light neutrino. Obviously, this decay mode should be as slow as about 500 s, which is the time needed for the particle to reach the detector.

Borexino, a real-time liquid scintillator (LS) detector for low-energy neutrino spectroscopy, is near completion in the underground laboratory at Gran Sasso (see [15, 16] and references therein). The main goal of the detector is the direct measurement of the flux of ^{7}Be solar neutrinos of all flavors via neutrino–electron scattering. In this paper, we present the results of the search for the $\nu_H \longrightarrow \nu_L + e^+ + e^-$ decay inside the active volume of the prototype of the Borexino detector.

2. Experimental setup and results of measurements. *2.1. Brief description of the detector.* The prototype of the Borexino detector, the Counting Test Facility (CTF), was constructed with the aim of testing the key concept of Borexino, namely, the possibility to purify a large mass of liquid scintillator at the level of contamination for U and Th of a few units 10^{-16} g/g. In this simplified scaled-down version of the Borexino detector, a volume of LS is contained by a transparent inner nylon vessel 2 m in diameter mounted at the center of an open structure that supports 100 phototubes (PMT) [17]. The whole system is located within a cylindrical tank (11 m in diameter, 10 m in height) that contains 1000 tons of ultra-pure water, which provides a 4.5 m shielding against neutrons originating from the rock and against external γ rays from PMTs and other construction materials.

The upgrade of the CTF, called CTF-II, was equipped with a carefully designed muon veto system. It consists of 2 rings of 8 PMTs each, installed at the bottom of the tank. The radii of the rings are 2.4 and 4.8 m. Muon veto PMTs look upward and have no light concentrators. The muon veto system was optimized to have a negligible probability of registering scintillation

¶This article was submitted by the authors in English.
† Deceased.
[1] Spokesmen.
[2] Project manager.
[3] Operational manager.
[4] Task manager.
[5] GLIMOS.
[6] On leave of absence from St. Petersburg Nuclear Physics Inst., Gatchina, Russia.
[7] Marie Curie fellowship at LNGS.
[8] On leave of absence from Institute for Nuclear Research, MSP 03680, Kiev, Ukraine.
[9] On leave of absence from KFKI-RMKI, Konkoly Thege ut 29-33 H-1121 Budapest, Hungary.
[10] Address for correspondence: St. Petersburg Nucl. Phys. Inst., Gatchina, 188350 Russia.
[11] Address for correspondence: Joint Inst. for Nucl. Research, Dubna, 141980 Russia.

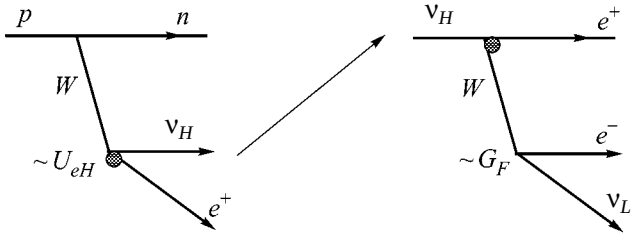

Fig. 1. Feynman graphs describing the appearance ($^8B \longrightarrow {}^8Be + e^+ + \nu_H$) and decay ($\nu_H \longrightarrow \nu_L + e^+ + e^-$) of a heavy neutrino.

events in the so-called "neutrino energy window" from 250 to 800 keV. The behavior of the muon veto at higher energies has been specially studied for the previous work [18]. The energy dependence of the probability $\eta(E)$ of identification of an event with energy E in the LS by the muon veto was also calculated by a ray-trace Monte Carlo (MC) method. The calculated function was adjusted to correctly reproduce the experimental measurements with the ^{226}Ra source. Detailed reports on the CTF have been published [19–22].

2.2. Detector calibration. The energy of an event in the CTF detector is defined using the total collected charge from all PMTs. The coefficient linking the event energy and the total collected charge is called light yield (or photoelectron yield). At low energies, the phenomenon of "ionization quenching" violates the linear dependence of the light yield versus energy [23]. The deviations from the linear law can be taken into account by the ionization deficit function $f(k_B, E)$, where k_B is Birks' constant. For the calculations of the ionization quenching effect for the PXE (phenylxylylethane, $C_{16}H_{18}$) scintillator, we used the KB program from the CPC library [24]. The ionization quenching effect leads to a shift in the position of the peak of the energy deposit of the gammas on the energy scale calibrated using electrons. For example, the position of the two 1022-keV annihilation gamma quanta in CTF-II corresponds to the 860-keV energy deposit of the electron. A check of the MC-simulation code was performed by modeling ^{40}K data. The detector energy and spatial resolution were studied with radioactive sources placed at different positions inside the active volume of the CTF. Typical spatial 1σ resolution is 10 cm at 1 MeV. The studies also showed that the total charge response of the CTF detector can be approximated by a Gaussian curve. For energies $E \geq 1$ MeV (which are of interest here), the relative resolution can be expressed as $\sigma_E/E = \sqrt{3.8 \times 10^{-3}/E + 2.3 \times 10^{-3}}$ (E is in MeV) [25] for events uniformly distributed over the detector's volume.

The energy dependence on the collected charge becomes nonlinear for energies $E \simeq 5$ MeV because of the saturation of the ADCs used. In this region, we use

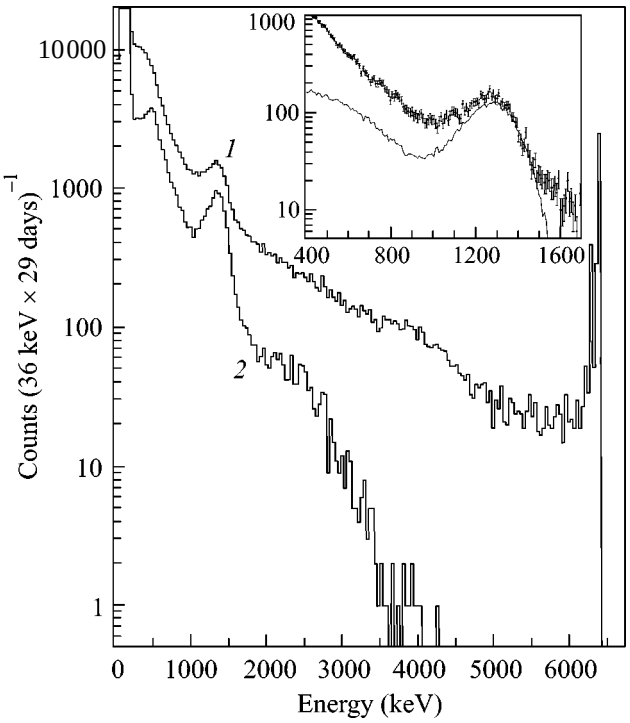

Fig. 2. Background energy spectra of the 4.2 ton BOREXINO CTF-II detector measured during 29.1 days: (*1*) spectrum without any cuts; (*2*) with muon veto applied. In the inset, the simulated response function for external ^{40}K gammas is shown together with the experimental data.

only the observation of nonobservation of candidate events; hence, the mentioned nonlinearity does not influence the result of the analysis.

2.3. Data selection. In this analysis, 29.1 days of the August–September 200 data-taking period were used (Fig. 2). In our analysis we used 29.1 days of data from CTF-II (Fig. 2). The major part of the CTF background at low energies is induced by the activity of ^{14}C, ^{85}Kr, and ^{39}Ar [26]. At higher energies, the background is mainly induced by muons. The spectrum without any cuts (spectrum *1*) is presented on the top. The second spectrum was obtained by applying the muon cut, which suppressed the background rate by up to two orders of magnitude, mainly at high energy.

The peak at 1.36 MeV, present in both spectra, is due to ^{40}K decays outside the scintillator, mainly in the ropes supporting the nylon sphere. The peaklike structure at ~6.2 MeV is caused by saturation of the electronics by high-energy events. As one can see from Fig. 2, muon identification cuts remove most of the background induced by muons in such a way that there are no events with energy higher than 4.5 MeV. In our analysis, we used only this fact.

3. Neutrino flux and deduced limits. In order to obtain bounds on the parameters $|U_{eH}|^2$ and m_ν, the spectrum obtained by CTF has to be compared with the

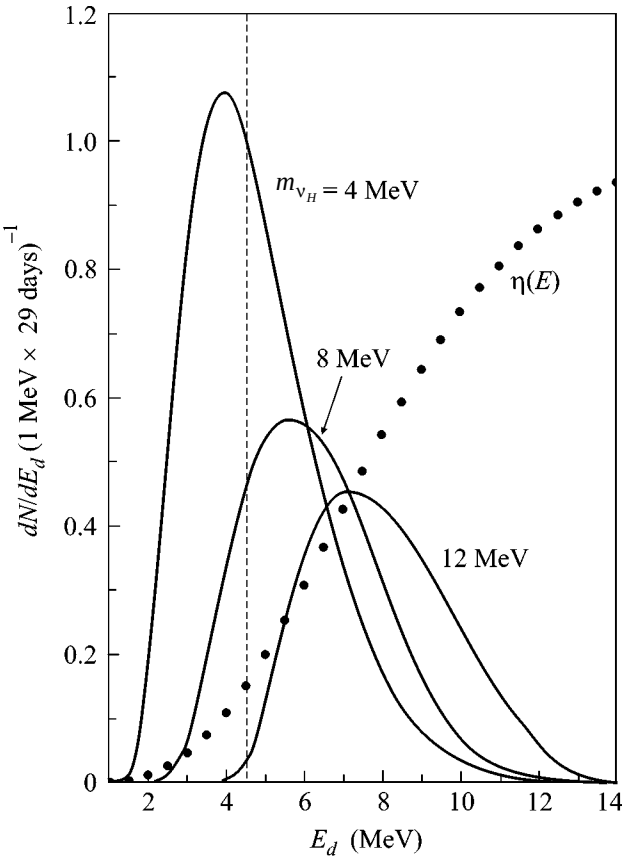

Fig. 3. The expected spectra of signals due to $\nu_H \longrightarrow \nu_L + e^+ + e^-$ decay for different neutrino masses m_{ν_H} = 4, 8, 12 MeV. The corresponding mixing parameters ($|U_{eH}|^2$ = 1.8×10^{-4}, 3.9×10^{-5}, 1.3×10^{-4}) lead to the CTF-II count rate 2.44/29.1 d for $E_d \geq 4.5$ MeV. The probability $\eta(E)$ of identification of an event in the LS by the muon veto is shown by the point curve.

energy spectrum expected for ν_H decay. To calculate this, one has to know the flux of heavy neutrinos through the detector $\Phi(E_\nu)$, the kinetic energy of the created e^+e^- pairs, and the response function of CTF to two-annihilation quanta.

The emission of a heavy neutrino, coupled to an electron, in the reaction of β^+ decay of ^{8}B is suppressed by the mixing parameter $|U_{eH}|^2$ and a phase-space factor:

$$\Phi_{m_\nu}(E_\nu) = |U_{eH}|^2 \sqrt{1 - \left(\frac{m_{\nu_H}}{E_\nu}\right)^2}\, \Phi_{^8\mathrm{B}}(E_\nu), \qquad (3)$$

where E_ν is the total energy of the heavy neutrino ($\Phi_{m_\nu}(E_\nu) = 0$ for $E_\nu < m_\nu$). For calculation, we used the neutrino spectrum from ^{8}B decay $\Phi_{^8\mathrm{B}}(E_\nu)$ given in [27].

A heavy neutrino emitted in the Sun can decay on its flight to Earth. The energy spectrum of neutrinos reaching the detector is given by

$$\Phi(E_\nu) = \exp(-\tau_f/\tau_{\mathrm{c.m.}})\Phi_{m_\nu}(E_\nu), \qquad (4)$$

where $1/\tau_{\mathrm{c.m.}} = \Gamma_{\mathrm{c.m.}}$ defined by (2). τ_f is the time of flight in c.m.s.:

$$\tau_f = \frac{m_{\nu_H}}{E_\nu}\frac{L}{\beta c}. \qquad (5)$$

Here, $L = 1.5 \times 10^{13}$ cm is the average distance between the Sun and the Earth and $\beta = \sqrt{1 - (m_\nu/E_\nu)^2}$.

The double differential distribution for energy e and emission angle θ of the light neutrino ν_L for the c.m.s. was obtained in [2]:

$$\frac{dN_{\nu_L}}{d\epsilon d\cos\theta} = \Gamma_{\mathrm{c.m.}}(f_1 + \xi|\mathbf{P}|f_s\cos\theta), \qquad (6)$$

where $f_1(\epsilon, m_{\nu_H})$ and $f_s(\epsilon, m_{\nu_H})$ are complex functions defined in [2], $\xi = +1(-1)$ for $\nu_H(\overline{\nu_H})$, and $|\mathbf{P}| = \beta$ is the polarization of the ν_H.

The total laboratory energy of the e^+e^- pair, $E = E_\nu - E_{\nu_L}$, is connected with ϵ as follows:

$$E = E_\nu(1 - (\epsilon/m_\nu)(1 + \beta\cos\theta)). \qquad (7)$$

In c.m.s., the energy e of the emitted neutrino is restricted by the value $\epsilon \leq \epsilon_{\min} = (m_{\nu_H}^2 - 4m_e^2)/2m_{\nu_H}$, which corresponds to the emission angle

$$(\cos\theta)_{\min} = (1/\beta)(\epsilon_{\min}(1 - E/E_\nu) - 1). \qquad (8)$$

The differential spectrum of the e^+e^- pair is obtained by integration of (6) over cos(θ) (or ϵ) and account of Eq. (7):

$$\frac{dn}{dE}(E, E_\nu) = \int_{(\cos\theta)_{\min}}^{1} \frac{dN_{\nu_L}}{d\epsilon d\cos\theta} d\epsilon d\cos\theta. \qquad (9)$$

For a given energy of heavy neutrino E_ν, the energy E of the e^+e^- pair is restricted to the interval

$$E_\nu\left[1 - \frac{1+\beta}{2}\left(1 - \frac{4m_e^2}{m_{\nu_H}^2}\right)\right] \leq E \leq E_\nu. \qquad (10)$$

Integrating over neutrino energy up to the end-point energy Q_0, one can obtain the spectrum of total e^+e^--pair energy:

$$\frac{dN}{dE}(E) = \Gamma_{\mathrm{c.m.}}|U_{eH}|^2\frac{m_\nu}{c}\int_{2m_e}^{Q_0}\frac{dN}{dE}(E, E_\nu)\frac{\Phi(E_\nu)}{E_\nu}dE_\nu. \qquad (11)$$

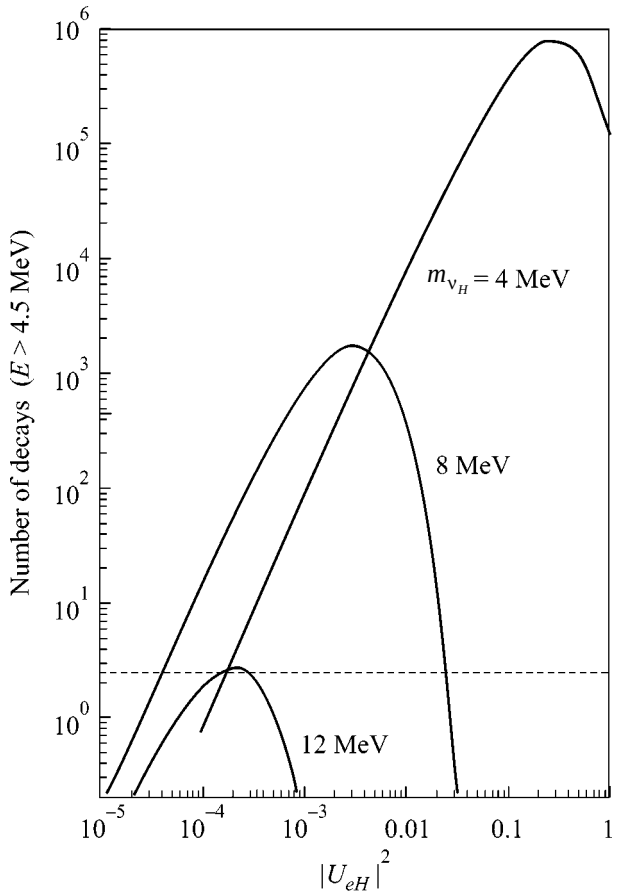

Fig. 4. Counting rates of CTFII as a function of the mixing parameter $|U_{eH}|^2$ for different values of heavy neutrino mass. The level 2.44 events /29.1 d is shown by the dotted line.

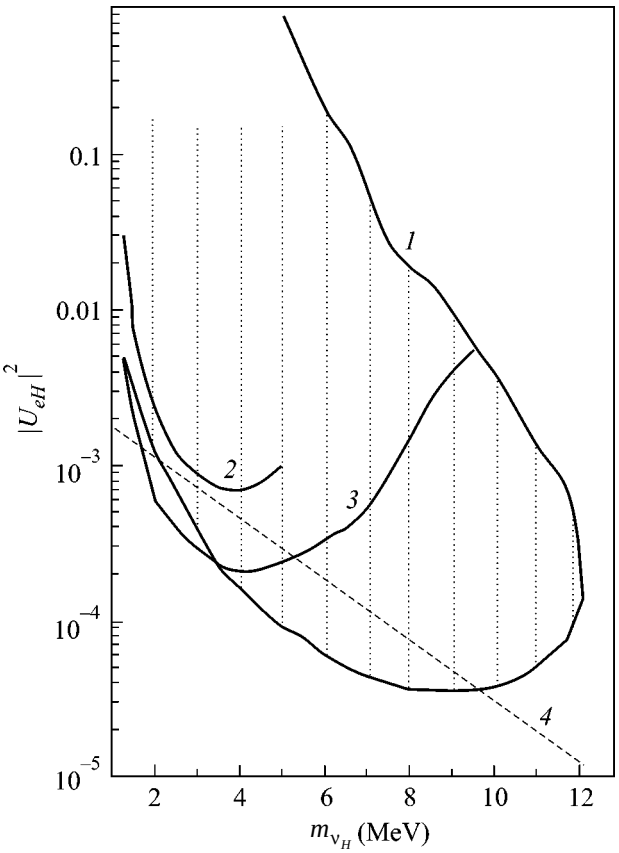

Fig. 5. Limits on the mixing parameter $|U_{eH}|^2$ as a function of neutrino mass m_ν (90% c.l.). (*1*) present work excludes values of $|U_{eH}|^2$ and m_ν inside dotted region; (*2*, *3*) upper limits from reactor experiments on the search for $\nu_H \longrightarrow \nu_L + e^+ + e^-$ decay [7, 8]; (*4*) upper limits from $\pi \longrightarrow e + \nu$ decay [29].

The Monte Carlo method was used in order to simulate the CTF response $S(E)$ to two-annihilation quanta. The gamma–electron showers were followed using the EGS-4 code [28], taking into account the ionization quenching factor and the dependence of the registered charge on the distance from the detector's center. The obtained response function looks like the sum of two Gaussian peaks at energies 860 and 430 keV, with dispersion ~70 keV and relative intensities ~3 : 1. Peaks have low energy tails containing ~10% of the total intensity.

Taking into account the probability of suppression of the high-energy events by the muon veto $(1 - \eta(E))$ [18] and the detector response function $R(E, E')$ with σ_E defined as in Section 2.2, the energy spectrum of signals in the detector is obtained by convolutions (11) over $S(E)$ and $R(E, E')$:

$$\frac{dN}{dE}(E) = VT(1-\eta(E)) \times \int_{E-3\sigma}^{E+3\sigma} \left(\int_{E_d-2m_e}^{E_d} \frac{dN}{dE'}(E')S(E_d-E')dE' \right) R(E_d, E)dE_d. \quad (12)$$

Here, V is the volume of the detector and T is the time of measurement. The obtained spectra for various values of m_ν are shown in Fig. 3. The shape of (12) differs from (11): it is shifted by about 870 keV to higher energy and it is suppressed at higher energies by muon veto (e.g., $\eta(5\text{ MeV}) = 0.2$, Fig. 3).

As mentioned above, we used in analysis only the fact that there are no events with $E \geq 4.5$ MeV. In accordance with the recommendation for Particle Data Group [9], the statistical maximum number of events for zero events observed is 2.44 (at 90% confidence level).

The relation

$$S_{\text{int}}(m_\nu, |U_{eH}|) = \int_{4.5\text{ MeV}}^{Q_0} \frac{dN}{dE_d}(E_d) \leq 2.44 \quad (13)$$

leads to bounds on parameters $|U_{eH}|^2$ and m_ν. The dependence of the number of counts on the parameters of $|U_{eH}|^2$ and m_ν is

$$S_{\rm int}(m_\nu, |U_{eH}|) \sim m_\nu^6 |U_{eH}|^4 \exp(-\text{const} \cdot m_\nu^6 |U_{eH}|^2). \quad (14)$$

Functions $S_{\rm int}(|U_{eH}|)$ are shown on Fig. 4 for different values of m_ν. The experiment is not as sensitive for low $|U_{eH}|^2$ (due to the low probability of ν_H decay) as for high values of $|U_{eH}|^2$, because in this case ν_H decays during its flight from the Sun. The maximum $S_{\rm int}(|U_{eH}|^2)$ for fixed m_ν and E_ν corresponds to $|U_{eH}|^2 = 2(|U_{eH}|^2 \tau_{\rm c.m.})/\tau_f$, where $\tau_{\rm c.m.} = 1/\Gamma_{\rm c.m.}$ and τ_f are defined by (2) and (5).

The region of restricted values of parameters $|U_{eH}|^2$ and m_ν is shown in Fig. 5 in comparison with the results of reactor experiments [7, 8] and the search for massive neutrinos in the $\pi^+ \longrightarrow e^+\nu_e$ decay in accelerators [29]. For the neutrino mass region 4–10 MeV, the obtained limits on the mixing parameter are stronger than those obtained in previous experiments using nuclear reactors and accelerators.

4. Conclusion. Using the extremely low background and large mass of the Borexino Counting Test Facility, new limits on the mixing parameter $|U_{eH}|^2$ of a massive neutrino in the range of mass 1.1 MeV to 12 MeV have been set. These limits are more than one order of magnitude stronger than these obtained in previous experiments using nuclear reactors.

REFERENCES

1. F. Boehm and P. Vogel, *Physics of Massive Neutrinos* (Cambridge Univ. Press, Cambridge, 1987).
2. R. E. Shrock, Phys. Rev. D **24**, 1275 (1981).
3. P. C. de Holanda and A. Yu. Smirnov, hep-ph/0211264.
4. P. Vogel, Phys. Rev. D **30**, 1505 (1984).
5. L. Oberauer, F. Von Feilitzsch, and R. L. Mossbauer, Phys. Lett. B **198**, 113 (1987).
6. V. I. Kopeĭkin, L. A. Mikaelyan, and S. A. Fayans, Pis'ma Zh. Éksp. Teor. Fiz. **51** (2), 75 (1990) [JETP Lett. **51**, 86 (1990)].
7. A. V. Derbin, A. V. Chernyĭ, L. A. Popeko, *et al.*, Pis'ma Zh. Éksp. Teor. Fiz. **57**, 755 (1993) [JETP Lett. **57**, 768 (1993)].
8. C. Hagner, M. Altman, F. von Feilitzsch, *et al.*, Phys. Rev. D **52**, 1343 (1995).
9. D. E. Groom *et al.* (Particle Data Group), Eur. Phys. J. C **15**, 1 (2000); K. Hagiwara, K. Hikasa, K. Nakamura, *et al.*, Phys. Rev. D **66**, 010001 (2002).
10. D. Toussaint and F. Wilczek, Nature **289**, 777 (1981).
11. L. Oberauer, C. Hagner, G. Raffelt, and E. Rieger, Astropart. Phys. **1**, 377 (1993).
12. A. D. Dolgov, S. H. Hansen, G. Raffelt, and D. V. Semikoz, Nucl. Phys. B **580**, 331 (2000).
13. A. D. Dolgov, Phys. Rep. **370**, 333 (2002).
14. G. G. Raffelt, hep-ph/0208024.
15. G. Alimonti *et al.* (Borexino Collab.), Astropart. Phys. **18**, 1 (2002).
16. H. O. Back *et al.* (Borexino Collab.), Phys. Lett. B **525**, 29 (2002).
17. G. Ranucci *et al.*, Nucl. Instrum. Methods Phys. Res. A **333**, 553 (1993).
18. H. O. Back *et al.* (Borexino Collab.), Phys. Lett. B **563**, 35 (2003).
19. G. Alimonti *et al.* (Borexino Collab.), Nucl. Instrum. Methods Phys. Res. A **406**, 411 (1998).
20. G. Alimonti *et al.* (Borexino Collab.), Phys. Lett. B **422**, 349 (1998).
21. G. Alimonti *et al.* (Borexino Collab.), Astropart. Phys. **8**, 141 (1998).
22. G. Alimonti *et al.* (Borexino Collab.), Nucl. Instrum. Methods Phys. Res. A **440**, 360 (2000).
23. J. B. Birks, Proc. Phys. Soc. London, Sect. A **64**, 874 (1951).
24. J. M. Los Arcos and F. Ortiz, Comput. Phys. Commun. **103**, 83 (1997).
25. O. Ju. Smirnov, Instrum. Exp. Tech. **46**, 327 (2003).
26. H. O. Back *et al.* (Borexino Collab.), Phys. Lett. B **563**, 35 (2003).
27. J. N. Bahcall, H. Pinsonneault, and S. Basu, Astrophys. J. **555**, 990 (2001).
28. W. R. Nelson, H. Hirayama, and D. W. O. Rogers, *The EGS4 Code System* (1985), SLAC-265.
29. D. A. Bryman *et al.*, Phys. Rev. Lett. **50**, 1546 (1983).

JETP Letters, Vol. 78, No. 5, 2003, pp. 267–271. Translated from Pis'ma v Zhurnal Éksperimental'noĭ i Teoreticheskoĭ Fiziki, Vol. 78, No. 5, 2003, pp. 713–717.

Correlation or Decoherence? Quantum Beats of Atomic Inversion in a Resonant Coherent Field

N. K. Solovarov

Zavoisky Physical-Technical Institute, Kazan Scientific Center, Russian Academy of Sciences, Sibirskiĭ trakt 10/7, Kazan 29, Tatarstan, 420029 Russia

e-mail: solovar@kfti.knc.ru

Received June 30, 2003; in final form, July 29, 2003

It is shown that the standard reduction procedure (i.e., the calculation of the density matrix of the observable subsystem from the density matrix of a closed quantum system) bringing about decoherence corresponds to the limiting approximation, where the unobservable subsystem is assumed to be in the stationary state with minimum information (infinite temperature). An approximate set of interrelation (correlation) equations for the density matrices of the subsystems is derived. It is shown that the correlation of atom and field can be manifested as the inversion beats of a two-level atom in the known experimental scheme of resonator QED. Experimental observation of such beats would indicate that the observable subsystem (atom) generally conserves information about quantum coherence of the unobservable subsystem (field). © *2003 MAIK "Nauka/Interperiodica".*

PACS numbers: 03.65.Ta; 42.50.Pq

An old problem of the reduction of a quantum mechanical system with simultaneous decoherence of its observable subsystem is being discussed now in quantum optics and quantum informatics [1–8].

Decoherence is considered as the transition of the observable quantum system from the superposition state to the statistical-mixture state as a result of the interaction with the macroscopic environment [3, 6–8]. In this formulation, the decoherence problem is equivalent to the known problem of quantum relaxation theory [9, 10] describing the dynamics of a quantum system interacting with a thermostat and encounters no fundamental difficulties. The general difference is that the state of environment is not specified in the problem of decoherence. For definiteness, this decoherence will be called macroscopic decoherence.

We discuss decoherence (and its existence as a physical phenomenon [1, 3–5]) under reduction, i.e., separation of the observable subsystem from the closed (Hamiltonian) quantum system with unitary dynamics. Mathematical reduction, i.e., the algorithm of calculating the reduced density operator of the observable subsystem from the density operator of the closed system, was axiomatically introduced by von Neumann [11]. This reduction amounts to calculating the partial trace of the density operator of the total system over the unobservable subsystem (projection onto the observable subsystem). Since this operation is nonunitary, a portion of information is lost, so that the quantum nature of irreversibility [3, 5, 12], as well as the completeness of information readout from a quantum computer in quantum informatics [8], is now under discussion.

The experimental separation of the reduction or intrinsic decoherence [13] from the macroscopic decoherence is expected in the observation of the dynamics of a simple composite quantum system [3], which can be considered as closed in the time intervals under consideration. The resonant QED scheme [6] is considered as one of the successful experimental schemes for investigations of the dynamics of quantum coherence and decoherence in a simple closed system. In this work, the known theoretical analysis of this experimental scheme is revised with emphasis on the correlation between the subsystems of the closed system. The reduction decoherence under consideration is shown to follow from the implicit use of the approximation of the given "extremely incoherent" state of the unobservable subsystem in calculations.

Let us analyze the physical content of the standard (Neumann) reduction [9–11], which postulates that, if the dynamics of a closed system (for definiteness, atom + field) is described by the density operator $\hat{\rho}(t)$, the dynamics of the observable subsystem (atom) is described by the reduced density operator $\hat{\rho}_a(t) = \mathrm{Tr}_f\hat{\rho}(t)$.

First, the calculation of the trace of the observable $\hat{A}$ of a quantum system in the basis of its energy eigenstates is equivalent, except for a constant factor N equal to the space dimension (the number of eigenstates), to the calculation of the quantum mean value of this

observable for the case where the quantum system is in the state with minimum information:

$$\mathrm{Tr}\hat{A} \equiv N\langle \hat{A}\rangle_{\min} = N\mathrm{Tr}\hat{\rho}_{\min}\hat{A}, \quad (1)$$

where $\hat{\rho}_{\min} = (1/N)\hat{1}$ is the density operator of the quantum system in the state with minimum information (state with infinite temperature) and $\hat{1}$ is the unity operator [9, 11]. The state $\hat{\rho}_{\min}$ physically corresponds both to the equiprobable location (with probability $1/N$) of the quantum system in any eigenstate and to the absence of quantum coherence (nonzero off-diagonal elements of the density matrix [10]) in the system.

According to the definition [9], the density matrix $\hat{\rho}(t)$ is the information operator for a closed quantum system. The calculation of the trace over the unobservable subsystem is mathematically identical with the partial average of this operator for the case where the field is in the state with minimum information (except for the normalization constant):

$$\hat{\rho}_a(t) = \mathrm{Tr}_f\hat{\rho}(t) \equiv N_f\mathrm{Tr}_f\hat{\rho}(t)\hat{\rho}'_{f\min}, \quad (2)$$

where $\hat{\rho}'_{f\min} = (\hat{1}_a \otimes \hat{\rho}_{f\min})$ is the extended (to the entire system space) density operator of a field in the state with minimum information and $\hat{1}_a$ is the unity operator in atomic space. Thus, according to Eq. (2), the calculation of the reduced density operator of an atom is equivalent to the assumption that a field is in a stationary state with minimum information (infinite temperature). This assumption is used only for the reduction and not for calculating the dynamics of a closed system [i.e., $\hat{\rho}(t)$].

Analysis of the correlation between the density operators of the subsystems of a closed quantum system leads to the same conclusion [14, 15]. The atom and field are equivalent subsystems of a closed system. Let us assume that the density operator of a closed system can be approximately represented in terms of the direct product of the correlated density operators (labeled the subscript C) of the subsystems $\hat{\rho}(t) \approx (\hat{\rho}_{aC}(t) \otimes \hat{\rho}_{fC}(t))$ (the exact equality is generally valid only for noninteracting subsystems [9, 10]). Multiplying this expression on the right by $\hat{\rho}_{fC}(t)$ or $\hat{\rho}_{aC}(t)$ and calculating the trace over the field or atomic subsystems, one easily arrives at the set of approximate coupled equations [14, 15]

$$\hat{\rho}_{aC}(t) \approx \frac{\mathrm{Tr}_f\hat{\rho}(t)\hat{\rho}'_{fC}(t)}{\mathrm{Tr}_{af}\hat{\rho}(t)\hat{\rho}'_{fC}(t)}, \quad (3)$$

$$\hat{\rho}_{fC}(t) \approx \frac{\mathrm{Tr}_a\hat{\rho}(t)\hat{\rho}'_{aC}(t)}{\mathrm{Tr}_{af}\hat{\rho}(t)\hat{\rho}'_{aC}(t)}. \quad (4)$$

The right-hand sides of Eqs. (3) and (4) are the quantum averaging (normalized to unity) of the density operator $\hat{\rho}(t)$ of the closed system over one of the subsystems. If the state of the unobservable subsystem (e.g., field) $\hat{\rho}'_f(t)$ is defined from the external physical conditions, the state of the observable subsystem (atom), which is correlated with the former state, is also defined according to Eq. (3). Therefore, each of Eqs. (3) and (4) can be treated as a generalized definition of reduction or the approximation of a given state of an unobservable subsystem under reduction. In particular, when a field is in the $\hat{\rho}_{f\min}$ state, this definition coincides with the generally accepted Neumann definition of reduction (2). When a field in the n-photon eigenstate at a measurement time t (i.e., the field-density operator is the projector onto this state, so that $\hat{\rho}_f(t) = \hat{P}_{fn} = |n\rangle\langle n|$), Eq. (3) coincides with the reduction definition used in the quantum optics theory of nondemolition measurements of photons [16, 17].

When the state of one of the subsystems is given, the set of Eqs. (3) and (4) is generally inconsistent. This inconsistency reflects the approximate character of separation of one of the interacting subsystems. Indeed, according to Eqs. (3) and (4), any possible algorithm of reduction is equivalent to the change $\hat{\rho}(t) \longrightarrow \hat{\rho}_a(t) \otimes \hat{\rho}_f(t) = \hat{\rho}_R(t)$, i.e., to an approximate representation of the closed quantum system as two quasi-independent subsystems with known dynamics, or to transition to a new "reduced" closed system with the density operator $\hat{\rho}_R(t)$. Does the reduction algorithm (i.e., the corresponding change) correspond to the initial assumption that the quantum system is closed? Or in mathematical terms: What error is introduced to the assumed exact state $\hat{\rho}(t)$ under the change $\hat{\rho}(t) \longrightarrow \hat{\rho}_R(t)$?

The Neumann reduction algorithm obviously includes the following physical inconsistency. On the one hand, the quantum system is considered closed. On the other hand, the state of an unobservable subsystem is implicitly considered stationary and is specified by the infinite temperature. To closely approximate $\hat{\rho}_R(t)$ to $\hat{\rho}(t)$, the reduction algorithm can be improved by the following two methods:

(i) to physically justify the postulated state of the unobservable subsystem in each particular case (thermostat in the quantum relaxation theory [9, 10]; one of the eigenstates in the theory of quantum nondemolition measurements of photons [16, 17]; or a certain physically appropriate state) and to use one of Eqs. (3) and (4);

(ii) to use the self-consistent successive approximation procedure to find the correlated density operators of the subsystems from Eqs. (3) and (4) with the zero approximation, e.g., in the form of the reduced Neumann density operators of the subsystems [14, 15].

The second method is mathematically general but is often physically excessive. However, in any case, the

state (density operator) of an observable subsystem correlates with the state of an unobservable subsystem. In the standard Neumann reduction, it implicitly correlates with the maximally incoherent state (with zero quantum coherence!) of an unobservable subsystem, and, therefore, the reduction decoherence of an observable subsystem is postulated. The Neumann reduction algorithm is more justified if the properties of an unobservable subsystem are close to macroscopic and its state can be specified by high (infinite) temperature. However, in experiments, where both subsystems of a closed system are substantially quantum, it is necessary to take into account their correlation.

Let us discuss the possible manifestation of the correlation between the subsystems in the known experimental scheme of resonator QED. These experiments (see review [6]) study the dynamics of individual Rydberg atoms flying through the high-Q resonator whose eigenfrequency (ω) is in resonance with the transition between two neighboring Rydberg levels, excited and ground. The probability of observation of an atom in a certain state (excited or ground) is measured as a function of the properties of the electromagnetic field in the resonator, the time τ of flight of an atom through a resonator, the initial state, and the atomic flux intensity. In a high-Q resonator, the energy change between the atom and the photon field occurs during time interval τ.

These experiments are described by the exactly solvable Jaynes–Cummings model of a closed quantum system of a two-level atom interacting with the resonant single-mode quantized field in the rotating-wave approximation [18–20]. The model corresponds to the physical case where the source of the electromagnetic field in the ideal resonator is turned off at the time (taken as $t = 0$) when the atom enters the resonator and the nonstationary energy exchange between the atom and resonator field is considered. It is convenient to present the qualitative model results for a case where the atom entering the resonator is in the excited state. In this case, the probabilities of observing the atom leaving the resonator in the excited and ground states are determined as [6, 21]

$$\left.\begin{matrix} P_e(\tau) \\ P_g(\tau) \end{matrix}\right\} = \frac{1}{2}\sum_{n=0}^{\infty} p(n)[1 \pm \cos(\Omega_n \tau)], \qquad (5)$$

where $p(n)$ is the probability that the resonator field includes n photons at $t = 0$, $\Omega = \Omega_0$ is the Rabi quantum frequency corresponding to the frequency of atomic inversion oscillations in the vacuum ($n = 0$) resonator field, and $\Omega_n = \Omega\sqrt{n+1}$ is the corresponding Rabi frequency in the n-photon field. It is seen that, if $p(n)$ is a smooth function, n-photon contributions to Eq. (5) are dephased with increasing τ. As a result, the probabilities that the atom is in the excited and ground states are equal to each other, $P_e(\tau_{col}) \simeq P_g(\tau_{col}) \simeq 1/2$; i.e., the atomic inversion exhibits quantum collapse [22]. If $p(n)$ has a sharp maximum for $n = \bar{n}$, which makes the basic contribution of the form $p(\bar{n})[1 + \cos(\Omega\tau\sqrt{\bar{n}+1})]$ to $P_e(\tau)$, $P_e(\tau)$ can undergo periodic oscillations with the period $\tau_{rev} = 2\pi/\Omega\sqrt{\bar{n}+1}$ of the inversion revival [23]. Experiments on the observation of revival [21] are described under the assumption that the initial number of photons in the resonator obeys the Poisson distribution $p(n) = \exp(-\bar{n})(\bar{n}^n/n!)$ with the mean number $\bar{n}$ and standard deviation $\sqrt{\bar{n}}$. This distribution corresponds to two physically different states of photon field: a coherent state with the density operator $\hat{\rho}_{fc}(0) = |\alpha\rangle\langle\alpha|$ and the statistical mixture

$$\hat{\rho}_{fm}(0) = \exp(-|\alpha|^2)\sum_{n=0}^{\infty}(|\alpha|^{2n}/n!)|n\rangle\langle n|,$$

where $\bar{n} = |\alpha|^2$ in both cases [24]. According to Eq. (5), the calculated dynamics of atomic inversion is independent of the quantum coherence of field. It is this loss of the dependence of atomic inversion on the coherence properties of the field that represents the reduction decoherence discussed in the model under consideration. We emphasize that the complete decoherence of the atom does not occur for the initial coherent field state $\hat{\rho}_{fc}(0)$. The quantum coherence of the atom (dipole transition moment) is not identical zero [6, 23], but it is unobservable (immeasurable) in experiments with individual atoms.

In the experimental scheme under consideration with $\bar{n} \gg 1$, the interaction with a single atom in a relatively short time cannot change considerably the initial state of the photon field in the resonator. Therefore, the calculation of the reduced operator in the approximation of the stationary initial state of the field, rather than in the standard approximation of the infinite field temperature, is physically justified. Thus, the first method of improving the reduction algorithm for the atomic inversion dynamics will be used.

It is convenient to use the known solution of the Jaynes–Cummings resonant model [18, 19] in the form of the evolution operator $\hat{U}(t)$ determining the dynamics of the closed system [15, 25] as $\hat{\rho}(t) = \hat{U}(t)(\hat{\rho}_a(0) \otimes \hat{\rho}_f(0))\hat{U}^{\dagger}(t)$, where $\hat{\rho}_a(0)$ and $\hat{\rho}_f(0)$ are the initial density operators of the atom and field, respectively. Let the atom initially be in the excited state and the field in the state $\hat{\rho}_{fc}(0)$ or $\hat{\rho}_{fm}(0)$. In this case, calculating first the density operator of the system $\hat{\rho}(t)$ and then the density operator of the atom (reduced by the standard way) $\hat{\rho}_a(t) = \mathrm{Tr}_f\hat{\rho}(t)$ and writing the diagonal elements of the latter, one obtains the known result (5).

In contrast, we perform reduction according to Eq. (3) assuming that the field is either in the stationary

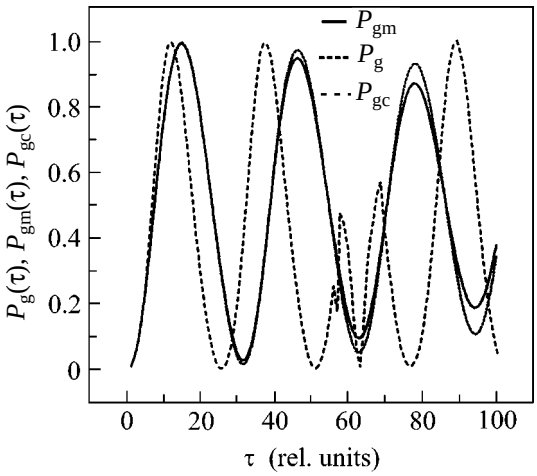

Probabilities of the observation of an atom in the ground state vs. the duration τ of its interaction with a resonator field: P_g for the standard reduction, P_{gc} in the approximation of a given coherent field in reduction, and P_{gm} in the approximation of a given field in the state of incoherent statistical mixture. Parameters are $|\alpha|^2 = 100$, $\omega = 0.1$, and $\Omega = 0.01$.

coherent state $\hat{\rho}_{fc}(0)$ or in the statistical mixture state $\hat{\rho}_{fm}(0)$. Then, the respective probabilities that the atom is in the ground state are equal to

$$\left.\begin{matrix} P_{gc}(\tau) \\ p_{gm}(\tau) \end{matrix}\right\} = \begin{cases} s_c(\tau)/[c_c(\tau) + s_c(\tau)] \\ s_m(\tau)/[c_m(\tau) + s_m(\tau)], \end{cases} \quad (6)$$

where

$$c_c(\tau) = \sum_{m,n=0}^{\infty} \frac{|\alpha|^{2(m+n)}}{m!n!} \cos[\omega\tau(m-n)] \times \cos(\Omega\tau\sqrt{m})\cos(\Omega\tau\sqrt{n}),$$

$$s_c(\tau) = \sum_{m,n=0}^{\infty} \frac{|\alpha|^{2(m+n+1)}}{m!n!\sqrt{m+1}\sqrt{n+1}} \cos[\omega\tau(m-n)] \times \sin(\Omega\tau\sqrt{m+1})\sin(\Omega\tau\sqrt{n+1}),$$

$$c_m(\tau) = \sum_{n=0}^{\infty} \frac{|\alpha|^{4n}}{(n!)^2} \cos^2(\Omega\tau\sqrt{n}),$$

$$s_m(\tau) = \sum_{n=0}^{\infty} \frac{|\alpha|^{4n+2}}{n!(n+1)!} \sin^2(\Omega\tau\sqrt{n+1}),$$

and the additional subscripts c and m indicate that reduction is performed in the approximation of the respective initial field states.

The figure shows the characteristic probabilities $P_g(\tau)$, $P_{gc}(\tau)$, and $P_{gm}(\tau)$ demonstrating qualitative differences in the calculated inversion dynamics that are caused by the use of an approximation of a given field in a reduction. It is seen that if a field is assumed to be in the statistical mixture state $\hat{\rho}_{fm}(0)$, the computational result differs from the standard result (5) only by a small weakening of the quantum collapse, i.e., by a retarding of the decrease in the amplitude of Rabi oscillations. This result is qualitatively clear: the implicit assumption about the infinite field temperature in the traditional reduction increases the relative weight of components Ω_n whose frequencies are far from the frequency of the $\Omega_{\bar{n}}$ component. Therefore, their dephasing is accelerated and the population inversion collapse proceeds rapidly.

The inclusion of field coherence in reduction leads to a qualitatively new inversion dynamics. Beats appear due to (as follows from Eqs. (6)) the superposition of oscillations that are additional to Ω_n, have frequencies $n\omega$, and characterize n-quantum components of a coherent field. These beats result from quantum interference between the amplitudes of atomic transition probabilities under the action of coherent n-photon field components. For the statistical incoherent mixture of photons P_{gm}, the transition probabilities are summed in Eq. (6). For the coherence field P_{gc}, the transition probability amplitudes are summed.

Thus, the presence (or absence) of inversion beats in experiments conducted in the scheme of resonator QED [6] for a coherent field would provide an answer to the fundamental question of whether the decoherence exists in reduction or the subsystems correlate with each other, or, in other words, whether the Neumann compuational rule for the reduced density matrix of an observable subsystem is generally valid or the condition for correlation between subsystems (3) and (4) must be used in reduction.

REFERENCES

1. D. N. Klyshko, Usp. Fiz. Nauk **168**, 975 (1998) [Phys. Usp. **41**, 885 (1998)].
2. S. Ya. Kilin, Usp. Fiz. Nauk **169**, 507 (1999) [Phys. Usp. **42**, 435 (1999)].
3. M. B. Menskiĭ, Usp. Fiz. Nauk **170**, 631 (2000) [Phys. Usp. **43**, 585 (2000)].
4. A. I. Lipkin, Usp. Fiz. Nauk **171**, 437 (2001) [Phys. Usp. **44**, 417 (2001)].
5. M. B. Menskiĭ, Usp. Fiz. Nauk **171**, 459 (2001) [Phys. Usp. **44**, 438 (2001)].
6. J. M. Raimond, M. Brune, and S. Haroche, Rev. Mod. Phys. **73**, 565 (2001).
7. W. H. Zurek, quant-ph/0105127.
8. E. Knill, R. Laflamme, H. Barnum, *et al.*, quant-ph/0207171.
9. U. Fano, Rev. Mod. Phys. **29**, 74 (1957).
10. K. Blum, *Density Matrix. Theory and Applications* (Plenum, New York, 1981; Mir, Moscow, 1983).

11. J. von Neumann, *Mathematical Foundations of Quantum Mechanics* (Princeton Univ. Press, Princeton, 1955; Nauka, Moscow, 1964).
12. I. Prigogine, *The End of Certainty* (Free Press, New York, 1997; Regul. Khaot. Din., Izhevsk, 1999).
13. V. S. Batista and P. Brumer, Phys. Rev. Lett. **89**, 143201 (2002).
14. N. K. Solovarov, in *The 2001 Yearbook of Kazan Physicotechnical Institute, Kazan Scientific Center, Russian Academy of Sciences*, Ed. by K. M. Salikhov (Fiztekhpress, Kazan, 2002), p. 104.
15. N. K. Solovarov, quant-ph/0304142.
16. N. Imoto, M. Ueda, and T. Ogawa, Phys. Rev. A **41**, 4127 (1990).
17. T. Fukuo, T. Ogawa, and K. Nakamura, Phys. Rev. A **58**, 3293 (1998).
18. W. H. Louisell, *Quantum Statistical Properties of Radiation* (Wiley, New York, 1973).
19. L. Allen and J. H. Eberly, *Optical Resonance and Two-Level Atoms* (Wiley, New York, 1975; Mir, Moscow, 1978).
20. H. I. Yoo and J. H. Eberly, Phys. Rep. **118**, 239 (1985).
21. G. Rempe, H. Walther, and N. Klein, Phys. Rev. Lett. **58**, 353 (1987).
22. F. W. Cummings, Phys. Rev. **140**, A1051 (1965).
23. N. B. Narozhny, J. J. Sanchez-Mondragon, and J. H. Eberly, Phys. Rev. A **23**, 236 (1981).
24. R. Loudon, *The Quantum Theory of Light* (Clarendon Press, Oxford, 1973; Mir, Moscow, 1987).
25. D. A. Demidov and N. K. Solovarov, Laser Phys. **5**, 997 (1995).

Translated by R. Tyapaev

JETP Letters, Vol. 78, No. 5, 2003, pp. 272–275. Translated from Pis'ma v Zhurnal Éksperimental'noĭ i Teoreticheskoĭ Fiziki, Vol. 78, No. 5, 2003, pp. 718–721.

Interaction of a Charge with a Plane Wave in a Medium

V. V. Ternovskiĭ* and A. M. Khapaev

Faculty of Physics, Moscow State University, Vorob'evy gory, Moscow, 119992 Russia

**e-mail: vladimir1961@hotmail.com*

Received June 3, 2003; in final form, July 24, 2003

The problem of simulating the energy state of a relativistic charge in the field of a circularly polarized plane wave and longitudinal magnetic field in a medium with the refractive index $k \neq 1$ is analyzed. The classical description of the interaction reduces to the integration of the Maxwell–Lorentz equation. The presence of a medium leads to qualitative changes in the charge dynamics. An exact analytic representation of the energy of an ensemble of relativistic charges as a function of the average flight coordinate $\bar{z}$ is obtained for $k = 1$. Moreover, the asymptotic approximation for $k \neq 1$ is constructed in the first approximation in $\mu = 1 - 1/k^2$ by the Van der Pol method. © *2003 MAIK "Nauka/Interperiodica".*

PACS numbers: 03.50.De

Relativistic motion of charged particles in electromagnetic fields has long attracted interest from both physical and mathematical viewpoints [1, 2]. The classical description of motion of a charge reduces to the integration of the equation

$$m_0\ddot{x}_\mu = \frac{e}{c}\dot{x}_\nu H_{\mu\nu}. \tag{1}$$

In this work, we give a Fourier-series representation for a solution of Eq. (1) for a circularly polarized plane wave in a magnetic field in a medium with the refractive index k that differs slightly from unity. Up to now, solutions have been found for $k = 1$ [3] and for particular resonant cases [4]. This work aims to find all possible solutions to Eq. (1) as functions of laboratory time t and flight coordinate z. The problem is considered in the approximation of a given field, and the wave magnetic field is taken into account.

Formulation of the problem. Equation (1) of motion of a charge is solved in the region $z > 0$ for arbitrary initial conditions

$$\dot{x}_0 = c\beta_{x0}\gamma_0, \quad \dot{y}_0 = c\beta_{y0}\gamma_0,$$
$$\dot{z}_0 = c\beta_{z0}\gamma_0, \quad \gamma_0 = 1/(1-\beta_0^2)^{1/2}, \tag{2}$$

where the dot over a symbol means the derivative with respect to the proper time τ and $\beta_0 = (\beta_{x0}, \beta_{y0}, \beta_{z0})$ is the initial velocity of the particle. The fields of the wave and axial magnetic field are specified as

$$\mathbf{A} = -\frac{cE_0}{\omega}[\sin(\omega\xi + \psi_0)\mathbf{i} - g\cos(\omega\xi + \psi_0)\mathbf{j}],$$

$$\mathbf{E} = -\frac{1}{c}\mathbf{A}'(\xi), \quad \mathbf{H} = \mathbf{H}_0\mathbf{k} - \frac{1}{\beta_f c}\mathbf{n}\times\mathbf{E}, \quad \xi = t - \frac{z}{\beta_f c},$$

where H_0 is the amplitude of the constant magnetic field (of arbitrary sign), $g = \pm 1$ is the wave polarization, ω is the frequency, E_0 and ψ_0 are the amplitude and initial phase of the wave, and $\beta_f = 1/k$ is the phase velocity. In what follows, we replace z, t, ε, c_x, c_y, $\dot{x}_0$, $\dot{y}_0$, $\dot{z}_0$, and τ by the respective dimensionless variables

$$\frac{\omega z}{c}, \omega t, \varepsilon = \frac{eE_0}{m\omega c}, \frac{c_x}{c}, \frac{c_y}{c}, \frac{\dot{x}_0}{c}, \frac{\dot{y}_0}{c}, \frac{\dot{z}_0}{c} \text{ and } \omega\tau.$$

Solutions as functions of z and t with respect to an observer at rest are of practical interest. We use the differential transition formula

$$\frac{d}{dz} = \frac{\beta_f}{\gamma(\tau) - \alpha}\frac{d}{d\tau},$$

where $\alpha = \gamma(1 - \beta_z\beta_f) = \text{const}$ is the energy–momentum integral.

Thus, the Cauchy problem for Eq. (1) reduces to the integration of the oscillator equation

$$(\gamma - \alpha)^2\frac{d^2\gamma}{dz^2} + (\gamma - \alpha)\left(\frac{d\gamma}{dz}\right)^2 + P_3(\gamma, \mu) = 0 \tag{3}$$

with initial conditions (2). Here,

$$P_3(\gamma, \mu) = \frac{1}{2}\frac{\mu^2}{1-\mu}\gamma^3 + \frac{3}{2}\mu\delta\gamma^2 + \frac{1}{2}(2\delta^2(1-\mu) + \mu s)\gamma$$
$$+ (1-\mu)\left(\frac{1}{2}\delta s - g\frac{\omega_0}{\omega}\varepsilon^2\right),$$

$$\mu = 1 - \beta_f^2, \quad \delta = g\frac{\omega_0}{\omega} - \frac{\alpha}{1-\mu},$$

$$s = 1 + \varepsilon^2 + c_x^2 + c_y^2 + \frac{\alpha^2}{1-\mu} - 2g\frac{\omega_0}{\omega}\gamma_0,$$

0021-3640/03/7805-0272$24.00

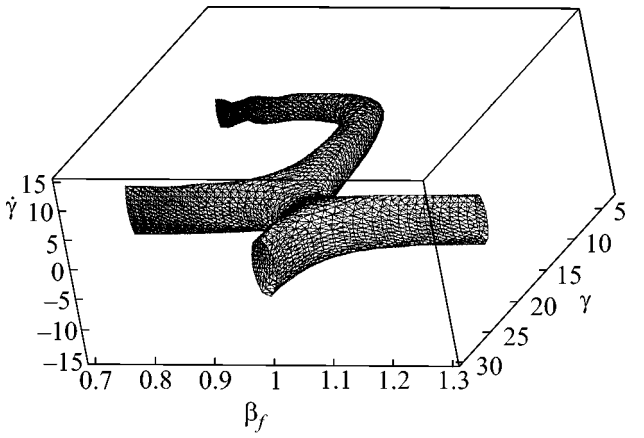

Fig. 1. Phase portrait of Eq. (5) with the parameters $\beta_{x0} = \beta_{y0} = 0.2$, $\beta_{z0} = 0.958$, $\varepsilon = 0.66$, $\omega_0/\omega = 0.84$, $\psi_0 = 1.5$, and $g = 1$.

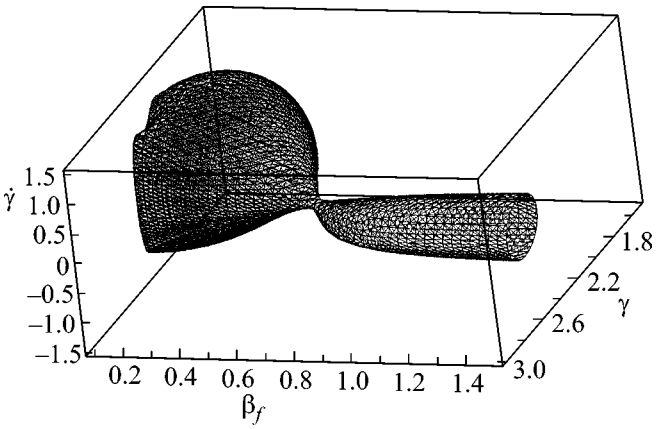

Fig. 2. Phase portrait of Eq. (5) with the parameters $\beta_{x0} = \beta_{y0} = 0.1$, $\beta_{z0} = 0.9$, $\varepsilon = 0.8$, $\omega_0/\omega = 1.9$, $\psi_0 = 0.5$, and $g = -1$.

$$c_x = \dot{x}_0 + \varepsilon\sin\psi_0 + \frac{\omega_0 y_0}{c}, \quad c_y = \dot{y}_0 - g\varepsilon\cos\psi_0 - \frac{\omega_0 x_0}{c}.$$

Energy $m_0c^2\gamma$ as a multivalued function of z. Energy or relativistic factor γ is a multivalued function of z; i.e., there are β_{x0}, β_{y0}, β_{z0}, ε, ω_0/ω, β_f, and ψ_0 values such that several γ values correspond to certain points on the z axis at different times. Therefore, the analytic and numerical solution for γ as a function of z can be obtained only in sections where this function is single-valued. In other words, a charge in the field of a circularly polarized wave and a constant magnetic field can be stopped in the z direction. Moreover, the charge can be trapped by the wave at $\beta_f = 1$ and move on the toroidal surface [5]. The manifold of the input parameters is determined from the condition $\dot{z} = 0$ and relation $\dot{x}^2 + \dot{y}^2 + \dot{z}^2 = c^2(\gamma^2 - 1)$:

$$2g\gamma_0\beta_{z0}\beta_f\frac{\omega_0}{\omega} = (c_x)^2 + (c_y)^2 - (\varepsilon + \sqrt{\alpha^2 - 1})^2. \quad (4)$$

The surface specified by manifold (4) in the space of input data separates the regions of single-valued and multivalued solutions.

Phase portrait of Eq. (1). To determine γ as a function of z, we reveal the effect of the medium or parameter μ on the phase portrait of Eq. (1). Volodin *et al.* [6] showed that Eq. (1) is equivalent to the equation

$$\dot{\gamma}^2 + P_4(\gamma, \mu) = 0, \quad (5)$$

where $P_4(\gamma, \mu)$ is a fourth-order polynomial of γ. Figure 1 shows the three-dimensional phase portrait of Eq. (5) for the given parameters β_{x0}, β_{y0}, β_{z0}, ε, ω_0/ω, ψ_0, and $g = 1$. As is seen, the amplitude of γ oscillations increases sharply at $\mu \approx 0$. This means that one can select a medium with properties such that the charged particle interacting with the electromagnetic wave acquires energy. In contrast, it is difficult to practically realize the cyclotron-resonance condition $\delta = 0$ [7], because any small perturbation of the input data gives rise to a periodic solution.

The phase portrait shown in Fig. 2 for the wave polarization $g = -1$ differs from the above case. There is a region of positive μ values, where the particle interacts weakly with the wave in spite of strong initial swirling.

To determine phase surface, it is sufficient to solve algebraic equation (5) with respect to $\dot{\gamma}$, γ, and μ. The phase portrait provides the amplitude and energy values upon changing in the properties of the medium without solving the differential equation.

Stable orbits and bifurcation values of the refractive index. Equation (5) describes oscillations of the conservative system and can be analyzed within the framework of bifurcation theory [8]. We aim to find the set of the input parameters for which energy is, possibly, maximal.

Stable orbits are determined from the cubic equation

$$F(\gamma, \mu) = \left(\frac{\mu\gamma}{1-\mu} + \delta\right)^3 + \left(\frac{\mu}{1-\mu}s - \delta^2\right)\left(\frac{\mu\gamma}{1-\mu} + \delta\right) - 2g\frac{\mu}{1-\mu}\frac{\omega_0}{\omega}\varepsilon^2 = 0.$$

It is convenient to find the roots in the trigonometric form. The number of real roots is determined by the signs of the discriminant

$$D = \frac{1}{27}\left(\frac{\mu}{1-\mu}s - \delta\right)^3 + \frac{\mu^2}{(1-\mu)^2}\frac{\omega_0^2}{\omega^2}\varepsilon^4$$

and quantity $\mu s - \delta^2$. Three real roots exist at $D \le 0$ and $\mu s - \delta^2 < 0$, and one real root exists at $D > 0$ and

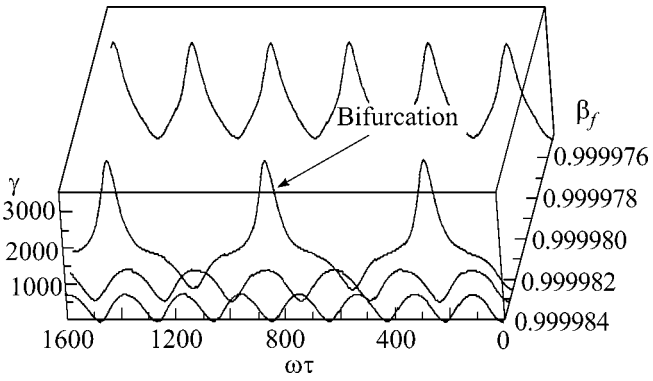

Fig. 3. Particle energy as a function of time ωτ and parameter β_f.

$\mu s - \delta^2 < 0$. For $\mu s - \delta^2 > 0$, the single regular stable real root is found from the relation

$$\frac{\mu}{1-\mu}\gamma^* + \delta = -2R\sinh\frac{\vartheta}{3},$$
$$\sinh\vartheta = 3^{3/2}\left|\frac{\mu}{1-\mu}\right|\frac{\omega_0}{\omega}\varepsilon^2\left|\frac{\mu}{1-\mu}s - \delta^2\right|^{2/3}, \quad (6)$$
$$R = \operatorname{sgn}\left(-2\frac{\mu}{1-\mu}g\right)\sqrt{\frac{1}{3}}\sqrt{\left|\frac{\mu}{1-\mu}s - \delta^2\right|}.$$

Some roots are obviously singular in the limit $\mu \longrightarrow 0$.

According to [8], the bifurcation points are determined from the general solution to the set of equations

$$\begin{cases} F(\gamma,\mu) = 0 \\ F'_\gamma(\gamma,\mu) = 0 \end{cases} \longleftrightarrow \left(\delta^2 - \frac{\mu}{1-\mu}s\right)^{3/2} = \sqrt{\frac{3}{2}}6\frac{\mu}{1-\mu}g\frac{\omega_0}{\omega}\varepsilon^2. \quad (7)$$

Since δ and s depend on μ, the bifurcation refractive index $k = 1/\beta_f$ is sought numerically. In particular, Eq. (7) for $\beta_{x0} = \beta_{y0} = 0.2$, $\beta_{z0} = 0.958$, $\varepsilon = 0.66$, $\omega_0/\omega = 0.84$, and $\psi_0 = 1.5$ has two bifurcation points $k_{1,2} = 1.000017598$ and 1.054951067. The amplitude of energy oscillations at the point k_1 is higher than the initial value $\gamma_0 = 21.14774672$ by a factor of 150. Figure 3 shows energy γ as a function of proper time τ and β_f.

Method of solution. Equation (3) describes oscillations of the conservative system. The exact analytic solution is unknown. An approximate solution is constructed by the Van der Pol method of averaging [9] under the assumption that the parameter μ is small. We also assume that there is $\varepsilon > 0$ such that bifurcation points are absent in the interval $-\varepsilon < \mu < \varepsilon$. More exactly, we expand γ into an asymptotic series near regular root (6). To a first approximation, the periodic solution to Eq. (3) has the form

$$\gamma(z) = \gamma^* + \frac{1}{2}\frac{\left(1+\frac{1}{2}\mu\right)}{a}b^2 + 2b\sum_{n=1}^{\infty}\frac{1}{n}J'_n\left(-\frac{n\left(1+\frac{1}{2}\mu\right)}{a}b\right) \times \cos\left\{n\left[\frac{\Omega}{a}z - \frac{\left(1+\frac{1}{2}\mu\right)}{a}\frac{\dot\gamma_0}{\Omega} - \theta_0\right]\right\}, \quad (8)$$

where

$$a = \left(1+\frac{1}{2}\mu\right)\gamma^* - \alpha_0 - \frac{1}{2}\mu\gamma_0,$$
$$b = \sqrt{(\gamma_0-\gamma^*)^2 + \frac{\dot\gamma_0^2}{\Omega^2}},$$
$$\Omega = \delta_0 + \frac{\mu}{2\delta_0}d, \quad \tan\theta_0 = \frac{\gamma_0}{\gamma_0-\gamma^*\Omega},$$
$$d = \delta_0^2\gamma_0(\beta_{z0}-2) - \delta_0 s_0 + 3g\frac{\omega}{\omega_0}\varepsilon^2,$$
$$\gamma^* = -\frac{1}{2}\frac{s_0}{\delta_0} + \frac{1}{\delta_0}g\frac{\omega_0}{\omega}\varepsilon^2 + \frac{\mu}{3\delta_0^2} \times\left\{\left[\frac{1}{2}\delta_0^2\gamma_0^2(1-\beta_{z0}+\beta_{z0}^2) + \frac{1}{4}s_0\delta_0\gamma_0(2-\beta_{z0}) + \frac{s_0^2}{8}\right] - \frac{1}{2}d^2\right\},$$

α_0, s_0, and δ_0 are the coefficients α, s, and δ at $\mu = 0$, and J_n are the integer-order Bessel functions. To the factor μ, the oscillation period in z is given by the formula

$$T_z = \frac{2\pi(\gamma^*-\alpha_0)}{\delta_0} + \mu\frac{\pi}{\delta_0}\left(\gamma^* - \gamma_0 - 2(\gamma^*-\alpha_0)\frac{d}{2\delta_0^3}\right].$$

Fourier-series solution (8) was constructed by using the known relation

$$\cos\eta = -\frac{1}{2}\delta + 2\sum_{n=1}^{\infty}\frac{1}{n}J'_n(n\sigma)\cos n\nu,$$

where $\nu = \eta - \sigma\sin\eta$. Representation (8) is invalid at the points of splash (bifurcation) and multivalence of γ. The choice of μ is determined by the cylinder-like phase surfaces of Eq. (5) (see Fig. 2).

The solution as a function of the laboratory time t is constructed similarly:

$$\gamma(t) = \gamma^* + \frac{1}{2\gamma^*}b^2 + 2b\sum_{n=1}^{\infty}\frac{1}{n}J_n'\left(-\frac{n}{\gamma^*}b\right) \times \cos\left\{n\left[\frac{\Omega}{\gamma^*}t - \frac{\dot\gamma_0}{\gamma^*\Omega} - \theta_0\right]\right\}.$$

Ensemble of charges at $\mu = 0$. Solution (8) describes the energy of one charge as a function of z. To describe the energy of an ensemble of noninteracting relativistic charges, we use the "electron-ring" model:

$$x_0 = R_0\cos\varphi, \quad y_0 = R_0\sin\varphi,$$

$$\beta_{x0} = \beta_{\perp 0}\sin\varphi, \quad \beta_{y0} = -\beta_{\perp 0}\cos\varphi, \quad 0 \le \varphi \le 2\pi.$$

The problem reduces to the search for the quantity

$$\bar\gamma(\tau) = \frac{1}{2\pi}\int_0^{2\pi}\gamma(\tau,\varphi)d\varphi, \quad \bar z(\tau) = \frac{1}{2\pi}\int_0^{2\pi}z(\tau,\varphi)d\varphi$$

as a function of $\bar z$. The necessary solutions are determined from Eq. (3) at $\mu = 0$:

$$\bar\gamma(\bar z) = \bar q - \frac{1}{2}\frac{(\gamma_0 - \bar q)^2}{(\alpha_0 - \bar q)} + 2(\gamma_0 - \bar q)\sum_{n=1}^{\infty}\frac{1}{n}J_n'\left(n\frac{(\gamma_0 - \bar q)}{(\alpha_0 - \bar q)}\right)\cos\left(n\frac{\delta_0}{(\alpha_0 - \bar q)}\bar z\right), \quad (9)$$

$$\bar q = g\varepsilon^2\frac{\omega_0}{\omega}\frac{1}{\delta_0^2} - \frac{1}{2\delta_0} \times\left(1 + \alpha_0^2 + 2\varepsilon^2 + \left(\beta_{\perp 0}\gamma_0 + \frac{\omega_0 R_0}{c}\right)^2 - 2g\gamma_0\frac{\omega_0}{\omega}\right).$$

The period of ensemble oscillations is equal to $\bar T_{\bar z} = 2(\bar q - \alpha_0)\pi/\delta_0$. The solution at $\mu \neq 0$ is derived similarly to Eq. (9) but is not present in this short report.

The above analysis reveals a complex behavior of a relativistic charge in the system consisting of the wave and a magnetic field. The charge can acquire considerable energy in a medium whose properties are close to vacuum. The spike (bifurcation) in energy upon changing the refractive index of the medium is associated with the presence of the parameter μ in higher powers of the polynomial $P_3(\gamma, \mu)$. Indeed, the effect disappears at $\mu = 0$.

Only several terms of the solution in the form of Fourier series (8) and (9) can be taken into account due to the exponential decrease in coefficients. In the second approximation constructed by the averaging method mentioned above, higher harmonics with unwieldy coefficients appear. We emphasize that formula (8) is exact at $\mu = 0$.

Since energy γ is a multivalued function of z, the applicability of numerical methods to Eq. (1) is restricted. The method developed above can be generalized to nonuniform periodic magnetic fields.

We are grateful to B.S. Luk'yanchik for discussions and valuable remarks.

REFERENCES

1. L. D. Landau and E. M. Lifshitz, *The Classical Theory of Fields*, 6th ed. (Nauka, Moscow, 1973; Pergamon Press, Oxford, 1975).
2. A. A. Sokolov and I. M. Ternov, *Radiation from Relativistic Electrons*, 2nd ed. (Nauka, Moscow, 1983; AIP, New York, 1986).
3. B. A. Volodin, I. V. Ponomarev, and A. M. Khapaev, Izv. Vyssh. Uchebn. Zaved., Fiz. **3**, 113 (1984).
4. A. Bourdier and S. Gond, Phys. Rev. E **62**, 4189 (2000).
5. V. V. Ternovskiĭ and A. M. Khapaev, Fundam. Prikl. Mat. **8**, 547 (2002).
6. B. A. Volodin, V. R. Khalilov, and A. M. Khapaev, Izv. Vyssh. Uchebn. Zaved., Fiz. **2**, 97 (1981).
7. V. P. Milant'ev and Ya. N. Shaar, Zh. Tekh. Fiz. **70**, 100 (2000) [Tech. Phys. **45**, 1054 (2000)].
8. A. A. Adronov, A. A. Vitt, and S. É. Khaĭkin, *Theory of Oscillators* (Fizmatgiz, Moscow, 1959; Pergamon Press, Oxford, 1966).
9. N. N. Bogolyubov and Yu. A. Mitropol'skiĭ, *Asymptotic Methods in the Theory of Nonlinear Oscillations*, 3rd ed. (Fizmatgiz, Moscow, 1963; Gordon and Breach, New York, 1962).

Translated by R. Tyapaev

JETP Letters, Vol. 78, No. 5, 2003, pp. 276–280. Translated from Pis'ma v Zhurnal Éksperimental'noĭ i Teoreticheskoĭ Fiziki, Vol. 78, No. 5, 2003, pp. 722–726.

Soliton Structures of a Wave Field with an Arbitrary Number of Oscillations in Nonresonance Media

D. V. Kartashov*, A. V. Kim, and S. A. Skobelev

Institute of Applied Physics, Russian Academy of Sciences, Nizhni Novgorod, 603950 Russia

**e-mail: dekart@ufp.appl.sci-nnov.ru*

Received June 19, 2003; in final form, August 5, 2003

A new class of solitary solutions for a wave field is found. This class describes soliton-like structures of a circularly polarized radiation that propagate in a nonresonance medium and which involve an arbitrary number of field oscillations. A feature peculiar to these solutions is that they undergo a smooth transformation from solitons of the Schrödinger type, which correspond to long pulses involving many oscillations, to extremely short visible pulses, which, in fact, do not extend beyond one period. Realizability of such soliton structures is considered for a field of linear polarization, and their structural stability is shown numerically. *© 2003 MAIK "Nauka/Interperiodica".*

PACS numbers: 42.65.Tg

1. Soliton solutions to nonlinear wave equations are of general interest since they belong to basic elementary structures playing a fundamental role in nonlinear physics [1]. At present, advances made in the realm of laser technologies make it possible to perform experimental investigations into the processes of nonlinear interaction between matter and electromagnetic pulses of duration equal to a few periods of optical oscillations [2–4]. The possibility of soliton modes of propagation of such extremely short field pulses in various nonlinear media [5, 6] is one of the most important and interesting questions in this connection. A theoretical analysis of physical phenomena arising in such interactions is complicated by the fact that the well-developed nonlinear-optics formalism employing the approximation of a slowly varying wave-field amplitude is inapplicable under the conditions of extremely short pulse durations. In order to describe the evolution of a field in this case correctly, it is necessary to use wave equations describing the dynamics of the field in a pulse as a discrete unit without recourse to a scale separation into a slowly varying envelope and a high-frequency filling. In the present study, the propagation of electromagnetic pulses in a nonresonance medium is considered in the reflectionless approximation, this consideration being performed for an arbitrary number of field oscillations in a pulse. It is shown that there exists a new class of exact solitary solutions describing a nonlinear propagation of wave pulses whose envelope has a soliton structure, which, however, includes a finite number of field oscillations. An appealing feature of these solutions is that there is an uninterrupted connection between them and Schrödinger-type soliton solutions, which makes it possible to trace a transition from Schrödinger solitons to visible pulses involving less than one period of optical oscillations.

2. As a starting point, we will employ a vector wave equation in the reflectionless approximation, which is extensively used in describing the nonlinear dynamics of extremely short pulses containing a small number of optical oscillations. In this approximation, where it is assumed that variations in field distributions are small over scales commensurate with characteristic wavelengths, the reduced wave equation for a nonresonance medium can be represented in the form (see [6])

$$\frac{\partial^2 \mathbf{E}}{\partial z \partial \tau} + n\mathbf{E} + g\frac{\partial}{\partial \tau}\left(\mathbf{E}^2\frac{\partial \mathbf{E}}{\partial \tau}\right) + h\frac{\partial}{\partial \tau}\left[\mathbf{E}, \left[\mathbf{E}, \frac{\partial \mathbf{E}}{\partial \tau}\right]\right] = 0, \quad (1)$$

where z is the coordinate along the direction of pulse propagation and $\tau = t - z\varepsilon_o^{1/2}/c$ is the time in the coordinate frame comoving with the pulse, ε_o and c being, respectively, the static dielectric permittivity of the medium and the speed of light in a vacuum. Equation (1), which is the simplest one in its class, includes both a nonlinear low-frequency dispersion (n) and an inertia-free nonlinearity of the Kerr type (g, h; see, for example, [7]). In particular, it describes the propagation of extremely short pulses in optical fibers in the region of anomalous dispersion [8], as well as their self-interaction in an ionized gas, where a plasma dispersion is more pronounced than a gas dispersion, which is associated with neutral particles [9]. It is worth noting that the wave equation in the form (1) disregards the high-frequency dispersion of the medium; this corresponds to the assumption that the spectrum of the optical pulse being considered lies rather far off the zero-dispersion point, entirely falling within the region of anomalous dispersion. It should also be noted that, for resonance media, fundamental equations based on the model of a two-level medium and an analysis of corresponding wave fields are given in [10–12] (see also [5] and references therein).

It can easily be shown that by introducing a high-frequency filling the original equation (1) is reduced to a nonlinear Schrödinger equation for a slowly varying field amplitude.

In the following, we consider the propagation of laser radiation in a medium characterized by an electric-type nonlinearity, where $h = 2g/3$. Using the scale invariance of Eq. (1), we then write it in terms of the projections ($\mathbf{E} = \mathbf{e}_x E_x + \mathbf{e}_y E_y$) onto relevant axes in dimensionless variables; that is,

$$\frac{\partial^2 E_{x,y}}{\partial z \partial \tau} + E_{x,y} + \frac{\partial^2}{\partial \tau^2}[(E_x^2 + E_y^2)E_{x,y}] = 0. \quad (2)$$

Here, $\mathbf{e}_x$ and $\mathbf{e}_y$ are unit vectors along the x and y axes of a system of Cartesian coordinates, while E_x and E_y are the corresponding projections of the electric-field vector. From (2), it follows that, for localized field distributions, the following integral relation holds:

$$\int_{-\infty}^{+\infty} E_{x,y} d\tau = 0. \quad (3)$$

It expresses the absence of an average field and indicates that solutions have an oscillating character. Considering that the group and phase velocities of waves may be different, we represent solutions to Eq. (2) in the form

$$E_x(z, \tau) = a(z, \tau)\cos\varphi(z, \tau),$$
$$E_y(z, \tau) = a(z, \tau)\sin\varphi(z, \tau),$$

which describes the evolution of a circularly polarized field. For the amplitude $a(z, \tau)$ of the wave field being considered and its phase $\varphi(z, \tau)$, we then obtain the set of exact equations

$$a_{z\tau} - \varphi_z\varphi_\tau a + a + (a^3)_{\tau\tau} - \varphi_\tau^2 a^3 = 0, \quad (4)$$

$$a\varphi_{z\tau} + a_z\varphi_\tau + a_\tau\varphi_z + 2(a^3)_\tau\varphi_\tau + a^3\varphi_{\tau\tau} = 0, \quad (5)$$

where a subscript on a quantity denotes its partial derivative with respect to the corresponding argument. Assuming that the envelope of the field propagates at a constant velocity, we seek solutions in the form

$$a(z, \tau) = a(\xi), \quad (6)$$

$$\varphi(z, \tau) = \omega\tau - kz + \int_{-\infty}^{\xi} g(a) d\xi, \quad (7)$$

where $\xi = \tau - \gamma z$. The local frequencies and wave vectors are defined as $\varphi_\tau = \omega + g(a)$ and $\varphi_z = -k - \gamma g(a)$, respectively. Substituting the above relations into Eq. (5) and defining ω as the carrying frequency of the signal in the limit of small amplitudes—that is, $g(a) \longrightarrow 0$ for $a \longrightarrow 0$—we find that $g(a) = \omega a^2(3\gamma - 2a^2)/2(\gamma - a^2)^2$, $k = -\gamma\omega$, and for the phase of the field we eventually obtain

$$\varphi(z, \tau) = \omega\tau + \gamma\omega z + \int_{-\infty}^{\xi} \frac{\omega a^2(3\gamma - 2a^2)}{2(\gamma - a^2)^2} d\xi. \quad (8)$$

Thus, we see that not only may a field pulse contain a finite number of oscillations, but it must also be phase-modulated—that is, contain a frequency chirp of a rather complicated shape, in general, $\varphi_\tau \sim g(a)$. Equation (4) for the amplitude then takes the form

$$u_{\eta\eta} - \frac{6uu_\eta^2}{1 - 3u^2} - \frac{u}{1 - 3u^2}\left\{\delta^2 - \frac{u^2[4(1 - u^2)^2 - u^2]}{4(1 - u^2)^3}\right\} = 0. \quad (9)$$

Here, we have introduced the variables $\eta = \omega\xi$ and $u = a/\gamma^{1/2}$; as one can easily see, the family of soliton-like solutions is one-parameter in this case—that is, it depends on the parameter $\delta^2 = 1/\gamma\omega^2 - 1 > 0$. The first integral of Eq. (9) has the form

$$\left(\frac{du}{d\eta}\right)^2 = \frac{u^2}{(1 - 3u^2)^2} \times \left[\delta^2 - \frac{3}{2}(\delta^2 + 1)u^2 + \frac{(4 - 5u^2)u^2}{4(1 - u^2)^2}\right] + \frac{C}{(1 - 3u^2)^2}, \quad (10)$$

where C is a constant of integration; it is equal to zero for localized field distributions. In accordance with this, solutions to this equation can generally be represented only in quadratures. However, the possible types of solutions can easily be analyzed in the phase plane, where the phase trajectories of (10) are symmetric with respect to the $u = 0$ axis. Restricting our consideration to the half-plane $u \geq 0$ we can see that Eq. (9) has four equilibrium states—three centers and a saddle point at the origin of coordinates—which are separated by the singular straight lines $u = 1/\sqrt{3}$ and $u = 1$. The structure of the phase plane depends greatly on the parameter δ. A closed saddle separatrix ($C = 0$) existing only for $\delta^2 \leq \delta_c^2 = 1/8$ and including one or two equilibrium states of the center type corresponds to soliton solutions in which we are interested. For $\delta^2 < 1/8$, it includes the closest equilibrium state, and a typical phase plane corresponding to this case is displayed in Fig. 1a. For these parameters, the maximum amplitude of a soliton is bounded from above, $u_{\max}^2 < 1/3$, and its dependence on the root-mean-square duration defined as

$$\tau_s = \left[\int_{-\infty}^{\infty} \eta^2 u^2 d\eta / \int_{-\infty}^{\infty} u^2 d\eta\right]^{1/2}$$

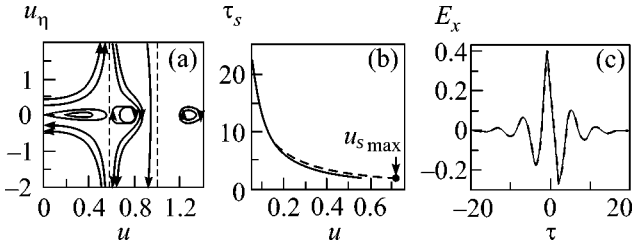

Fig. 1.

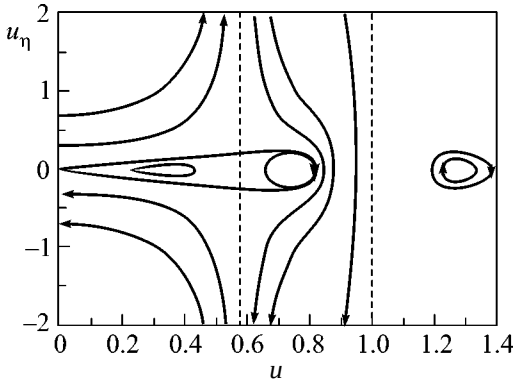

Fig. 2.

is presented in Fig. 1b. For $u_{\max}^2 \ll 1$, one can integrate Eq. (10) and represent its approximate solution in the implicit form

$$6\delta\sqrt{\delta^2 - \frac{u^2}{2}} - \operatorname{arccosh}\left(\frac{\sqrt{2}\delta}{u}\right) = \pm\delta\eta. \qquad (11)$$

This approximate solution describes field dynamics to a rather high degree of precision everywhere up to $\delta \approx \delta_c$, with the exception of the limiting value itself. Figure 1c shows characteristic oscillograms of the fields that correspond to the exact and approximate soliton solutions at $\delta = 0.32$ that include about one period of optical oscillations. As can be seen, these solutions are rather close, their maximum deviation being less than 3%.

At $\delta^2 = 1/8$, the separatrix trajectory changes qualitatively and, in view of the removal of the singularity at $u^2 = 1/3$, includes two equilibrium states (see Fig. 2). This separatrix solution can be referred to as a limiting soliton corresponding to the minimum possible duration, including, as a matter of fact, less than one period of oscillations ($\tau_{s\,\min} = 1.84$), and, accordingly, to the maximum possible amplitude $u_{s\,\max}^2 = 2/3$. The corresponding exact solution has the same functional form as (11), but it describes a soliton of maximum possible energy:

$$\frac{\sqrt{2-3u^2}}{3} - (2)^{-1/2}\operatorname{arccosh}\left(\frac{2}{3u^2}\right)^{1/2} = \pm\eta/4. \qquad (12)$$

For $\delta^2 > 1/8$, the closed separatrix trajectory becomes disconnected, which suggests the absence of localized solutions.

Let us now establish connections between the solutions obtained above and the well-known solitons of the envelope that exist in the case of the nonlinear Schrödinger equation (NSE) and its generalizations [1, 13]. The duration of the localized field distributions found here (see Fig. 1b) is approximately in inverse proportion to their amplitudes; therefore, a transition to long quasimonochromatic pulses containing many oscillations occurs at small amplitudes, $u^2 \ll 1/3$; as follows from Eq. (10), this takes place for $\delta^2 \ll 1/9$. In this case, Eq. (10) reduces to an equation for finding NSE solitons, $u_\eta^2 = u^2(\delta^2 - u^2/2)$, which has the fundamental Schrödinger soliton $u(\eta) = \sqrt{2}\,\delta/\cosh(\delta\eta)$ among its solutions. As the amplitude is increased, the duration of the soliton decreases, with the result that processes associated with the dispersion of group velocities of various frequency components begin to play an ever more important role, and this affects, first of all, the phase-modulated structure of the pulse in Eq. (8). Its amplitude dependence then transforms into solitons of a generalized nonlinear Schrödinger equation [14], which, as can easily be found from (10) by expanding relevant polynomials and retaining next-order terms, have the form

$$u(\eta) = \frac{2\delta}{\sqrt{1 + \cosh(2\delta\eta)}}. \qquad (13)$$

As the amplitude is increased further, the soliton duration becomes commensurate with the period of optical oscillations; as a matter of fact, this imposes, in accordance with the integral in (3), an upper bound on admissible values of the field, which is reflected in the existence of a limiting soliton solution. Thus, we can conclude that there is an uninterrupted connection between the soliton structures of the wave field that were found in the present study and soliton solutions of the Schrödinger type; owing to this, we can trace a transition from solitons of the envelope of quasimonochromatic radiation to optical visible solitons.

3. It is of interest to consider the question of whether the soliton structures of a wave field that were found above are implementable in the important particular case of linearly polarized radiation. For a linearly polarized field $\mathbf{E} = \mathbf{e}_x E$, Eq. (2) assumes the form

$$\frac{\partial^2 E}{\partial z \partial \tau} + E + \frac{\partial^2 E^3}{\partial \tau^2} = 0. \qquad (14)$$

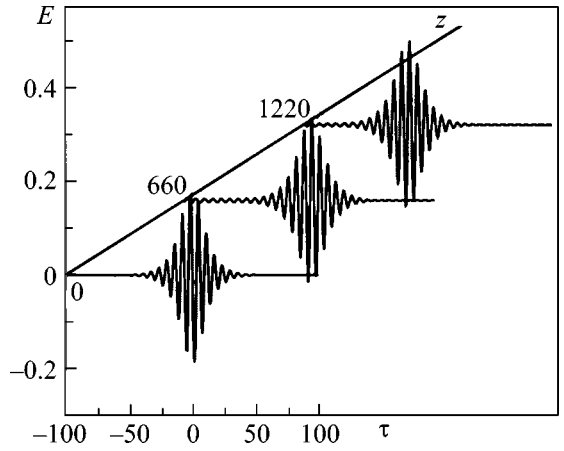

Fig. 3.

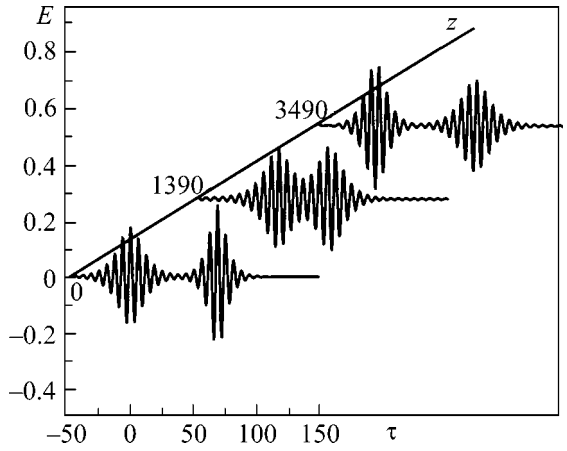

Fig. 4.

As is well known, the main distinction between the nonlinear dynamics of a linearly polarized field and that of a circularly polarized field is that the spectral composition can be enriched faster for the former, this concerning, above all, odd harmonics owing to a cubic character of nonlinearity. In the dispersive medium considered here and described by Eq. (14), however, the conditions of wave synchronisms for a resonance excitation (including a nonlinear excitation) of spectral harmonics of field components are not satisfied, as can easily be proven. This statement is supported, in particular, by the results of the numerical calculations performed in [8, 9], where it was found that the corresponding spectral components are small in the region of anomalous dispersion. Representing solutions to Eq. (14) in the form $E(z, \tau) = (2/\sqrt{3})a(z, \tau)\cos\varphi(z, \tau)$ and assuming that the field components at the frequencies of the third harmonic (3φ) are small, we obtain, for $a(z, \tau)$ and $\varphi(z, \tau)$, a set of equations that is identical to the set of Eqs. (4) and (5) and, for a determination of soliton distributions of the field, the same equation (9). It follows that the above analysis of soliton solutions for a circularly polarized field can be extended to the case of linearly polarized fields, whose nonlinear dynamics are expected to experience a strong influence of the wave solitons found above. A numerical simulation that we performed for Eq. (14) revealed that its wave-field solitons are structurally stable formations—particularly with respect to collisions—and propagate without variation in its envelope over distances considerably exceeding characteristic path scales: the dispersion length $L_{\text{dis}} \sim \omega_*^2/\Delta\omega$ (where ω_* and $\Delta\omega$ are, for example, the characteristic central frequency and the spectral width of the wave pulse, respectively) and the nonlinear-interaction range $L_{nl} \sim \Delta\omega/\omega_*^2 E_m^2$ (where E_m is the pulse amplitude). This fact is reflected in Fig. 3, where the length of the propagation of a pulse that was specified at the input as a wave soliton was $400L_{nl}$ (for this input field distribution, the characteristic lengths L_{dis} and L_{nl} were approximately equal at about 3 to 4). As can be seen from the figure, the soliton field pulse in question is a stable formation and can propagate without variations in its parameters over distances that considerably exceed characteristic path scales. The internal dynamics that are seen in this case are associated exclusively with variations in the phase of the field (see Eq. (8)). We also note that, if the spectrum of the input pulse falls within the region of anomalous dispersion, such localized distributions of the field undergo only slight structural changes when taking into account high-frequency dispersion that is described by a term of the form $\partial^4 E/\partial\tau^4$ in Eq. (14), and this is in accord with the numerical results of Kozlov and Sazonov [8].

Figure 4 illustrates the dynamics of a collision between two wave solitons having different amplitudes and identical carrying frequencies ($\omega = 1$) in the sense of Eq. (8). As is well known, the possibility that the structure of solitons remains unchanged upon collisions is one of the important properties which causes solitons to play a fundamental role in the nonlinear dynamics of wave processes. From Fig. 4, one can see that the soliton of greater amplitude catches up with the soliton of smaller amplitude, whereupon they pass through each other, recovering their former distributions upon the interaction; that is, they travel without a noticeable energy transfer and without losses by radiation. This result gives sufficient grounds to refer to the wave structures found here as wave solitons.

In conclusion, we would like to note that the stability of the wave solitons considered above with respect to collisions and an uninterrupted connection between them and Schrödinger solitons make it possible to treat them as basic wave-field structures whose role in the nonlinear dynamics of wave fields is not less fundamental than the role of Schrödinger solitons. In particular, numerical calculations show that they appear as stable elementary components in the dynamic process

through which the time compression of an originally broad pulse to rather low durations occurs, forming, at some stage, an extremely short pulse of a few field oscillations that is characterized by an amplitude exceeding the amplitude of a limiting soliton.

We are grateful to V.A. Mironov and A.M. Sergeev for interest in this study and discussion of its results.

REFERENCES

1. V. E. Zakharov, S. V. Manakov, S. P. Novikov, and L. P. Pitaevskiĭ, *Theory of Solitons: the Inverse Scattering Method* (Nauka, Moscow, 1980; Consultants Bureau, New York, 1984).
2. A. Baltuska, Z. Y. Wei, M. S. Pshenichnikov, and D. A. Wiersma, Opt. Lett. **22**, 102 (1997).
3. M. Nisoli, S. De Silvestri, O. Svelto, *et al.*, Opt. Lett. **22**, 522 (1997).
4. T. Brabec and F. Krausz, Rev. Mod. Phys. **72**, 545 (2000).
5. A. I. Maĭmistov, Kvantovaya Élektron. (Moscow) **30**, 287 (2000).
6. S. A. Kozlov, in *Problems of Coherent and Nonlinear Optics*, Ed. by I. P. Gurov and S. A. Kozlov (S-Peterb. Gos. Inst. Tochn. Mekh. Opt., St. Petersburg, 2000), p. 12.
7. S. N. Vlasov and V. I. Talanov, *Self-Focusing of Waves* (Inst. Prikl. Fiz. Ross. Akad. Nauk, Nizhni Novgorod, 1997).
8. S. A. Kozlov and S. V. Sazonov, Zh. Éksp. Teor. Fiz. **111**, 404 (1997) [JETP **84**, 221 (1997)].
9. A. Nazarkin and G. Korn, Phys. Rev. Lett. **83**, 4748 (1999).
10. J. C. Eilbeck, J. D. Gibbon, P. J. Coudrey, and R. K. Bullough, J. Phys. A **6**, 1337 (1973).
11. É. M. Belenov, P. G. Kryukov, A. V. Nazarkin, *et al.*, Pis'ma Zh. Éksp. Teor. Fiz. **47**, 442 (1988) [JETP Lett. **47**, 523 (1988)].
12. A. A. Zabolotskiĭ, Pis'ma Zh. Éksp. Teor. Fiz. **77**, 558 (2003) [JETP Lett. **77**, 464 (2003)].
13. A. Hasegawa, *Optical Solitons in Fibers* (Springer, Berlin, 1989).
14. E. M. Gromov and V. I. Talanov, Zh. Éksp. Teor. Fiz. **110**, 137 (1996) [JETP **83**, 73 (1996)].

Translated by A. Isaakyan

JETP Letters, Vol. 78, No. 5, 2003, pp. 281–284. From Pis'ma v Zhurnal Éksperimental'noĭ i Teoreticheskoĭ Fiziki, Vol. 78, No. 5, 2003, pp. 727–730.

Resonant Field Amplification near the RWM Stability Boundary in a Tokamak¶

V. D. Pustovitov

Institute of Nuclear Fusion, Russian Research Centre Kurchatov Institute, pl. Kurchatova 1, Moscow, 123182 Russia
e-mail: pustovit@nfi.kiae.ru

Received June 3, 2003; in final form, July 7, 2003

Evolution of a resistive wall mode (RWM)—a magnetic field perturbation produced by a plasma and partially stabilized by a conducting wall—is considered. It is assumed that there is a small resonant harmonic in the spectrum of the static error field. It is shown that the effect of this harmonic on the dynamics of stable RWMs increases as the plasma approaches the RWM stability boundary. The error field is "amplified" during the transition through this boundary. The smaller the rotation velocity of the perturbation and the longer the time during which the plasma stays near the stability boundary, the stronger this amplification is. © *2003 MAIK "Nauka/Interperiodica".*

PACS numbers: 52.55.Fa; 52.35.Bj

The theory of magnetohydrodynamic (MHD) plasma stability operates with a notion of small (to be precise, infinitesimal) perturbation that is "switched on" instantly in a "perfect" equilibrium configuration prepared beforehand. However, in real configurations, finite-amplitude perturbations are always present. In magnetic confinement systems, these are the so-called error fields—weak magnetic fields related, in particular, to inaccuracy in manufacturing and assembling the magnetic coils. Formally, these are the fields that are not included in the idealized theoretical description of a system. For example, a tokamak is considered to be an axially symmetric system, although weak magnetic fields breaking this symmetry are always present. It is these fields that will be discussed below.

It is known that sometimes such fields with an amplitude on the order of 10^{-4}–10^{-5} of the main toroidal field can significantly influence the plasma behavior in a tokamak [1]. This happens when certain factors produce an unfavorable combination. What is exactly needed for that still remains unclear because a convincing predictive theory has not yet been developed and the experimental data are incomplete and inconsistent [1]. This can be partially explained by the fact that studying the error field effects requires highly precise diagnostics and the elimination of masking factors.

In recent years, interest in the error field problem has greatly increased in connection with DIII-D experiments aimed at studying operating regimes near the MHD stability threshold, specifically, near the plasma pressure limit, which is one of the most important characteristics of tokamaks.

Theory and experiment show that high β values (where $\beta \equiv 2\bar{p}/\mathbf{B}^2$ is the ratio of the averaged plasma pressure $\bar{p}$ to the magnetic field pressure $\mathbf{B}^2/2$) could be achieved in a stationary tokamak if large-scale kink modes were stabilized [1, 2]. Such stabilization could be ensured by a highly conducting (in the best case, ideal) wall closely facing the plasma [3]. A real wall with a finite conductivity can completely stabilize a mode for a period on the order of the "wall time" τ_w, during which the magnetic field penetrates through the wall. This is certainly insufficient for discharges of interest (with a duration of hundreds of τ_w or longer). The conducting wall cannot prevent the development of kink modes over a large time interval but decreases their growth rates to values on the order of τ_w^{-1}. That is why these modes are called resistive wall modes (RWMs).

Recent years' experiments in the DIII-D tokamak were devoted to studying the physics of RWMs and methods for stabilizing these modes [2, 4–10]. RWMs observed in DIII-D arise at $\beta > \beta^{\text{no wall}}$, where $\beta^{\text{no wall}}$ is the ideal MHD stability limit calculated in the absence of a conducting wall. Great success of the DIII-D experiments was demonstrated by sustained operation at β twice as high as the RWM instability limit [8–10]. This outstanding result was achieved when the measures already used against RWMs were supplemented by the suppression of the above-mentioned weak (just several gauss) error fields, or, more precisely, by their main lowest harmonics that can "resonate" with the closed field lines of the idealized unperturbed configuration. Until the role of the error fields as a strong destabilizing factor was realized, experiments on the RWM feedback stabilization in the DIII-D tokamak yielded

¶ This article was submitted by the author in English.

much more modest results [2, 4–7], though theoretical forecasts (without account of error fields) were rather optimistic. These forecasts actually came true, but under conditions of error field suppression—a requirement that had not been theoretically predicted beforehand.

Convincing experimental evidence that a slowly growing or saturated $n = 1$ perturbation (where n is the toroidal wavenumber) measured outside the plasma in DIII-D was the plasma response to the static resonant error field was presented for the first time in [6]. It was shown that the plasma response to such a field was much stronger for $\beta > \beta^{\text{no wall}}$. The discovered effect became an interesting new object of research [6, 8–10] and was called "resonant field amplification" (RFA) [8–10]. Now, it is a definitely established experimental fact that weak error fields play an important role in the RWM dynamics. However, a theory that could explain the observable effects has not yet been developed. When discussing RFA, paper [11] is usually cited. However, the model and results of [11] (which were recently confirmed in [12]) must be revised for reasons which are partially explained below. Here, we propose a different model of RFA.

The aim of this work is to analyze the error field amplification by a plasma. Actually, we discuss here the transition through the RWM stability boundary, in which case the effect is most pronounced.

In the cylindrical approximation, the amplitude of the (m, n) harmonic of the radial magnetic field perturbation at the wall, B_m, is described by the equation

$$\tau_w \frac{\partial B_m}{\partial t} = \Gamma_m B_m + 2\mu B_m^{\text{ext}}, \tag{1}$$

where $\tau_w = \mu_0 \sigma r_w d$ is the above-mentioned wall time; σ, r_w, and d are the conductivity, minor radius, and thickness of the wall, respectively; $\mu = |m|$; and B_m^{ext} is the part of B_m that is created by all the sources outside the shell (in the region $r > r_w$). In general, the field B_m^{ext} can be time-dependent. Here, we will consider the case of a static error field: $B_m^{\text{ext}} = B_m^{\text{er}} = \text{const}$. For definiteness, we assume that $B_m^{\text{er}} > 0$.

Equation (1) is a direct consequence of Maxwell's equations and Ohm's law for a conducting wall and long-wavelength perturbations (see [13] for details). Briefly, the derivation of Eq. (1) consists in integrating the radial component of the equation

$$\frac{\partial \mathbf{B}}{\partial t} = \nabla^2 \frac{\mathbf{B}}{\mu_0 \sigma} \tag{2}$$

through the wall, which is considered as a thin shell, and substituting the perturbation $B_r = b_m(r, t)\exp(im\theta - in\zeta)$ (where θ is the poloidal angle and $\zeta = z/R$ is an equivalent of the toroidal angle) or the sum of such harmonics into the right-hand side of the resulting equation. When deriving Eq. (1), we use explicit expressions for b_m in the vacuum regions on both sides of the wall:

$$b_m = B_m^{pl} x^{-\mu-1} + (B_m^w + B_m^{\text{ext}}) x^{\mu-1} \tag{3}$$

for $x = r/r_w < 1$ and

$$b_m = (B_m^{pl} + B_m^w) x^{-\mu-1} + B_m^{\text{ext}} x^{\mu-1} \tag{4}$$

for $x > 1$. Here, $B_m = b_m(r_w)$ and the time-dependent complex amplitudes B_m^{pl} and B_m^w describe the contributions to $B_m(t)$ from the plasma and wall, respectively. In this notation, we have

$$\Gamma_m = -2\mu(1 - B_m^{pl}/B_m). \tag{5}$$

In Eq. (1), all information about the plasma is contained in the parameter Γ_m. According to Eq. (5), this parameter is determined by the ratio B_m^{pl}/B_m, which can be found, e.g., by calculating the perturbation in the plasma. In the linear theory, the radial profile $b_m(r)$ in a plasma depends only on the properties of the unperturbed equilibrium configuration, thus allowing one to consider Γ_m independent of B_m. The invariance of the mode structure in the plasma (mode rigidity) with respect to variations in B_m that are typical of experiments is confirmed by both the exact MHD calculations and the results of DIII-D experiments [7]. Note that the exact matching of Γ_m to the experimental conditions is also possible without calculations because Γ_m has a simple physical meaning. It follows from Eq. (1) that

$$\Gamma_m = \tau_m(\gamma_0 + in\Omega_0), \tag{6}$$

where γ_0 is the growth (or damping) rate of the mode and Ω_0 is the angular frequency of its toroidal rotation. In experiments, γ_0 increases with increasing β and passes through the point $\gamma_0 = 0$ at $\beta = \beta^{\text{no wall}}$. The transition through the stability boundary $\gamma_0 = 0$ can also be attributed to variations in the profile and/or magnitude of the plasma current.

Without a plasma, we have $\Gamma_m = \Gamma_m^0 = -2\mu$, so that, at $B_m^{\text{ext}} = B_m^{\text{er}} = \text{const}$, Eq. (1) has a stationary solution $B_m = B_m^{\text{er}}$. The plasma changes the value Γ_m; hence, the magnitude of the stationary solution also changes. At $\Gamma_m = \text{const}$ and $\text{Re}\,\Gamma_m < 0$ (otherwise, a stable stationary solution is absent), we have

$$B_m^{st} = -\frac{2\mu}{\Gamma_m} B_m^{\text{er}}. \tag{7}$$

This equality shows that the plasma response to the static external resonant field is stronger for smaller $|\Gamma_m|$. At $|\Gamma_m| < 2\mu$, it gives $|B_m^{st}| > B_m^{\text{er}}$, which can be regarded as the amplification of the resonant field. The most dangerous point here is $\Gamma_m = 0$, which corresponds to a nonrotating mode at its stability boundary. In the DIII-D

experiments, such modes are observed even in the presence of fast plasma toroidal rotation [4].

Large perturbations are inadmissible in experiments, which necessitates the struggle with MHD instabilities, first of all, with low-*n* modes. In this context, the most dangerous is the region $\gamma_0 > 0$. However, it follows from Eq. (7) that, even in the stability range ($\gamma_0 = \mathrm{Re}\Gamma_m/\tau_m < 0$), the value of B_m^{st} can exceed an acceptable level. The growth of B_m at $\gamma_0 < 0$ is related to the transition to a new equilibrium state with $B_m = B_m^{st}$. Within the model at hand, this state remains stable with respect to the considered mode, which resonates with the error field; however, the large values of B_m imply undesirable deformations of the plasma column and a danger of loss of equilibrium.

It was stated in [11] (and this viewpoint was confirmed once again in [12]) that the magnetic field perturbation near marginal stability can be accurately approximated by a stationary solution similar to that given by Eq. (7). Formally, the "amplification factor" in Eq. (7) can become infinite at $\Gamma_m \longrightarrow 0$. However, as $|\gamma_0|$ decreases, the time ($\sim|\gamma_0|^{-1}$), which is required to achieve the stationary level B_m^{st} from any initial B_m^0, increases. Therefore, however slow the evolution of the tokamak discharge might be, steady-state level (7) will never be achieved in the immediate vicinity of the point $\Gamma_m = 0$. This directly follows from Eq. (1). In other words, at $\Gamma_m \longrightarrow 0$, we must retain the time derivative in Eq. (1) and RFA cannot be regarded as a quasi-stationary phenomenon, as was done in [11, 12].

Actually, solution (7) shows a danger of long stay in the vicinity of $\Gamma_m = 0$, where the growth of B_m can proceed up to level (7) if there is enough time for that. At $\Gamma_m = 0$ and $B_m^{\mathrm{ext}} = B_m^{\mathrm{er}} = \mathrm{const}$, Eq. (1) has a linearly growing solution

$$B_m = B_m^0 + 2\mu B_m^{\mathrm{er}}\frac{t}{\tau_w}. \qquad (8)$$

Such a growth of B_m is not dangerous over small time intervals; however, at $t \gg \tau_w$, it results in practically unlimited values of B_m. For example, for the $m = 2$ mode at $t = 25\tau_w$, which is much smaller than the discharge duration in the DIII-D tokamak [8, 9], the amplification factor in Eq. (8) is 100. Let B_m^{tol} be the maximum tolerable value of B_m. Then, the condition $B_m < B_m^{\mathrm{tol}}$ with account of Eq. (8) turns into a rather tough restriction

$$B_m^{\mathrm{er}}\Delta t < \tau_w B_m^{\mathrm{tol}}/2\mu. \qquad (9)$$

At given B_m^{er}, it sets the upper limit for Δt (the time during which the RWM stability boundary is crossed at $\Omega_0 = 0$), and, at given Δt, it imposes a restriction on B_m^{er}. For example, if $B_m^{\mathrm{tol}} = 40B_m^{\mathrm{er}}$, then, for the $m = 2$ mode, we obtain $\Delta t < 10\tau_w$.

Solution (8) can be used when $|\Gamma_m B_m| \ll 2\mu B_m^{\mathrm{er}}$, which, at $B_m^0 = 0$ in formula (8), is reduced to

$$|\Gamma_m t| \ll \tau_w. \qquad (10)$$

If Γ_m evolves toward $\Gamma_m = 0$, condition (10) for t becomes weaker, thus making the applicability range of solution (8) wider. Formula (8) is valid for any Γ_m satisfying inequality (10). This means that the amplification of the resonant error field can be observed not only at the stability threshold of a "conventional" RWM, but also in the vicinity of all other zeros of Γ_m. An important point in our task is the interaction of the plasma-produced perturbation with the wall. Therefore, the RWM should be regarded here as a generic name for all such perturbations, including those destabilized not only by the plasma pressure, but also by the current.

In any case, the RFA effect is the strongest when the mode does not rotate ($\Omega_0 = 0$). The rotation of the mode eliminates the singularity in Eq. (7) and reduces the time t during which the linear growth of B_m is possible (see Eqs. (8) and (10)). Note that we talk here about the toroidal rotation frequency of the magnetic perturbation, which can be measured by magnetic probes. In DIII-D experiments, the observed RWM frequency was substantially lower than the plasma rotation frequency Ω_p. According to [4], the experimentally observed toroidal rotation is such that $\Omega_0 \sim \tau_w^{-1} \ll \Omega_p$, starting from the RWM onset.

Equation (1) is a consequence of Maxwell's equations and Ohm's law for the conducting wall; therefore, it contains only the wall parameters (τ_w) and the characteristics of the perturbed magnetic field. In [11], the problem is formulated in other terms—certain parameters s and α, which are related to γ_0 and Ω_0 in a rather complicated fashion even in the cylindrical model. Probably, it is for this reason that the following obvious contradiction was not noticed in [11]: at $s = 0$, which, by definition, is the stability boundary in [11], $\gamma_0 \neq 0$ if $\Omega_0 \neq 0$. As a consequence, in [11] the position of the strongest RFA is displaced relative to the point $\gamma_0 = 0$ along the γ_0 axis. The coincidence takes place only at $s = \alpha = 0$; however, in this case, one must use equality (8) instead of an absolutely unattainable solution (similar to Eq. (7)) that was proposed in [11].

The B_m value given by formula (8) becomes a "seed" amplitude of an unstable RWM after crossing the RWM stability threshold. The smaller this value, the better. Relationships (7)–(9) show three opportunities to oppose the growth of the seed perturbation B_m as the RWM instability region is approached: the sustainment of the mode toroidal rotation (not the plasma rotation!),

the fast crossing of the subthreshold zone in the immediate vicinity of the point $\gamma_0 = 0$, and the reduction of $B_m^{\rm er}$.

It is rather difficult to completely eliminate $B_m^{\rm er}$. Let us assume that two other means allowed us to enter the area $\beta > \beta^{\rm no\ wall}$ (more precisely, $\gamma_0 > 0$) keeping the value B_m small. Further progress toward larger β requires RWM stabilization. Let us consider the feedback system of RWM stabilization, which produces a control signal

$$B_m^f = -\tau_w K_d \frac{\partial B_m}{\partial t} - K_p(B_m - B_n^{\rm er}), \qquad (11)$$

where K_d and K_p are constants. Substituting

$$B_m^{\rm ext} = B_m^f + B_m^{\rm er} \qquad (12)$$

into Eq. (1), we arrive at the equation

$$\frac{\tau_w^*}{2\mu}\frac{\partial B_m}{\partial t} = -(\Gamma_m/\Gamma_m^0 + K_p)B_m + (1 + K_p)B_m^{\rm er}, \qquad (13)$$

which differs from Eq. (1) in coefficients only (recall that $\Gamma_m^0 = -2\mu$). All the above said about the consequences of Eq. (1) at $B_m^{\rm ext} = B_m^{\rm er}$ is also valid for the solution of Eq. (13) if $\tau_w^* \equiv (1 + 2\mu K_d)\tau_w \neq 0$. Instead of Eq. (7), we obtain in this case

$$B_m^{st} = \frac{1 + K_p}{\Gamma_m/\Gamma_m^0 + K_p} B_m^{\rm er}, \qquad (14)$$

which still keeps a danger of RFA, but now near a new threshold, where the mode becomes unstable at a given operation algorithm of the stabilizing system, described by Eq. (11). To suppress the unstable nonrotating mode, it is sufficient to make zero the quantity $\Gamma_m/\Gamma_m^0 + K_p$, more precisely, to make it slightly positive. Then, the "amplification factor" in Eq. (14) will obviously be larger than unity, going to infinity at $\Gamma_m/\Gamma_m^0 = -K_p$. The growth of B_m at the RWM stability boundary under active stabilization of the mode is described by formula (8), where we must substitute τ_w^* instead of τ_w.

Thus, the danger of RFA requires the fast crossing of the RWM stability boundary (accordingly, the high heating power) and large gain factors of the feedback system for active stabilization of RWMs. The mode rotation eliminates the possibility of the unlimited amplification of the resonant field. If the rotation could be controlled and mode locking [1] could be avoided, this rotation would be an effective means of RFA suppression at $|n\Omega_0\tau_w| \geq 2\mu$. However, in the DIII-D tokamak, the RWM appears as a stationary mode, which is clearly seen from magnetic measurements [4]. Besides, as it is believed now, the thresholds for mode locking will be lower in larger tokamaks [1]. Therefore, the only radical means of struggle with RFA is the reduction of the error field, which is the basic reason of RFA.

It follows from Eqs. (1) and (13) that, at $B_m^{\rm er} \neq 0$, it is impossible to achieve a state with $B_m = 0$. Even at a very small value of $B_m^{\rm er}$ and, accordingly, small growth rate of B_m in Eq. (8), strong amplification of the error field is possible if the discharge evolves slowly. Therefore, the error field problem demands special attention in projecting stationary tokamaks.

The author is grateful to Yu.V. Gribov and V.S. Mukhovatov for bringing his attention to the problem and encouraging the study, N.V. Ivanov for the support, and V.D. Shafranov for the discussion of the results obtained and useful recommendations.

REFERENCES

1. ITER Physics Basis, Nucl. Fusion **39**, 2137 (1999).
2. T. C. Luce, M. R. Wade, P. A. Politzer, *et al.*, Nucl. Fusion **41**, 1585 (2001).
3. E. J. Strait, T. S. Taylor, A. D. Turnbull, *et al.*, Phys. Rev. Lett. **74**, 2483 (1995).
4. A. M. Garofalo, A. D. Turnbull, E. J. Strait, *et al.*, Phys. Plasmas **6**, 1893 (1999).
5. A. M. Garofalo, E. J. Strait, J. M. Bialek, *et al.*, Nucl. Fusion **40**, 1491 (2000).
6. A. M. Garofalo, M. S. Chu, E. D. Fredrickson, *et al.*, Nucl. Fusion **41**, 1171 (2001).
7. M. Okabayashi, J. Bialek, M. S. Chance, *et al.*, Phys. Plasmas **8**, 2071 (2001).
8. A. M. Garofalo, T. H. Jensen, L. C. Johnson, *et al.*, Phys. Plasmas **9**, 1997 (2002).
9. M. Okabayashi, J. Bialek, M. S. Chance, *et al.*, Plasma Phys. Controlled Fusion **44**, B339 (2002).
10. A. M. Garofalo, R. J. La Haye, and J. T. Scoville, Nucl. Fusion **42**, 1335 (2002).
11. A. H. Boozer, Phys. Rev. Lett. **86**, 5059 (2001).
12. A. H. Boozer, Phys. Plasmas **10**, 1458 (2003).
13. V. D. Pustovitov, Fiz. Plazmy **27**, 209 (2001) [Plasma Phys. Rep. **27**, 195 (2001)].

JETP Letters, Vol. 78, No. 5, 2003, pp. 285–290. Translated from Pis'ma v Zhurnal Éksperimental'noĭ i Teoreticheskoĭ Fiziki, Vol. 78, No. 5, 2003, pp. 731–736.

Second Harmonic Generation in Plasma in the Presence of SBS

I. V. Khazanov

Institute of Applied Physics, Russian Academy of Sciences, ul. Ul'yanova 46, Nizhni Novgorod, 603950 Russia

Received July 7, 2003; in final form, July 23, 2003

The mechanism of second harmonic generation in the presence of intense-radiation SBS in plasma is considered under the condition that the incident beam has no time for filamentation. The mechanism is based on the formation of low-frequency plasma-density perturbations that are optimal for this effect in the field of scattered waves. The theoretical calculations are compared with the experimental data. © *2003 MAIK "Nauka/Interperiodica".*

PACS numbers: 52.38.-r; 42.65.Ky

From the very outset of inquiries into nonlinear phenomena, much attention has been given to the harmonic generation for an intense fundamental (pump) wave $\mathbf{E}_\omega = \mathbf{E}_\omega^\circ \exp[-i(\omega t - \mathbf{kr})]$ (ω is fundamental frequency and $\mathbf{k}$ is wave vector) propagating in nonlinear media. This problem is of considerable interest both as a possible method of generating shorter-wavelength radiation and for diagnostic purposes, because it aids in gaining information both on the substance of interest and on the processes occurring in it under the action of strong electromagnetic fields. To date, many mechanisms of this phenomenon have been proposed; various theoretical models have been developed; and many experimental results are now available. It has become clear as early as in pioneering works [1] that, in the electric dipole approximation, only odd harmonics can be generated in homogeneous isotropic centrosymmetric media. Simultaneously, the entire spectrum of odd harmonics in a dense plasma with "collisional" (dissipative) nonlinearity [2] was obtained (see also [3]).

Interest in harmonic generation has quickened in the latter half of 1980s in connection with experiments (see, e.g., [4]) on the action of intense subpicosecond laser pulses on rarefied gases, in which a broad spectrum of odd harmonics was generated. These results were interpreted both with the simplest classical atomic model [5, 6] and using a more rigorous semiclassical consideration of electron scattering by its own ion with allowance for the electron optical tunneling in a strong laser field [7]. The problem of such harmonics was also studied in plasma with relativistic nonlinearity [8].

At the same time, in anisotropic or inhomogeneous media, even harmonics can also be generated. For instance, in plasma with a sharp and strong concentration change induced by the striction force of a high-intensity laser wave in the critical (relative to pumping) density region, an all-harmonic (even and odd) spectrum was calculated in [9]. In this case, the mechanism of harmonic radiation can likely be interpreted as a certain analogue of the transient radiation of particles moving with varying (oscillating) velocity. We finally note that this effect can be significantly amplified in nonlinear parametric harmonic generation if the transition frequency between the molecular energy levels in the medium coincides with the harmonic frequency [10].[1]

As a rule, first harmonics are observed and analyzed more easily, because they are induced by low-order nonlinearities. This is also true, in full measure, for the second harmonic of a radiation propagating in plasma, which is considered in this work.

In the case of a homogeneous plasma with density N_0, the nonlinear current appearing at the frequency 2ω can readily be determined from the hydrodynamical equations using the well-known relations for the operator ∇, $\mathbf{j}_{2\omega} = (-ieN_0/8\omega)\nabla(\mathbf{V}_\omega\mathbf{V}_\omega)$ ($\mathbf{V}_\omega = ie\mathbf{E}_\omega/m\omega$ is the electron oscillation velocity in the field $\mathbf{E}_\omega$; cf. [11]); it is a purely potential quantity ($\mathrm{curl}\mathbf{j}_{2\omega} \equiv 0$) and, thus, cannot produce transverse waves. However, this is possible in an inhomogeneous plasma, in which, nevertheless, the detuning of the first and second-harmonic wave vectors from the well-known phase-matching condition should be taken into account (due to the dispersion of electromagnetic waves in plasma, $\mathbf{k}(2\omega) \neq 2\mathbf{k}(\omega)$). For this reason, the second harmonic can be efficiently generated in those regions where the semiclassical approximation (valid if the plasma density varies slower than the wavelength) breaks and the phase-matching conditions become less significant [12, 13]. In plasma, these are the regions of (pump) wave reflection points and critical density. The decay mechanism of second harmonic generation in the critical density region, where the pump wave first decays into the plasma and ion-sound waves, whereupon the plasma waves coalesce into a wave with frequency close to 2ω, was considered in [14, 15]. The inhomogeneities in the

[1] I am grateful to the referee for drawing attention to the cited works.

0021-3640/03/7805-0285$24.00

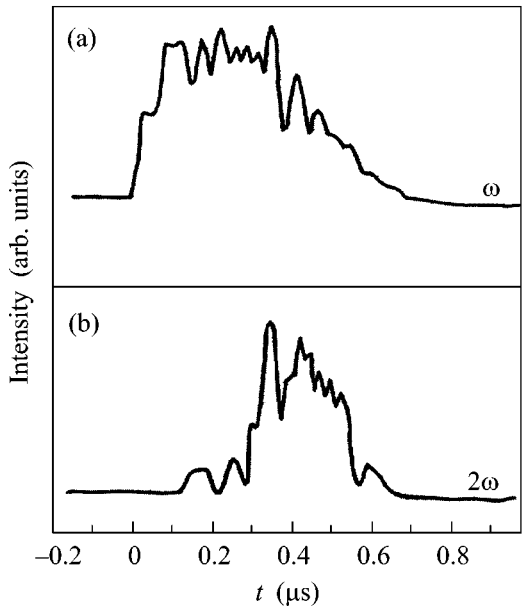

Radiation intensity transients for the (a) fundamental and (b) doubled frequencies (intensity (b) is grossly enlarged).

initially homogeneous plasma can be due to the nonlinear effects, e.g., to the self-focusing instability (filamentation) of intense radiation. This mechanism was proposed in [16] and is likely confirmed by the experiment [17, 18] (see also [19, 20], where the second harmonic generation was attributed to the formation of a region of reduced electron density (cavity) that appears on the background of immobile ions under the action of a ponderomotive force in the focal spot of a short and very intense ($V_\omega \sim c$) laser pulse). Finally, second harmonic generation caused by second-order stimulated Raman scattering (SRS), in which the transverse and plasma waves are produced through the decay of the pump second harmonic (rather than the pump wave itself) representing a stimulated longitudinal wave generated in a homogeneous plasma by the current $\mathbf{j}_{2\omega}$, was studied in [21] (see above; cf. [22], where the second harmonic generation was studied in optically active liquids with taking into account high-order nonlinearities).

In this work, interpretation is given to the second harmonic generation in the experiments [23, 25] on the stimulated microwave scattering in plasma. The plasma concentration was virtually uniform over a large volume of (diameter) ~60 cm × (length) 300 cm, and plasma was transparent with $N_0 \sim 6 \times 10^{11}$ cm$^{-3} \sim 0.5N_{cr}$ ($N_{cr} = m\omega^2/4\pi e^2$ is the critical density); the microwave (pump) pulse duration $\tau \sim 0.4$ μs ($\omega \sim 6 \times 10^{10}$ s^{-1}) was short, though not sufficient for self-focusing, and the pulse power $P_0 \sim 30$ MW ($V_\omega \sim 0.01c$) was far from relativistic. In those experiments, apart from the SBS, a frequency-doubled radiation was observed, with the maximum at the pump pulse end (see figure). The electromagnetic radiation (weakly diverging beam) was focused in plasma at a distance of ~130 cm from the chamber entrance window. The radius of the resulting pump caustic was $a \approx 16$ cm, and its length was $l_0 = ka^2/2 \approx 180$ cm. The beam intensity distribution over the caustic cross section was gaussian. In the longitudinal direction, the intensity changed only slightly from the focus (caustic center) up to the lengths $\approx l_0/2$ in the direction of the entrance window (it changed somewhat more strongly in the opposite direction; cf. a similar dependence for the self-focused gaussian beam in [26]). Radiation at frequency 2ω was received by a horn antenna that was placed behind the focus at a distance of 30 cm from it and at 20 cm up from the chamber axis. The horn was directed at 30° to this axis (denoted by the z axis). Taking these facts into account, one can determine the attainable second harmonic intensity.

Considering that the process of second harmonic generation is not one-dimensional and nonresonant, it is more convenient and correct to use, especially in our case of a moderate supercriticality ($\omega^2/\omega_{pe}^2 = N_{cr}/N_0 \sim 2$, where ω_{pe} is the electron plasma frequency), directly the solution to the wave equation for retarded potentials (**A**; see, e.g., [27] and cf. [9, 16]), rather than the method of reduced equations (see, e.g., [11]). Then the magnetic field curl$\mathbf{A}_{2\omega}$ of the wave at frequency 2ω is represented in the form

$$\mathbf{B}_{2\omega} = \frac{e^{i2k_0 r}}{cr}\int dz e^{-i2k_0 z\cos\gamma}\int \rho d\rho \int d\varphi \times \mathbf{I}_{2\omega}(z, \rho, \varphi, t)e^{-i2k_0\rho\sin\gamma\cos(\varphi-\varphi_0)}. \quad (1)$$

It can be used to determine the electric field outside the sources

$$\mathbf{E}_{2\omega} = \frac{i}{2k_0}\mathrm{curl}\mathbf{B}_{2\omega}. \quad (2)$$

In Eq. (1), the well-known approximation to the exact solution for the vector potential **A** is used for the case that the source ($\mathbf{I}_{2\omega}$) size $d \ll r$ (r is the distance to the observation point; see below); γ is the angle between the radius vector **r** and the z axis (see above); ρ, φ, and z are the cylindrical coordinates (the angle φ is measured from the vertical direction with which the pump electric vector $\mathbf{E}_\omega$ is aligned in the caustic region); φ_0 is the φ coordinate of the observation point; and $\mathbf{I}_{2\omega}$ is a function of the nonlinear current density, for which one can use any of the expressions

$$\mathbf{I}_{2\omega} = \begin{cases} i2k_0\dfrac{\mathbf{r}}{r}\times\mathbf{j}_{2\omega} \\ \mathrm{curl}\,\mathbf{j}_{2\omega,} \end{cases} \quad (3)$$

where $k_0 = \omega/c$. The first of them is evident from Eq. (1), and the second is obtained through the transi-

tion in the integrand of the exact solution for curl$\mathbf{A}_{2\omega}$ to the operator ∇ acting on the integration variables, followed by the use of a familiar curl integral theorem that relates the volume and surface integrals to each other.[2] By the way, Eq. (3) reflects the well-known fact in electrodynamics that the curl-free current cannot produce a curl field.

The nonlinear current density $\mathbf{j}_{2\omega}$ in Eq. (3) is the sum of two terms

$$\mathbf{j}_{2\omega} = \frac{1}{2}en_\omega\mathbf{V}_\omega - \frac{ie}{8\omega}\left(N_0 + \frac{1}{2}n_\Omega\right)\times\nabla(\mathbf{V}_\omega\times\mathbf{V}_\omega), \quad (4)$$

where n_ω stands for the high-frequency electron-density perturbations resulting from the continuity equation and the condition that the pump wave is transverse (div$\mathbf{V}_\omega = 0$),[3]

$$n_\omega = \frac{1}{2}\frac{1}{i\omega}\mathbf{V}_\omega\times\nabla n_\Omega. \quad (5)$$

One can readily see that the second term in Eq. (4) for the nonlinear current density transforms at $n_\Omega = 0$ into the expression for $\mathbf{j}_{2\omega}$ in a homogeneous plasma.

It is worth noting that, in general, the rapidly oscillating exponentials in the integrand in Eq. (1) greatly suppress the contribution from the source to the frequency-doubled radiation. For this reason, those currents whose structures compensate, to some extent, these oscillations will radiate more efficiently. For instance, at the left caustic portion closer to the boundary, one has $\cos\gamma \simeq 1$ for a sufficiently long length under the above-mentioned reception conditions, whereas $V_\omega^2 \propto e^{i2kz}$ ($k_0 \approx 1.5k$ for $N_{cr}/N_0 \approx 2$) under the above-mentioned reception conditions. Because of this, if $n_\Omega \propto e^{ikz}$ (see Eqs. (4), (5)), the oscillations along z virtually disappear over a considerable integration interval in Eq. (1).[4] At the same time, $\sin\gamma$ in the second exponent in Eq. (1) is relatively small in this region. It is also significant that the pump field in this region is more intense and decreases noticeably along the z axis due to a rather strong stimulated Brillouin backscattering in the experiments [23–25]. It follows from the aforesaid that, to estimate the radiation received at frequency 2ω in the cited experiments, it, probably, suffices to consider the currents only in the indicated portion of pump caustic. The low-frequency plasma-density perturbations n_Ω with the wave vector $\boldsymbol{\kappa}$ arise in the field of pump beats and scattered waves. Therefore, when setting $\kappa_z = k$, one must assume that the corresponding scattered wave (denoted by $\tilde{\mathbf{E}}_\omega$) has the wave vector $\mathbf{k}_1 \perp \mathbf{z}$ ($\mathbf{k} = \mathbf{k}_1 + \boldsymbol{\kappa}$, $\mathbf{k} \parallel \mathbf{z}$, $|\mathbf{k}_1| \simeq |\mathbf{k}|$) and, hence, propagates transverse to the pump beam.[5] Therefore, the gaussian pump-beam field and the density perturbation n_Ω in the region of interest take the form

$$\mathbf{E}_\omega \simeq \mathbf{E}_\omega^\circ(z, t)e^{-\rho^2/a^2}e^{-i(\omega t - kz)},$$
$$n_\Omega \simeq n_\Omega^\circ(z, \rho, \varphi, t)e^{i(\kappa_x\rho\cos\varphi - \kappa_y\rho\sin\varphi + kz)}, \quad (6)$$

where $\mathbf{E}_\omega^\circ(z, t)$ and $n_\Omega^\circ(z, \rho, \varphi, t)$ are the slowly varying (compared to the next exponentials in Eq. (6)) functions of their arguments.[6]

The contributions $\mathbf{j}_{2\omega}^{(1)}$ and $\mathbf{j}_{2\omega}^{(2)}$ to the radiation from, respectively, the first and second terms in the expression for the nonlinear current density can conveniently be determined using, respectively, the first and second expressions for $\mathbf{I}_{2\omega}$ in Eq. (3). One can then readily see that the function $\mathbf{I}_{2\omega}$ reaches its maximal values at not small κ_x ($\kappa_x \sim \kappa_y$), with the contribution from $\mathbf{j}_{2\omega}^{(1)}$ exceeding the contribution from $\mathbf{j}_{2\omega}^{(2)}$ by several times. For this reason, only the first term $\mathbf{j}_{2\omega}^{(1)}$ will be taken below into account for the nonlinear current density $\mathbf{j}_{2\omega}$. By substituting $\mathbf{j}_{2\omega}^{(1)}$ into Eq. (1), one obtains, according to Eqs. (3)–(6)

$$\mathbf{B}_{2\omega} \approx \frac{ie^{i(2k_0r - 2\omega t)}}{cr}\frac{ek_0}{2\omega}\kappa_x\mathbf{y}_0$$
$$\times\int_{\Delta z} dz(\mathbf{V}_\omega^\circ)^2\int_0^\infty d\rho\rho e^{-2\rho^2/a^2}\int_0^{2\pi} d\varphi n_\Omega^\circ$$
$$\times e^{-i(k/2 - \kappa_x)\rho\cos\varphi - i\kappa_y\rho\sin\varphi}, \quad (7)$$
$$\sqrt{\kappa_x^2 + \kappa_y^2} = k_1$$

[2] The integration surface is chosen so that the sources (currents) at it can be taken to be zero.

[3] In Eq. (4), the analogous terms involving electron velocity in the field of a strong backscattered Stokes wave are omitted, because their contribution to the frequency-doubled radiation is insignificant (see below). Note also that the relatively small difference between the frequency of these terms and the pump frequency ω is hereafter ignored in the notation of the corresponding high-frequency quantities, because this difference is equal, by the order of magnitude, to the reciprocal characteristic time of the low-frequency plasma-density perturbations $n_\Omega(z, \rho, \varphi, t)$ that are, in fact, responsible for the SBS of the pump wave. The multipliers 1/2 in Eqs. (4) and (5) appear upon the transition to the complex representation of physical quantities.

[4] As the focus is approached, the analogous condition becomes more restrictive, so that the length of this interval becomes smaller.

[5] In the experiment of interest, the SBS process evolved starting with some initial level that appeared as a result of the pump reflection inside the chamber from the microwave absorbers covering its end wall and the adjacent surface portions of the side walls, from the walls themselves, and from various structural members inside the chamber. The angular spectrum of spurious reflection in [23–25] was rather isotropic.

[6] More specifically, it is precisely the beam central portion which is "eaten out" along the path at the nonlinear SBS stage [25]. However, one can easily verify from further calculations that this fact is immaterial for the analysis of various properties of the phenomena under discussion. Note also that, for the sake of convenience, the Cartesian coordinates with the vertical axis x are also introduced in Eq. (6) and in what follows. They are related to the cylindrical coordinates by the simple expressions $x = \rho\cos\varphi$ and $y = -\rho\sin\varphi$.

(it is considered that, under the above-mentioned experimental conditions, one has $k_0 \approx 1.5k$, $\varphi_0 = 0$, and $\sin\gamma \approx 1/6$). It must be kept in mind that the generation of low-frequency plasma-density perturbations in the process of interest has a local character because of a small pump-pulse duration [25]; i.e., $n_\Omega \propto |\mathbf{E}_\omega| \times |\tilde{\mathbf{E}}_\omega| \times \cos\alpha$ ($\alpha \equiv \angle(\mathbf{E}_\omega, \tilde{\mathbf{E}}_\omega)$). At the same time, the amplification of the $\tilde{\mathbf{E}}_\omega$ field also reduces with decreasing $|\cos\alpha|$. However, the oscillations in the integrand in Eq. (7) become slower in this case, because $|\kappa_y| = |k_{1y}| = |k_1\cos\alpha|$ (see above; it is assumed that $\tilde{\mathbf{E}}_\omega \perp \mathbf{z}$, as for $\mathbf{E}_\omega$, and $\mathbf{k}_1 \perp \tilde{\mathbf{E}}_\omega$). As a result, it turns out that, excepting the regions where $\kappa_x \ll k_1$ and $k_1 - \kappa_x \ll k_1$, the perturbations n_Ω with $\kappa_x > 0$ ($\kappa_x = -k_{1x}$, $|\kappa_x| = k_1|\sin\alpha|$) give approximately the same value for $\mathbf{B}_{2\omega}$ in Eq. (7). For definiteness, we obtain it below for $\kappa_x = k/2$.

The integral with respect to φ in Eq. (7) can be approximately evaluated using the following method. After representing the exponential of a complex argument through the real and imaginary parts, we first evaluate $\int_0^{2\pi} d\varphi n_\Omega^\circ \cos(\zeta\sin\varphi)$, where $\zeta \equiv \kappa_y\rho$ ($\kappa_y \simeq k\sqrt{3}/2$, $\kappa_x = k/2$). To this end, we divide the entire integration domain $[0, 2\pi]$ into four segments: $[5\pi/3, \pi/3]$, $[\pi/3, 2\pi/3]$, $[2\pi/3, 4\pi/3]$, and $[4\pi/3, 5\pi/3]$. On the interval $[0, \pi/3]$, we expand the function $\sin\varphi$ into the Taylor series and retain only the two leading terms in it. In further integration on this interval, the $\cos(\zeta\varphi)$ and $\sin(\zeta\varphi)$ are assumed to be rapidly oscillating functions, as compared to n_Ω°, $\cos(\zeta\varphi^3/6)$, and $\sin(\zeta\varphi^3/6)$. This allows the approximate integration of the expression by parts (see, e.g., [28]). On the interval $[5\pi/3, 2\pi]$, one should preliminarily replace $\sin\varphi \equiv -\sin(2\pi - \varphi)$, after which the entire procedure is repeated. The integration on the interval $[2\pi/3, 4\pi/3]$ is carried out in a similar way. After replacing $\sin\varphi \equiv \cos(\pi/2 - \varphi)$ on the interval $[\pi/3, 2\pi/3]$, the cosine is expanded into the Taylor series, and it again suffices to retain only the two leading terms. When integrating on this interval, one should take into account not only that n_Ω° is a slowly varying function but also that this interval is comparatively small. The analogous situation occurs on the interval $[4\pi/3, 5\pi/3]$.

As a result, we obtain

$$\int_0^{2\pi} n_\Omega^\circ(\rho, \varphi)\cos(\zeta\sin\varphi)d\varphi \approx \left[\frac{1}{\zeta}\sin\left(\frac{5}{6}\zeta\right) + \sqrt{\frac{\pi}{\zeta}}\cos\zeta C(\zeta/8) + \sqrt{\frac{\pi}{\zeta}}\sin\zeta S(\zeta/8)\right] \times \sum_{\nu = 1, \nu \neq 3}^{5} n_\Omega^\circ(\rho, \nu\pi/3), \quad (8)$$

where C and S are, respectively, the Fresnel cosine and sine integrals [29], and, for brevity, the z and t dependences (6) are not indicated for n_Ω°.

Next, this expression should be integrated, according to Eq. (7), over ρ. The functions $\sin\zeta$ and $\cos\zeta$ can again be considered rapidly oscillating, as compared to n_Ω° and $\exp(-2\rho^2/a^2)$. Then, after the approximate integration analogous to the one performed above, one obtains[7]

$$\int_0^\infty d\rho\rho e^{-2\rho^2/a^2}\frac{1}{\zeta}\sin\left(\frac{5}{6}\zeta\right) \times \sum_{\nu = 1, \nu \neq 3}^{5} n_\Omega^\circ(\rho, \nu\pi/3) \approx \frac{5}{\kappa_y^2}n_\Omega^\circ \quad (\rho = 0). \quad (9)$$

Here and in the analogous integration of the remaining two terms in the square brackets in Eq. (8), one should keep in mind that, in our case, $n_\Omega \propto (\mathbf{E}_\omega \times \tilde{\mathbf{E}}_\omega)$ (see above), and the magnitude $|\mathbf{E}_\omega|$ is maximal in the beam center ($\rho = 0$) (see Eq. (6)). At the same time, the amplification of the reflected-wave field $\tilde{\mathbf{E}}_\omega$ reduces on rows with distance from the center (with increasing ρ).

Similar to Eq. (9), the integration of the third term in the square brackets in Eq. (8) gives a value that is much smaller than Eq. (9). The second term in these brackets should be integrated more accurately, because the function $C(\zeta/8)$ increases rather rapidly at small ζ. Up to the point $\zeta_1/8 \sim 1$, one can put $C(\zeta/8) \approx (1/2)\sqrt{\zeta/\pi}$ and consider $\zeta\cos\zeta$ as a rapidly oscillating function in the resulting integral; as before, only $\cos\zeta$ can be considered rapidly oscillating in the remaining domain (to minimize error in the integration by parts, the integral containing derivatives of slowly varying functions should also be taken into account). One can then easily find that the value of the corresponding integral is half as large as in Eq. (9) and is opposite in sign.

The integral with the imaginary part of the exponential in Eq. (7), i.e., $\int_0^{2\pi} d\varphi n_\Omega^\circ \sin(\zeta\sin\varphi)$, is calculated in a similar way. The resulting expression differs from Eq. (8) by the replacement $\sin\zeta \longleftrightarrow \cos\zeta$ of the rapidly oscillating functions in it and also by a change in signs of some terms in $\sum_{\nu = 1, \nu \neq 3}^{5}$. The subsequent

[7] The upper limit in the integral in Eq. (9) is not too significant and denoted, by convention, as ∞.

integration with respect to ρ (see Eq. (7)) yields a value that is much smaller than the value given by Eq. (9).

Thus, Eq. (7) takes the following form:

$$\mathbf{B}_{2\omega} \approx ie^{i(2k_0 r - 2\omega t)} \frac{V_\omega^\circ}{c} \frac{e^2 n_\Omega^\circ (\rho = 0)}{m\omega^2} \times \frac{k_0 \kappa_x \Delta z}{\kappa_y^2} \frac{r}{} E_\omega^\circ \mathbf{y}_0. \quad (10)$$

Therefore, the value n_Ω° (ρ = 0) can be determined from the solution describing the linear stage of a modified wave decay in a layer [25]. Setting the wave interaction length equal to $a/\sqrt{2}$ and assuming that the "average" separation between the pump modes is on the order of the pump spectrum width $\Delta\omega \sim 2\pi \times 2$ MHz $\simeq 2\sqrt{2}\,\kappa v_s$ (v_s is the ion sound velocity), one obtains at the pulse length

$$\left|n_\Omega^\circ(\rho = 0, t)\right| \sim \left|\frac{V_\omega^{\circ 2} \tilde{\mathscr{E}}_\omega^\circ}{V_{T_e}^2 E_\omega^\circ}\right| 0.5\kappa^2 v_s^2 t^2 N_0, \quad (11)$$

where $V_{T_e} = (2T_e/m)^{1/2}$ is the electron thermal velocity and $\tilde{\mathscr{E}}_\omega^\circ$ is the initial (before amplification) amplitude of the scattered wave entering the pump caustic region.[8] Since, as is mentioned above, the initial level of the scattered waves was nearly isotropic, the value of $\tilde{\mathscr{E}}_\omega^\circ$ can be considered as corresponding to the experimentally observed strong stimulated Brillouin backscattering. Then, by taking maximal amplification over the entire caustic length l_0, one gets, according to [25], $|\tilde{\mathscr{E}}_\omega^\circ / E_\omega^\circ| \sim 1/60$. The radiation intensity at a doubled frequency reached its maximum value by the time $t_* \sim 0.3$ μs (see figure), when the SBS process was already at the nonlinear stage. In this case, the strong-field region Δz can be estimated both on the basis of the above-mentioned solutions and directly from the reduced equations for high-frequency waves using the experimentally measured relative plasma-density perturbations, which comprised ~5% at the pump pulse end ($t > t_*$) [23–25]. The value $\Delta z \sim 30$ cm seems to be quite reasonable. Considering the aforesaid and that $V_\omega^\circ \approx V_{T_e} \approx 2.5 \times 10^8$ cm/s, $\omega_{p_e}^2/\omega^2 \simeq 0.5$, $k_0 \simeq 2$ cm^{-1}, $\kappa_x \simeq 0.7$ cm^{-1}, $\kappa_y \simeq 1.2$ cm^{-1}, and $r \approx 120$ cm, one finds, according to Eqs. (10) and (11), that $|\mathbf{B}_{2\omega}^\circ| \sim 2 \times 10^{-6} \times |\mathbf{E}_\omega^\circ|$ at $t = t_*$. From these data and Eq. (2), one can easily see that

$$\left|\mathbf{E}_{2\omega}^\circ\right| \sim 2 \times 10^{-6} \left|E_\omega^\circ\right|, \quad \mathbf{E}_{2\omega}^\circ \parallel \mathbf{E}_\omega^\circ. \quad (12)$$

This value coincides, by the order of magnitude, with the experimentally observed $|E_{2\omega(\exp)}^\circ| \sim 3 \times 10^{-6} |E_\omega^\circ|$. The inclusion of the low-frequency perturbations n_Ω with different κ_x and κ_y (see above) would, likely, increase the value given by Eq. (12). Note also that the fact that the intensity of frequency-doubled radiation decreases slightly slower than the pump intensity at the pulse end (figure) is likely due to the growth of plasma-density perturbations with time (see Eq. (11)).

As the plasma density N_0 decreases, a structure resonant with the frequency-doubled wave can arise in the nonlinear current density $\mathbf{j}_{2\omega}$ under the action of the low-frequency perturbations with $\kappa_z < k$. They are produced by the scattered high-frequency waves propagating at acute angles to the *z* axis. From Eqs. (7) and (10) and considering that, in this case, $n_\Omega^\circ \propto \kappa^2 N_0$, one can readily find that $B_{2\omega} \propto N_0$. For an appreciable supercriticality $\omega^2 \gg \omega_{p_e}^2$ ($\kappa \ll k_0$), one has $B_{2\omega} \propto \kappa^3 N_0$; however, the 2ω wave in this region is radiated owing to the resonance with n_Ω generated with the participation of a pump-counterrunning backscattered wave. They make the greatest contribution to the radiation, and the corresponding component is $\mathbf{j}_{2\omega} \propto \mathbf{V}_\omega (\tilde{\mathbf{V}}_\omega \times \nabla n_\Omega)$; in this case, $B_{2\omega} \propto N_0$.

I am grateful to V.A. Isaev for interest in the work and helpful discussions.

REFERENCES

1. S. A. Akhmanov and R. V. Khokhlov, *Nonlinear Optics* (VINITI, Moscow, 1965; Gordon and Breach, New York, 1972).
2. V. P. Silin, Zh. Éksp. Teor. Fiz. **47**, 2254 (1964) [Sov. Phys. JETP **20**, 1510 (1964)].
3. V. P. Silin, Zh. Éksp. Teor. Fiz. **114**, 864 (1998) [JETP **87**, 468 (1998)]; Zh. Éksp. Teor. Fiz. **121**, 291 (2002) [JETP **94**, 244 (2002)].
4. A. McPherson, G. Gibson, H. Jara, *et al.*, J. Opt. Soc. Am. B **4**, 595 (1987).
5. S. M. Gladkov and N. I. Koroteev, Usp. Fiz. Nauk **160**, 105 (1990) [Sov. Phys. Usp. **33**, 554 (1990)].
6. R. V. Karapetyan and V. B. Fedorov, Kratk. Soobshch. Fiz., Nos. 7–8, 76 (1995).
7. P. B. Corkum, Phys. Rev. Lett. **71**, 1994 (1993).
8. E. Esarey, A. Ting, P. Sprangle, *et al.*, IEEE Trans. Plasma Sci. **21**, 95 (1993).
9. B. Bezzerides, R. D. Jones, and D. W. Forslund, Phys. Rev. Lett. **49**, 202 (1982).

[8] Up to $\kappa v_s t \approx 1$, one can write the sign "≈" between the left- and right-hand sides of Eq. (11), while, at larger *t*, n_Ω° increases somewhat faster than $\propto t^2$. Note that, at a constant amplitude $\tilde{E}_\omega^\circ = \tilde{\mathscr{E}}_\omega^\circ$ and the same Δω, $|n_\Omega^\circ|$ varies following the law $|n_\Omega^\circ(\rho = 0, t)| = 0.5 \left|(V_\omega^{\circ 2} \tilde{\mathscr{E}}_\omega^\circ)/(V_{T_e}^2 E_\omega^\circ)\right| N_0 \sin^2(\kappa v_s t)$.

10. V. S. Butylkin, A. E. Kaplan, Yu. G. Khronopulo, and E. I. Yakubovich, *Resonant Interactions of Light with Matter* (Nauka, Moscow, 1977).
11. V. N. Tsytovich, *Nonlinear Effects in Plasmas* (Nauka, Moscow, 1967; Plenum, New York, 1970).
12. N. S. Erokhin, V. E. Zakharov, and S. S. Moiseev, Zh. Éksp. Teor. Fiz. **56**, 179 (1969) [Sov. Phys. JETP **29**, 101 (1969)].
13. G. Auer, K. Sauer, and K. Baumgärtel, Phys. Rev. Lett. **42**, 1744 (1979).
14. N. G. Basov, Yu. V. Bychenkov, O. N. Krokhin, *et al.*, Kvantovaya Élektron. (Moscow) **6**, 1829 (1979).
15. R. P. Drake, B. S. Bauer, K. L. Baker, *et al.*, Phys. Plasmas **2**, 3473 (1995).
16. J. A. Stamper, R. H. Lehmberg, A. Schmitt, *et al.*, Phys. Fluids **28**, 2563 (1985).
17. I. V. Aleksandrova, A. E. Danilov, G. Korn, *et al.*, Pis'ma Zh. Éksp. Teor. Fiz. **38**, 478 (1983) [JETP Lett. **38**, 577 (1983)].
18. A. Giulietti, D. Giulietti, D. Batani, *et al.*, Phys. Rev. Lett. **63**, 524 (1989).
19. K. Krushelnick, A. Ting, H. R. Burris, *et al.*, Phys. Rev. Lett. **75**, 3681 (1995).
20. V. Malka, A. Modena, Z. Najmudin, *et al.*, Phys. Plasmas **4**, 1127 (1997).
21. K. Ramachandran, IEEE Trans. Plasma Sci. **24**, 487 (1996).
22. A. V. Balakin, D. Bushe, N. I. Koroteev, *et al.*, Zh. Éksp. Teor. Fiz. **112**, 97 (1997) [JETP **85**, 52 (1997)].
23. V. P. Denisov, N. I. Zaĭtsev, E. V. Ilyakov, *et al.*, Fiz. Plazmy **16**, 296 (1990) [Sov. J. Plasma Phys. **16**, 167 (1990)].
24. V. A. Isaev, Candidate's Dissertation in Physics and Mathematics (Inst. of Applied Physics, Russian Academy of Sciences, Nizhni Novgorod, 1992).
25. V. A. Isaev and I. V. Khazanov, Zh. Éksp. Teor. Fiz. **108**, 182 (1995) [JETP **81**, 97 (1995)].
26. V. M. Rysakov, Yu. V. Aristov, and V. I. Korotkov, Zh. Tekh. Fiz. **55**, 1955 (1985) [Sov. Phys. Tech. Phys. **30**, 1148 (1985)].
27. J. D. Jackson, *Classical Electrodynamics*, 2nd ed. (Wiley, New York, 1975; Inostrannaya Literatura, Moscow, 1965).
28. A. B. Migdal, *Qualitative Methods in Quantum Theory* (Nauka, Moscow, 1975; Benjamin, Reading, Mass., 1977).
29. E. Jahnke, F. Emde, and F. Lösch, *Tables of Higher Functions*, 6th ed. (McGraw-Hill, New York, 1960; Nauka, Moscow, 1968).

Translated by V. Sakun

JETP Letters, Vol. 78, No. 5, 2003, pp. 291–295. Translated from Pis'ma v Zhurnal Éksperimental'noĭ i Teoreticheskoĭ Fiziki, Vol. 78, No. 5, 2003, pp. 737–741.

A Cavitation Mechanism of Material Sputtering by Slow Multicharged Ions

V. S. Vorob'ev[1, *], V. S. Lisitsa[2], and S. P. Malyshenko[3]

[1]*Institute for High Energy Densities, Associated Institute for High Temperatures, Russian Academy of Sciences, Moscow, 127412 Russia*

**e-mail: vrbv@mail.ru*

[2]*Kurchatov Institute of Atomic Energy, State Scientific Center of the Russian Federation, Moscow, 123182 Russia*

[3]*Associated Institute for High Temperatures, Russian Academy of Sciences, Moscow, 127412 Russia*

Received July 24, 2003

A thermodynamic approach to the sputtering of materials by slow multicharged ions is developed based on the cavitation mechanism of fracture of the surface layer of a target. It is shown that a strong electric field of a slow multicharge ion approaching the surface of a dielectric target leads to the formation of an extended metastable subsurface region. Cavities spontaneously appearing in this region form a percolation cluster leading to the fracture (cavitational electroexplosive erosion) of the target material. Universal relationships established between the volume of the region of fracture, on the one hand, and the ion charge and the target surface properties, on the other hand, qualitatively agree with experimental data on the sputtering of LiF and SiO_2 by slow argon and xenon ions. *© 2003 MAIK "Nauka/Interperiodica".*

PACS numbers: 79.20.Rf, 81.15.Cd

Sputtering of the surface of metals and dielectrics plays an important role in the interaction of plasma with such solids. In particular, this is an important factor involved in the interaction of plasma with walls and divertor plates in setups with magnetic confinement. A traditional approach to the description of sputtering is based on an analysis of the kinetics of interactions between impinging ions and surface atoms leading to escape of the latter from the target material exposed to the beam of projectiles. In recent years, much attention has been devoted to an analysis of the action of relatively slow multicharge ions on the solid surface.

In the last decade, experiments with the beams of slow multicharge ions acting upon the surface of some dielectrics revealed a sharp increase in the amount of sputtered material with increasing ion charge Z [1–3]. Figure 1 shows plots of the total yield of sputtered atoms versus Z for polycrystalline LiF and SiO_2 targets under the action of slow Ar^{q+} and Xe^{q+} ions. These curves were constructed by extrapolating the data of [1–3] to the region of ultimately low kinetic energies of ions. As can be seen, the number of sputtered particles weakly depends on the ion mass and increases with the ion charge as Z^2. The surface of LiF is sputtered more effectively than that of SiO_2. The number of sputtered atoms per incident ion reaches up to about one hundred for sufficiently high ion charges. This result indicates that the potential energy stored in the form of a high ionization potential of the multicharge ion is quite effectively distributed between many atoms of the target, so that the region of fracture has macroscopic dimensions. This circumstance suggests that the phenomenon under consideration can be described using a thermodynamic approach.

The aforementioned experimental results were interpreted in [1–3] using the models of "Coulomb explosion" [4] and defect mediated sputtering [1]. Both models are formulated in terms of ion recharge, Auger effect, and other processes taking place at sufficiently small distances from the sample surface that are more applicable in the case of fast incident ions. However,

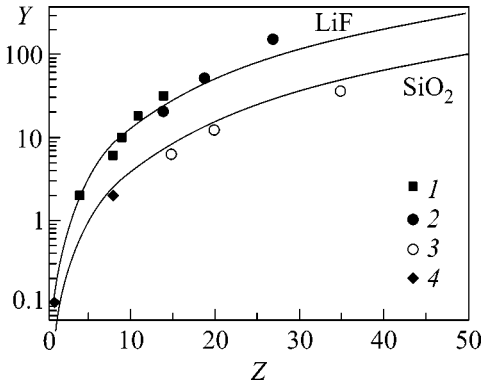

Fig. 1. Plots of the number of sputtered atoms for LiF and SiO_2 targets versus ion charge. Symbols represent the experimental data [1–3] extrapolated to small kinetic energies for (*1*, *4*) Ar^{q+} and (*2*, *3*) Xe^{q+} ions. Solid curves show the results of calculations according to the proposed model.

0021-3640/03/7805-0291$24.00 © 2003 MAIK "Nauka/Interperiodica"

slow multicharge ions begin to act upon the target surface already at large (on the scale of models [1–3]) distances, creating regions of tensile stressed state in a surface layer of the material. Provided a sufficiently high strength of the electric field, this stress can produce local fracture of the surface layer by mechanism of cavitational electroerosion.

Below we will estimate the sputtering yields within the framework of a thermofluctuational mechanism of cavity formation in the surface layer of a target. According to this model, the physical pattern of sputtering consists in an extended subsurface region of the material passing into a metastable state under the action of a strong electric field of a multicharge ion approaching the target. Thermal fluctuations lead to the appearance of critical cavities, which form a percolation cluster leading eventually to the material fracture within a certain volume of the surface layer. The probability of critical cavity formation can be determined by the general expressions for the fluctuations of physical quantities, including the efficiency of the ion action upon the surface as a function of the ion charge and the material temperature. Estimates of the volume of the region of fracture and the time required for the cavity formation in the above pattern are consistent with the known experimental data [1–3].

The time of interaction of a multicharge ion with the target surface is sufficiently short, which leads to certain features previously observed in investigations of the shock wave fracture [5, 6]. In particular, the results of investigations of the breakage of a rear surface of Al and Cu foils under the action of nanosecond high-power laser radiation pulses showed that, for these very short times of action, the buildup of tensile stresses at the rear surface of the target is so rapid that the cleavage is determined by the appearance and coalescence of newly formed cavities, rather than by the growth and merge of the flaws initially existing in the material. Such cavities appear in a tensile stressed metastable solid as a result of thermal fluctuations, by analogy with the cavities formed in a liquid during cavitation. The merge of cavities leads to the formation of a cleavage surface and, eventually, to the fracture of a certain region of the surface layer. An analogous cavitation mechanism was proposed for the explosion of microscopic cusps on a cathode surface under the action of a strong electric field (explosion-like emission) [7].

A multicharge ion approaching the target surface also induces the formation of an extended metastable subsurface region where similar effects can take place. The general and simple thermodynamic approach developed below allows certain laws of the sputtering process under these conditions to be established.

Consider a slowly moving ion possessing a mass M and bearing a charge Z, occurring at a distance x from the surface of a dielectric target (to the first approximation, the surface is assumed to be flat). In the general case, the ion charge exhibits a change near the surface as a result of recharge and, hence, depends on the distance to the surface. Calculations show that this change is rather significant for metals and much less pronounced for dielectrics. In the case of LiF and SiO_2 targets, the charge variations at a distance significant from the standpoint of sputtering are close to unity for the ion charges exceeding ten. Therefore, these changes can be ignored. As for metals, the estimates obtained below can be extended to such targets by substituting data on the dependence of charge on the distance [3] into the formulas presented below.

According to [8, 9], the permittivity of LiF is $\varepsilon = 9$ and that of SiO_2 varies within 3.8–5.4. Let the ion to possess an initial kinetic energy of K be determined by the ion source. Beginning with a certain distance, the kinetic energy K will be small as compared to a potential energy determined by the interaction between the ion and the image. As can be readily shown, this takes place at a distance x_0 meeting the condition

$$x_0 \le 2(eZ)^2/K(1+\varepsilon). \quad (1)$$

If the initial kinetic energy of an ion is large, the x_0 value is so small that the potential energy of this ion is insignificant. On the contrary, when K is small, the ion motion beginning with distances on the order of x_0 acquires a potential character. For an ion with $Z = 10$ and a kinetic energy of ~10 eV, this distance from a LiF surface is $x_0 \le 2 \times 10^{-7}$ cm.

The image force acting upon an ion occurring at a distance x from a flat surface is

$$F = \frac{(eZ)^2(1-\varepsilon)}{4x^2(1+\varepsilon)}. \quad (2)$$

The ion, acquiring an instantaneous velocity of

$$V(x) = \sqrt{\frac{(eZ)^2(\varepsilon-1)}{2Mx(1+\varepsilon)}}, \quad (3)$$

travels the distance x for a time of

$$t(x) = \frac{2x^{3/2}}{3eZ}\sqrt{2M\frac{\varepsilon+1}{\varepsilon-1}}. \quad (4)$$

For the numerical estimates, this formula is conveniently rewritten as $t = 5.7 \times 10^{-14}\sqrt{\mu x^3/Z^2}$, where μ is the molecular weight and all distances are expressed in units of 10^{-7} cm. For an argon ion with $Z = 10$ and $\mu \approx 40$ at $x_0 = 10^{-6}$ cm, we obtain $t \sim 10^{-12}$ s.

As is known, the strength characteristics (in particular, the cleavage stress) of solids significantly increase even in a nanosecond range of the interaction times [5, 6]. In the case under consideration, these times are much shorter. This gives ground to suggest that the elastic limit (for LiF, $p_e = 112$ bar [8]) for such short interaction times also exhibits a considerable increase. This implies that the surface layer of a solid cannot turn

to a yield state and occurs during this interaction in an extended metastable state.

Now it will be demonstrated that, even within short times under consideration, the electrostatic equilibrium is established in the dielectric and the electric field penetrates into the material to a sufficiently large depth. A characteristic time of the charge relaxation is $\tau_Q = \varepsilon/4\pi\zeta$, where ζ is the electric conductivity. For metals, this time is rather short ($\sim 10^{-18}$ s [10]). The thermal conductivity of LiF is about 4 W/mK [9]. Estimating the corresponding electric conductivity by the Wiedemann–Franz formula, we obtain $\tau_Q \sim 10^{-16}$ s. At the same time, the conductivity of NaCl (a substance possessing otherwise close properties) is $\sim 10^{-9}$ Ω^{-1} cm^{-1} [9], which yields a consistently close estimate of $\tau_Q \leq 10^{-16}$ s.

The field penetration depth can be estimated as $\delta \sim c_0\sqrt{t/\zeta}$, where c_0 is the velocity of light. Substituting $t \sim 10^{-12}$ s and $\zeta \sim 10^{16}$ s^{-1}, we obtain $\delta \sim 3 \times 10^{-4}$ cm. This value is significantly greater than the characteristic distances at which the ion motion acquires a potential character. Therefore, the distribution of the electric field is the same as in the stationary case.

In the electrostatic equilibrium, the force acting upon a dielectric surface is directed toward a medium possessing lower permittivity. At a point of the flat surface occurring at a distance of $r = (x^2 + y^2)^{0.5}$ from the ion, this force produces a tensile stress (negative pressure) [11]

$$\Delta p(x, z) = \frac{(eZ)^2}{2\pi x^4}\frac{1-\varepsilon}{(1+\varepsilon)^2}\frac{(\varepsilon + z^2)}{(1+z^2)^3}, \quad (5)$$

where $z = y/x$ and y is the coordinate measured along the surface from the ion projection point. For the sake of simplicity, let us replace the nonuniformly distributed pressure by the effective uniform pressure acting upon a certain effective area determined from the relation

$$2\pi\int_0^\infty \Delta p(x, z) z dz = \Delta p(x, 0)\pi z_e^2. \quad (6)$$

For $\varepsilon \gg 1$, this yields $z_e = x/\sqrt{2}$ and the effective area is $\pi x^2/2$.

Experiencing a negative pressure, a certain subsurface layer of the dielectric occurs in an extended metastable state. At a certain electric field strength and the depth of penetration into the metastable region (and the corresponding tensile stresses), cavities of a critical size can form in this region. In other words, cavitation can take place in a small region of the dielectric subjected to a strong action of the field of a multicharge ion approaching the target.

The size of a critical cavity and the work required for its formation are determined by the formulas

$$a_c = \frac{2\sigma}{\Delta p}, \quad A_c = \frac{16\pi\sigma^3}{3(\Delta p)^2}, \quad (7)$$

where σ is the surface tension of the target material. Substituting the expression for Δp (5) with $y = 0$ into formulas (7), we obtain

$$a_c = \frac{4\pi\sigma x^4}{(eZ)^2 f(\varepsilon)}; \quad A_c = \frac{64\pi^3\sigma^3 x^8}{3(eZ)^4 f(\varepsilon)^2}, \quad (8)$$

where $f(\varepsilon) = (\varepsilon - 1)\varepsilon/(1 + \varepsilon)^2$ is a parameter depending on the material properties.

It should be noted that particular values of the permittivity in formulas (8) may differ from the above static estimates. In the case of alternating electric fields, including the fields generated by moving ions, the permittivity can vary from the static value up to a limit determined by the optical properties of the medium. In practice, the permittivity is assigned a certain frequency-averaged value lying between the aforementioned limits. Taking into account that the thermodynamic characteristics are rather rapidly varying functions, the particular choice of permittivity rather weakly influences the results. For this reason, the simple estimates below are obtained for the static values of the permittivity.

The fracture of a material usually depends on the rate of growth of the existing and newly formed cavities in the extended material, as determined by the diffusion of dislocations. In the case under consideration, the characteristic times of such growth are significantly greater as compared to the time of the ion–surface interaction. Therefore, the surface layer fracture is determined by breakage of the solid phase connectivity in the subsurface layer upon reaching the percolation threshold for the newly formed critical cavities, rather than by the merge of growing cavities: the fracture has an explosion character [12].

The explosion takes place when the expanded region volume per cavity reaches a level of

$$W^* = 4\pi a_c^3/3(1-\beta), \quad (9)$$

where β is the percolation threshold ($\beta \sim 0.2$ for a crystal with the simple cubic lattice). Assuming that, during the ion–surface interaction time, the negative pressure wave propagates to a depth on the order of $2a_c \sim ct$, where c is the velocity of sound (the validity of this assumption will be assessed below), we obtain an estimate for the volume of the fractured region: $W \sim \pi x^2 a_c$. The ratio W/W^* gives the number of critical cavities necessary for the fracture. This ratio strongly varies with x: $W/W^* \sim 1/x^4$. For this reason, the values of x corresponding to the appearance of a single critical cavity are virtually the same as those providing for the fracture of a subsurface region. Substituting expression (7) for

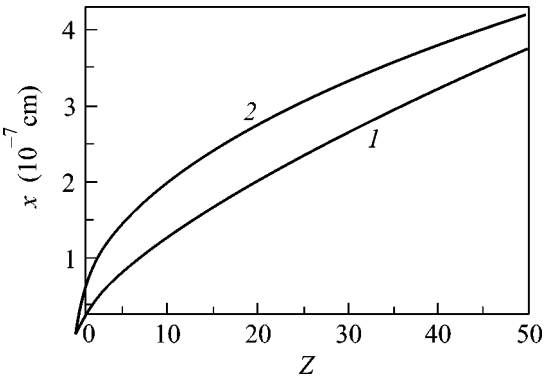

Fig. 2. Plots of the characteristic distances for (*1*) microvolume fracture and (*2*) critical cavity formation versus ion charge for argon ions interacting with a LiF surface.

a_c into formula (9) and equating this to $2\pi x^2 a_c$, we determine a characteristic distance x_c from the ion to the surface at which the cavitational fracture of the surface region will take place:

$$x_c = \left(\frac{3(1-\beta)}{2}\right)^{1/6}\left[\frac{(eZ)^2 f}{4\pi\sigma}\right]^{1/3}. \quad (10)$$

The volume of the fractured material is

$$W = 3(1-\beta)\frac{(eZ)^2 f}{4\sigma}. \quad (11)$$

Formula (11), multiplied by the number density of atoms, determines the number of sputtered atoms. This number depends only on the ion charge eZ and the prosperities of a target material (ε, σ). According to formula (11) the volume of sputtered material is a function of the combination of these quantities. Including the ion mass M, we can find the combinations of parameters corresponding to the energy of formation of a critical cavity, the ion velocity, and the interaction time. These combinations (to within the numerical factors and the functions of ε that are on the order of unity) are, respectively, as follows:

$$A_c \sim (eZ)^{4/3}\sigma^{1/3},$$
$$V_c \sim \sqrt{\frac{(eZ)^{4/3}\sigma^{1/3}}{M}}, \quad t_c \sim \sqrt{\frac{M}{\sigma}}. \quad (12)$$

An important condition for realization of the cavitational fracture is that the volume W must occur within the expanded metastable subsurface region. To provide for this, a perturbation produced by the tensile stress on the surface has to penetrate inside the material to a depth of $\sim 2a_c$ during the interaction time. This implies the condition $V \le c$, where c is the sound velocity in the dielectric (for LiF, $c \sim 5 \times 10^5$ cm/s [9]). Under the experimental conditions [1–3], the maximum velocity for argon ions with a maximum charge of $Z = 14$ and for xenon ions with $Z = 37$ was $V \sim 8 \times 10^5$ cm/s, which is close to the velocity of sound. For lower values of the ion charge, the velocity according to formula (12) decreases. Thus, we may conclude that, in the experiments described in [1–3], the condition $V \le c$ was satisfied (in the order of magnitude).

The second, but not less important condition is that a cavity of the critical size has to be formed in the volume W^* during the ion–surface interaction time t. A necessary condition for this is that

$$tW^*J = 1, \quad (13)$$

where J is the cavity nucleation rate. The latter quantity can be written for a nondissipative system as [12]

$$J = \frac{kT}{h}\frac{3}{4\pi a_c^2}\exp\left(-\frac{A_c}{kT}\right), \quad (14)$$

where h is the Planck constant and T is the absolute temperature. Substituting t and a_c according to Eqs. (4) and (8) into formulas (13) and (14), we arrive at an equation determining the values of x for which the formation of a critical cavity is possible. Figure 2 shows the solutions x (curve *2*) of this equation as a function of Z for argon ions and a LiF surface. In the same figure, curve *1* shows the values of x_c determining the region of fracture according to formula (10). As can be seen, curves *1* and *2* are situated close to each other, which implies that a critical cavity will form by the moment when the ion will approach the surface to a distance of x_c. This situation also takes place for the other combinations of ions and target materials.

Figure 1 (solid curves) shows the plots of fracture volumes (or the numbers of sputtered atoms) versus Z for LiF and SiO_2. For this calculation, the values of the surface tension of LiF and SiO_2 were taken to be equal to $\sigma \approx 250$ and 500 erg/cm^2, respectively [10]. In accordance with formula (11), the character of sputtering is determined by the properties of a target material and the ion charge, while being independent of the ion mass. In our model calculations, the volume of fracture was determined to within a constant factor. In order to provide for a better agreement with the experiment, we introduced a fitting parameter on the order of unity into formula (11), which was the same for both materials. It is interesting to note that the value of this parameter for the best fit to experiment was on the order of unity (~1.4) even for the static values of permittivity used in formula (11). As can be seen, this provides for a good agreement with the experimental data for both LiF and SiO_2.

This study was supported by the Russian Foundation for Basic Research, project nos. 99-02-16596, 99-02-16619, NSh-1953.2003.2, and NSh-2024.2003.2 and MNTTs-2155.

REFERENCES

1. T. Neidhart, F. Pichler, F. Aumayr, *et al.*, Phys. Rev. Lett. **74**, 5280 (1995).
2. M. Sporn, G. Libiseller, M. Schmid, *et al.*, Phys. Rev. Lett. **79**, 945 (1997).
3. H. P. Winter and F. Aumayr, J. Phys. B: At. Mol. Opt. Phys. **32**, R39 (1999).
4. I. S. Bitensky, M. N. Murakhmetov, and E. S. Parilis, Zh. Tekh. Fiz. **49**, 1044 (1979) [Sov. Phys. Tech. Phys. **24**, 618 (1979)].
5. E. Dekel, F. Eliezer, Z. Henis, *et al.*, J. Appl. Phys. **84**, 4851 (1998).
6. G. I. Kanel', S. V. Razorenov, A. V. Utkin, and V. E. Fortov, *Impact-Wave Phenomena in Condensed Media* (Yanus-K, Moscow, 1996).
7. V. S. Vorob'ev, S. P. Malyshenko, and S. I. Tkachenko, Pis'ma Zh. Éksp. Teor. Fiz. **76**, 503 (2002) [JETP Lett. **76**, 428 (2002)].
8. http://www.almazoptics.com/homepage/LiF.htm.
9. S. I. Popel', *Surface Phenomena in Melts* (Metallurgiya, Moscow, 1994).
10. L. D. Landau and E. M. Lifshitz, *Course of Theoretical Physics*, Vol. 8: *Electrodynamics of Continuous Media*, 3rd ed. (Nauka, Moscow, 1992; Pergamon, New York, 1984).
11. M. Pettersen, S. Balibar, and H. J. Maris, Phys. Rev. B **49**, 12062 (1994).
12. T. L. Chelidze, *The Passing Theory Methods in Mechanics of Geomaterials* (Nauka, Moscow, 1987).

Translated by P. Pozdeev

JETP Letters, Vol. 78, No. 5, 2003, pp. 296–299. Translated from Pis'ma v Zhurnal Éksperimental'noĭ i Teoreticheskoĭ Fiziki, Vol. 78, No. 5, 2003, pp. 742–746.

Splitting of Thin Current Sheets in the Earth's Magnetosphere

L. M. Zelenyĭ[1], H. V. Malova[1, 2], and V. Yu. Popov[3]

[1] *Space Research Institute, Russian Academy of Sciences, ul. Profsoyuznaya 84/32, Moscow, 117997 Russia*
e-mail: lzelenyi@iki.rssi.ru

[2] *Institute of Nuclear Physics, Moscow State University, Vorob'evy gory, Moscow, 119992 Russia*

[3] *Faculty of Physics, Moscow State University, Vorob'evy gory, Moscow, 119992 Russia*

Received June 10, 2003; in final form, July 28, 2003

An analytic model of a one-dimensional self-consistent anisotropic thin current sheet is proposed. This model describes the sheet with a split (or bifurcated) structure, where the current density is minimal at the center and maximal at the edges. The model is specified by the set of Vlasov–Maxwell equations that reduces to the Grad–Shafranov equation. Under the assumption that particles move quasi-adiabatically, i.e., that the approximate integral of motion I_z is conserved, the slow evolution of the system in the course of diffusion of the distribution function in I_z is analyzed. Scattering processes can give rise to the partial capture of flying ions near the current sheet. Since the current of such quasi-trapped particles is directed oppositely to the current of flying particles, the local current at the center of the sheet is fully or partially compensated. As a result, the ordinary single-peak shape of the current density profile changes to the bifurcated shape. Such a structure is characteristic of the thin current sheet before the total destruction, when the tension of the magnetic field is unbalanced. Numerical calculations are corroborated by the observations of split current sheets in the magnetotail by the Cluster and Geotail satellites. The obtained results indicate that a possible mechanism of the destruction of the thin current sheet is not necessarily associated with the development of plasma instabilities but can be evolutionary. © *2003 MAIK "Nauka/Interperiodica".*

PACS numbers: 94.30.Fk

Very thin current sheets with a thickness in the area of the ion gyroradius are quite often observed by satellites in a hot collisionless plasma in the Earth's magnetosphere [1–3]. In terms of the MHD theory, they are discontinuities serving as energy "reservoirs" for the transformation of the electromagnetic energy of solar wind to the kinetic energy of plasma fluxes. It is interesting that, as early as the 1970s, Syrovatskiĭ [4, 5] predicted the formation of such singular structures for certain plasma motions.

Satellite observations show that thin current sheets have a number of properties that are different from the properties of ordinary Harris-type sheets [6]. In particular, it was shown that thin current sheets could be embedded into a thicker plasma sheet [3]. Ions are usually primary current carriers in thin current sheets because of a significant temperature difference $T_i/T_e \geq 5$ [7]. Recent measurements by Cluster satellites [8, 9] in the near magnetotail (~15–20 R_E) show that the current density profile during substorms can have a split current structure (Runov *et al.* [8] called it bifurcated structure) such that current is concentrated at the sheet edges, whereas the local dip of the current density is observed at the center.

It is necessary to develop models of the formation and internal structure of split current sheets. Since thin current sheets can accumulate a considerable energy (~10^{14}–10^{15} J), calculations of their evolution regimes are necessary for a deep insight into the global dynamics of the magnetosphere.

In this paper, we present a self-consistent one-dimensional model of an anisotropic thin current sheet. In this model, the development of the split current sheet structure is caused by the evolution of a current density profile as a result of the nonadiabatic scattering of particles in a strongly curved magnetic field of the thin current sheet.

This model of self-consistent anisotropic thin current sheet shows how the sheet evolves naturally from the ordinary Harris-type configuration [6] to the bifurcated configuration. This evolution is caused by the nonadiabatic scattering typical for the interaction of a particle with strong magnetic inhomogeneities. In this case, the maximal Larmor radius ρ_L of ions (basic current carriers) is much larger than the radius of curvature R_c of the magnetic field lines, so that the so-called adiabaticity parameter $\kappa = \sqrt{R_c/\rho_L}$ lies in the range 0.1–0.3. In this regime, called quasi-adiabatic regime [10], the action invariant for fast motion of particles across the sheet is approximately conserved; i.e.,

$$I_z = \frac{1}{2\pi}\oint m v_z dz \approx \text{const}. \quad (1)$$

However, when the particle crosses the plane of the thin current sheet, ΔI_z jumps depend only linearly on the

small parameter κ; i.e., $\Delta I_z/I_z \sim \kappa$ [10]. For this reason, this regime is called quasi-adiabatic. Figure 1 shows the characteristic ion orbits in the projection onto the current sheet.

The basic current forming the sheet is supported by flying particles on the open, so-called Speiser, orbits [11] (Fig. 1a) characterized by small I_z values. Orbits with large I_z are closed and called "cucumber" orbits due to their oval shape [10]. Jumps in the I_z invariant lead to the transition of particles from open trajectories to closed ones and vise versa (see Fig. 1b). As will be shown below, this process is quite slow, as compared to the characteristic time of motion of particles through the sheet, and can be described by the diffusion equation (see below). Since the diffusion process is slow, one can assume that the sheet is in a quasi-equilibrium state at each stage of the process. Therefore, the evolution of the sheet can be considered as a sequence of quasi-static equilibria.

Figure 2 shows the scheme of the proposed model. Impinging anisotropic ion fluxes arrive at the sheet from the distant plasma sources located on both sides of the sheet. The ratio $\varepsilon = v_T/v_D$ of the thermal velocity v_T of these fluxes to their average flux velocity v_D is an important anisotropy parameter. Near the neutral plane, ions are "demagnetized" and move along the nonlinear loop orbits near the XY plane in the thin current sheet (Fig. 3). Some flying particles drift from open orbits to quasi-trapped (cucumber) orbits as a result of nonadiabatic scattering (see Figs. 1b, 2).

Under the above assumptions, the set of Vlasov–Maxwell equations $\mathrm{curl}\mathbf{B} = (4\pi/c)\mathbf{J}$, $df/dt = 0$ reduces to the one-dimensional scalar equation

$$dB/dz = (4\pi e/c)\int v_y f(z, \mathbf{v})\, d\mathbf{v} \qquad (2)$$

for the tangential component of the magnetic field. The quasi-adiabatic condition makes it possible to solve the problem with the use of two integrals of motion: total energy $W = mv_0^2/2$ of particles and quasi-adiabatic invariant I_z of the fast z motion. We introduce the dimensionless variables $\zeta = z\varepsilon^{-4/3}\omega_0/v_D$, $\mathbf{w} \equiv \varepsilon^{-2/3}\mathbf{v}/v_D$, $I = \varepsilon^{2/3}I_z\omega_0/mv_T$, $b = B/B_0$, and $\omega_0 = eB_0/mc$. After integration with respect to ζ, Eq. (2) reduces to the Grad–Shafranov-type equation [12]

$$b^2(\eta) = \frac{8\varepsilon^{1/3}}{\pi^{3/2}}\left(\frac{v_D}{v_A}\right)^2 \frac{F_{(+)}(\eta) + F_{(-)}(\eta)}{1 + \mathrm{erf}(\varepsilon^{-1})}, \qquad (3)$$

where $\eta = \varepsilon^{2/3}\int B(\zeta')\, d\zeta'$ is the vector potential, v_A is the Alfvén velocity, and

$$F_{(\pm)}(\eta) = \pm\int_0^\eta d\eta' \int_0^\infty dw_x \int_0^\infty w_y dw_y \int_0^\infty f\, dw_\zeta \qquad (4)$$

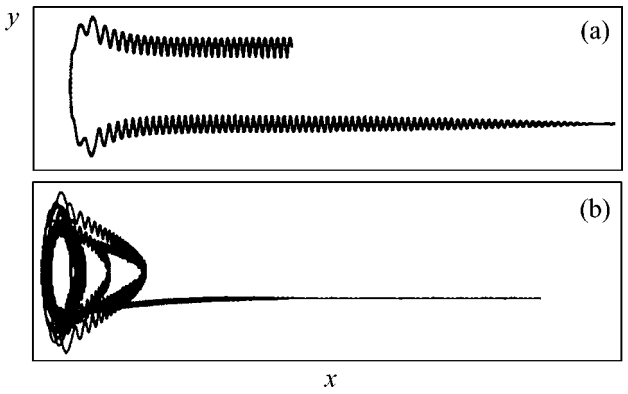

Fig. 1. Two types of quasi-adiabatic trajectories of particles in a curved magnetic field $\mathbf{B} = \{B_x, 0, B_z\}$: (a) characteristic transient (Speiser) orbit and (b) quasi-trapped (cucumber) orbit.

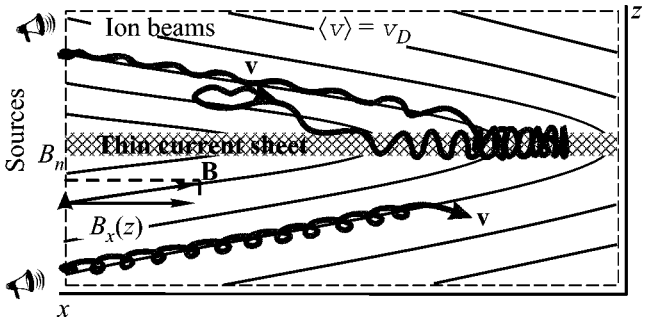

Fig. 2. Model scheme: particles fly from sources, and one particle is trapped by the sheet.

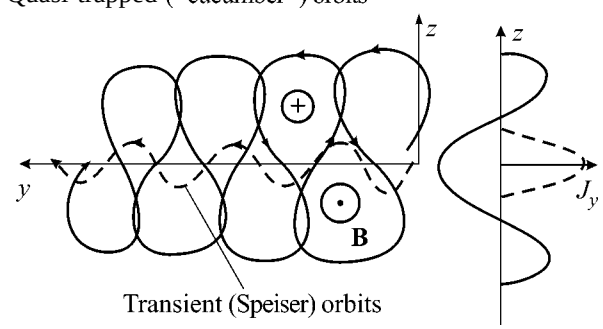

Fig. 3. (Left panel) Solid and dashed lines are elements of a quasi-adiabatic cucumber orbit and Speiser orbit, respectively, at the center of the current sheet; (right panel) the plot of the corresponding local current densities $J_y(z)$.

are the partial densities of positive and negative currents. The detailed derivation of Eq. (3) was given in [13, 14]. The function $f \equiv f(W(w_x, w_y, w_\zeta), I(w_x, w_y, w_\zeta, \eta'))$ describing the ion distribution over the invariants of

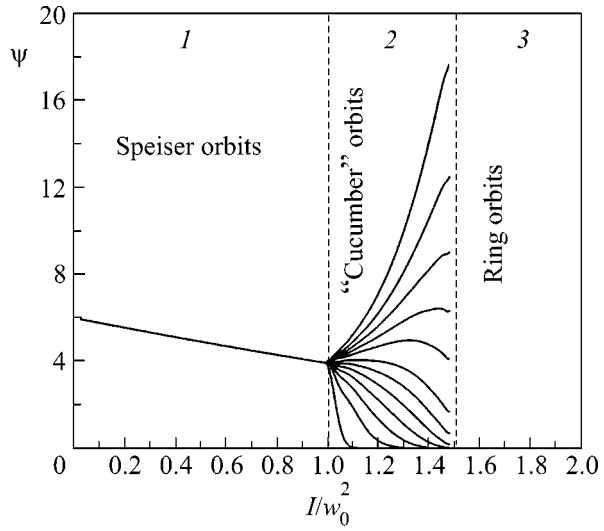

Fig. 4. Profiles of the plasma distribution function ψ in the thin current sheet at different times τ vs. the adiabatic invariant *I*.

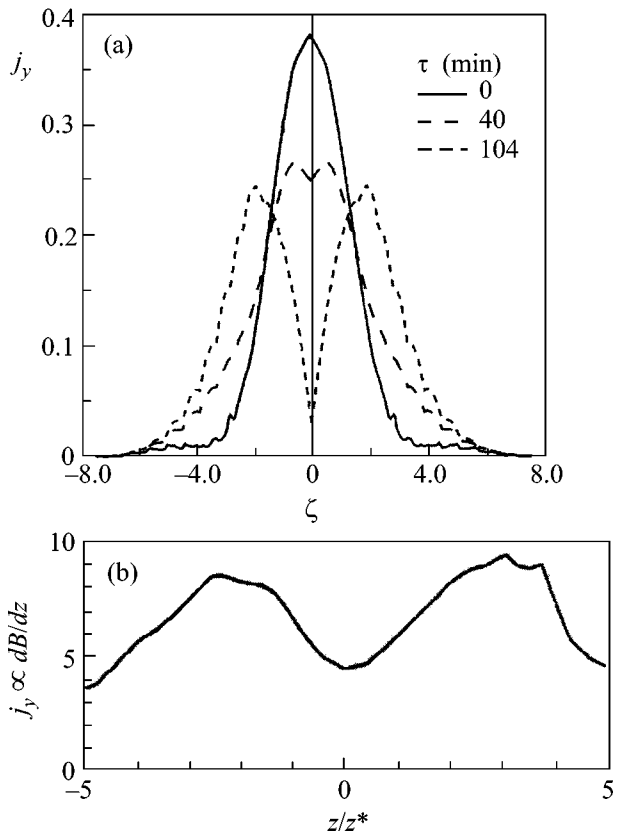

Fig. 5. (a) Profile of the dimensionless current density $j_y = J_y(z)/en_0v_D\varepsilon^{2/3}$ calculated as a function of the dimensionless coordinate ζ for $\tau = \omega_n t$ = (solid line) 0, (long dashes) 40, and (short dashes) 104 min, and (b) the statistically averaged current profile measured in [16].

motion depends implicitly on the velocities of particles and the *z* coordinate. Thus, the distribution function of plasma particles in the thin current sheet can be defined as follows (see Fig. 4). For small invariant values in interval *1* $(0, I_1]$, where $I_1 = w_0^2$, $w_0^2 = w_x^2 + w_y^2 + w_\zeta^2$ [15], current carriers move along Speiser orbits, and the initial distribution function can be specified in the form

$$f = \frac{n_0 \exp\{-\varepsilon^{2/3}[(\sqrt{w_0^2 - I} - \varepsilon^{-2/3})^2 + I]\}}{\pi^{3/2} v_T^2 [1 + \mathrm{erf}(\varepsilon^{-1})]} \quad (5)$$

of the Maxwell distribution shifted by v_D and having thermal spread v_T.

Quasi-trapped particles correspond to interval *2* $(I_1, I_2]$ $(I_2 = \sigma I_1, \sigma = (L/\rho_0)^{1/2} > 1)$. The distribution function $\psi \equiv \psi(I, \tau)$ $(\tau = \omega_n t, \omega_n = eB_n/mc)$ of scattered particles can be determined by solving the diffusion equation

$$\frac{\partial \psi}{\partial \tau} = \frac{\partial}{\partial I} D(I, \tau) \frac{\partial \psi}{\partial I}. \quad (6)$$

Here, the variable coefficient [10]

$$D = \frac{3\pi^2}{16 T_{ab}} \kappa^2 (1 - I^{4/3}), \quad (7)$$

where T_{ab} is the dimensionless period of motion of particles in closed orbits, corresponds to the linear jumps ΔI_z in the small parameter κ. The distribution function of the scattered plasma depends on time. However, the condition of fast relaxation of the system makes it possible to use distribution function profiles at different times as instantaneous quasi-equilibrium configurations. Thus, an "instantaneous pattern" of the distribution function of the quasi-trapped plasma is always used on the right-hand side of Eq. (3). Figure 4 shows profiles of the function ψ for different times τ. It is seen that the initially empty region of quasi-trapped cucumber orbits is gradually filled. Region *3*, where $I > I_2$, corresponds to the trapped plasma on completely integrable orbits. These orbits are ignored in this problem, because they are dynamically inaccessible from regions *1* and *2*; i.e., one can set $f = 0$.

Figure 5a shows the evolution of the current density profile as a result of the accumulation of the quasi-trapped plasma inside the thin current sheet at different times τ. Calculations were performed with the source anisotropy parameter $\varepsilon = 1$, which is in a good agreement with the actual ε value for the magnetotail plasma. These results are compared with the measurements in the magnetotail that are averaged over a large data sample [16].

Since the thin current sheet contains the trapped population during the main period of its life, the $J_y(z)$ profile must have a "statistical dip" at the center of the sheet. The theoretical and experimental results are in good qualitative agreement with each other (Fig. 5).

Although there is back diffusion from region *2* to region *1*, the accumulation of the quasi-trapped population in the thin current sheet continues up to the complete splitting of the sheet ($J_y|_{z=0} = 0$). In this case, the equilibrium self-consistent solutions are absent in the model. We treat this fact as the loss of equilibrium of the real thin current sheet with its further decomposition that occurs immediately after $\tau^* = 104$ min. The characteristic regular time t^* of such a destruction under the magnetotail conditions ($B_n \sim 0.5$–1.5 nT) can be estimated at 30–90 min in agreement with the characteristic time of the so-called phase of energy accumulation (growth phase) in the magnetotail.

The model results both agree well with the Geotail measurements [16] in the magnetotail at a distance of about 100 R_E (which is traditionally considered as the site of localization of the distant neutral line) and with certain measurements of split sheets in the near magnetotail [8, 9]. The model describes the natural internal evolution of the current sheet until its destruction without inclusion of various current instabilities. The problem of instabilities in the thin current sheet has not yet been solved. All models, both analytic and numerical, indicate that one instability (e.g., tearing, kink, or bottle) cannot be responsible for the sheet destruction [17–19]. However, to understand the adequacy of the proposed model for the description of the processes responsible for the formation of split sheets, additional magnetospheric experiments are necessary.

The model can explain the characteristic properties of the thin current sheet such as small thickness ($L \sim \rho_L$), "overshoot" in the magnetic field structure, characteristic anisotropic pressure tensor, dominance of ions in the current, and some specific forms of the plasma velocity distribution functions $f(v_x, v_y, v_z)$ [15] inside the thin current sheet. These distribution functions describe how the quasi-trapped plasma fills with time a certain phase-space region adjoining the phase-space region of flying particles.

We are grateful to Victor Sergeev (Institute of Physics, St. Petersburg State University, Russia) and Andreĭ Runov (Institut für Weltraumforschung der OAW, Graz, Austria) for stimulating discussions. This work was supported by the Russian Foundation for Basic Research (project nos. 02-02-16003-a, 01-02-16367, and NCNI 00-02-22001) and the Council of the President of the Russian Federation for Support of Leading Scientific Schools (project no. HIII-1739.2003.2).

REFERENCES

1. D. H. Fairfield, in *Magnetic Reconnection in Space and Laboratory Plasmas*, Ed. by E. W. Hones (Am. Geophys. Union, Washington, D.C., 1984), Geophys. Monogr. Ser., Vol. 30, p. 168.
2. T. I. Pulkkinen, D. N. Baker, D. G. Mitchell, *et al.*, J. Geophys. Res. **99** (A4), 5793 (1994).
3. V. A. Sergeev, D. G. Mitchell, C. T. Russell, and D. J. Williams, J. Geophys. Res. **98**, 17345 (1993).
4. S. I. Syrovatskiĭ, Zh. Éksp. Teor. Fiz. **60**, 1727 (1971) [Sov. Phys. JETP **33**, 933 (1971)].
5. S. I. Syrovatskiĭ, in *Proceedings of Lebedev Physical Institute, USSR Academy of Sciences* (Nauka, Moscow, 1974), p. 3.
6. E. G. Harris, Nuovo Cimento **23**, 115 (1962).
7. D. G. Mitchell, G. J. Williams, C. Y. Huang, *et al.*, Geophys. Res. Lett. **17**, 583 (1990).
8. A. Runov, R. Nakamura, W. Baumjohann, *et al.*, Geophys. Res. Lett. **30**, 8 (2003).
9. V. A. Sergeev, A. Runov, W. Baumjohann, *et al.*, Geophys. Res. Lett. **30**, 60 (2003).
10. J. Büchner and L. M. Zelenyi, J. Geophys. Res. **94**, 11821 (1989).
11. T. V. Speiser, J. Geophys. Res. **70**, 4219 (1965).
12. V. D. Shafranov, in *Problems in the Plasma Theory* (Nauka, Moscow, 1963), p. 92.
13. M. I. Sitnov, L. M. Zelenyi, H. V. Malova, and A. S. Sharma, J. Geophys. Res. **105**, 13029 (2000).
14. L. M. Zelenyi, M. I. Sitnov, H. V. Malova, and A. S. Sharma, Nonlinear Processes Geophys. **7**, 127 (2000).
15. L. M. Zelenyi, H. V. Malova, V. Yu. Popov, *et al.*, Adv. Space Res. (in press).
16. M. Hoshino, A. Nishida, T. Mukai, *et al.*, J. Geophys. Res. **101**, 24775 (1996).
17. J. Buchner and J.-P. Kuska, Ann. Geophys. (France) **17**, 604 (1999).
18. F. V. Coroniti, J. Geophys. Res. **85**, 6719 (1980).
19. W. Daughton, J. Geophys. Res. **103**, 29429 (1998).

Translated by R. Tyapaev

JETP Letters, Vol. 78, No. 5, 2003, pp. 300–304. Translated from Pis'ma v Zhurnal Éksperimental'noĭ i Teoreticheskoĭ Fiziki, Vol. 78, No. 5, 2003, pp. 747–752.

The Role of Negative Ions in Experiments with Complex Plasma

B. A. Klumov*, A. V. Ivlev, and G. Morfill

Centre for Interdisciplinary Plasma Science, Max-Planck-Institut für Extraterrestrische Physik, D-85740 Garching, Germany

**e-mail: klumov@cips.mpg.de*

Received July 31, 2003

The influence of negative ions on the state of an rf gas-discharge dusty (complex) plasma containing electronegative gaseous impurities was investigated. A simple one-dimensional argon-discharge model allowing for the impurity-induced plasmachemical reactions was taken as an example to show that the addition of even a minor amount of molecular oxygen changes appreciably the plasma composition and plasma transport properties, as well as the microparticle charges. In turn, these changes have a strong effect on the microparticle force balance and on the formation of various dusty structures in the discharge. © *2003 MAIK "Nauka/Interperiodica".*

PACS numbers: 52.27.Lw; 52.80.-s

In recent years, the processes occurring in weakly ionized plasmas containing microparticles (so-called "dusty particles") have been intensively studied. Such media are customarily referred to as dusty or complex plasmas [1–7]. Plasma recombination at the surface of dusty particles results in their fast charging. As a rule, a microparticle charge is negative[1] and is on the order of 10^3–10^4 electron charges. The presence of charged microparticles renders plasma behavior much more complicated, because new spatial and time scales appear, leading, in particular, to new types of waves and instabilities [8]. The dusty component of a complex plasma can occur in various phase states, from gaseous to crystalline [1–3].[2] The observation of the behavior of individual microparticles allows their behavior to be described at the kinetic level. This property is exceedingly important in the detailed study of the processes occurring in the phase transformations in complex plasmas, in the initiation of hydrodynamic instabilities, etc. The understanding of these processes at the kinetic level can be helpful in the construction of the general theory of phase transitions and can clarify many questions associated with the turbulence initiation.

A low-pressure rf inert-gas (as a rule, argon and, more rarely, helium, neon, and krypton are used) discharge, into which microparticles with the diameter $2a \simeq 1$–10 μm are injected, is traditional in studying the properties of a laboratory complex plasma. The concentration of dusty particles in the discharge is ordinarily varied within $n_d \sim 10^3$–10^6 cm^{-3}. In this work, we consider the argon discharge. The typical parameters of this discharge are as follows: the interelectrode distance is $L \simeq 3$–5 cm, the concentration of neutral atoms (argon) is $n_n \sim 10^{15}$–10^{16} cm^{-3}, the electron and ion concentrations (in the absence of microparticles) are $n_e \simeq n_i \sim 10^8$–10^{10} cm^{-3}, and the electron temperature is $T_e \simeq 1$–3 eV. The ion temperature is close to the temperature of neutrals: $T_i \simeq T_n \approx 300$ K. Note that plasma is weakly ionized with a very low degree of ionization, $n_e/n_n \simeq 10^{-6}$–10^{-7}.

A dusty particle in plasma rapidly acquires negative charge Z_d, which can be estimated by equating the electron and ion flows onto a microparticle. To determine these flows, one ordinarily uses the probe approximation of the orbital motion limited (OML) theory (see, e.g., [4]), in which the cross-sections for electron and ion interactions with an isolated charged microparticle are determined from the energy and momentum conservation laws. According to the OML theory, the charge increases proportionally to the microparticle size and electron temperature: $Z_d \propto aT_e$. For example, for a particle with a radius of 1 μm in an argon-discharge plasma with the above-mentioned parameters one has $Z_d \sim 3 \times 10^3 e$ (see, e.g., [9]).

Due to the fast electron diffusion onto the walls of a discharge chamber, the central zone of the discharge is charged positively and represents a potential well for the negatively charged microparticles. Under these conditions, the formation of dusty structures is governed by the balance of forces acting on the microparticles; these are the gravity force F_g, the electrostatic force F_E (directed to the discharge center), the ion-drag force F_{id}[3] associated with the momentum transfer from the

[1] A positive microparticle charge can arise under rather exotic conditions, when the photoelectric effect, thermionic emission, or secondary electron emission play the decisive role in the particle charging. These processes are not considered in this work.

[2] Sometimes, complex plasmas also mean nonideal plasmas with strong Coulomb interaction (strong coupling) between microparticles, where the dusty component is in a liquid or crystalline state.

[3] This force is often called ion-entrainment force. The latter term seems to be not perfectly correct, because this force can be directed opposite to the ion flow [10].

0021-3640/03/7805-0300$24.00

ion flow to the microparticles (this force is directed to the walls of a gas-discharge chamber), the neutral gas friction F_n caused by the interaction of a dusty particle with neutral gas, and the thermophoretic force F_T caused by the inhomogeneous heating of a neutral gas in the discharge (the direction of this force is determined by the temperature gradient of the neutral gas and, in general, can be arbitrary). In the ground-based experiments, the gravity force dominates; it is compensated by the electrostatic force only in the electrode sheath, leading, in particular, to microparticle levitation. Under microgravitation conditions, the ion-drag and electrostatic forces (though much weaker than the gravity force) play the main roles and often have the same order of magnitude. The balance of these forces determines the equilibrium configurations of the dusty component in the space experiments.[4] Although the contribution of the thermophoretic force is, as a rule, insignificant, it can play a key role in certain situations. It is worthwhile to present the power-law dependences of the indicated forces on the microparticle size: $F_g \propto a^3$, $F_{\text{id}} \propto a^2$ (for sufficiently small particles [11]), $F_E \propto a$, and $F_T \propto a^2$.

The addition of an electronegative gas leads to the appearance of negative ions in the discharge. This can strongly affect the plasma parameters and microparticle charges and, hence, the phase state of the dusty component [12].[5] The presence of negative ions also affects the microparticle force balance, which, in turn, can affect the configuration of dusty structures. Therefore, the influence of negative ions on the state of complex plasma can be quite substantial. Nevertheless, these problems have practically not been studied experimentally so far.

In this work, we study a change in the state of complex plasma upon the addition of molecular oxygen O_2 to the rf argon discharge. To begin with, we estimate the influence of molecular oxygen on the plasma composition. For this purpose, we will use the plasmachemical model of discharge in the Ar/O_2 mixture (all plasma parameters are averaged over the discharge volume). For a quasineutral complex plasma, the corresponding set of equations has the form

$$\frac{\partial n_j(t)}{\partial t} = R_j^{\text{prod}} - R_j^{\text{loss}} - R_j^d - n_j/\tau_j, \quad (1)$$

$$\frac{\partial Z_d}{\partial t} = \nu_{i^+} - \nu_{i^-} - \nu_e, \quad (2)$$

$$n_{i^+} = n_e + n_{i^-} + Z_d n_d. \quad (3)$$

Here, n_j stands for the concentrations of electrons and all sorts of ions (positive and negative) in the discharge and also the concentrations of metastable argon and oxygen atoms and molecules which influence the charged component;[6] R_j^{prod} and R_j^{loss} account for the photochemical sources and sinks of the jth component (given, e.g., in [13]); R_j^d describes the jth-component decay at the surface of dusty particles; and $\tau_j \simeq L^2/D_j$ is the characteristic diffusional lifetime of the jth component in the discharge, where D_j is the corresponding diffusion coefficient. Note that the diffusion coefficient strongly depends on the plasma composition; e.g., for the positive ions D_j ranges from the ambipolar (at low concentrations of negative ions) to unipolar (for ion–ion plasma) type. In Eq. (2) for microparticle charging, the terms ν_e, ν_{i^-}, and ν_{i^+} describe, in the OML approximation, the electron, negative-ion, and positive-ion flows onto a microparticle, respectively (see, e.g., [14]):

$$\nu_{e,i^-} \approx -\pi a^2 (8T_{e,i^-}/\pi m_{e,i^-})^{1/2} n_{e,i^-} \exp(e^2 Z_d / a T_{e,i^-}),$$

$$\nu_{i^+} \approx \pi a^2 (8T_{i^+}/\pi m_{i^+})^{1/2} n_{i^+} (1 - e^2 Z_d / a T_{i^+}).$$

Since $T_{i^+} \approx T_{i^-} \ll T_e$, the contribution from the negative ions to the microparticle charging can be ignored (note that $R_j^d = \nu_j n_d$). The set of Eqs. (1)–(3) describes the processes having substantially different characteristic times. Such sets of equations are ordinarily solved by the Gear method [15]. The equilibrium concentrations of the charged component and the charge of a micron-sized particle in the indicated discharge are presented in Fig. 1 as functions of the partial concentration ($[O_2]/[Ar]$) of molecular oxygen in the mixture. One can see that, starting with even negligible concentrations of molecular oxygen ($O_2/Ar \geq 10^{-6}$), the plasma composition changes materially to transform from the electron–ion plasma (e and Ar^+) to the ion–ion plasma, in which O_2^+ and O^- are the major ions while the electronic component is strongly suppressed. Such a drastic transformation of the plasma composition is caused by the fast charge-exchange reaction $Ar^+ + O_2 \longrightarrow Ar + O_2^+$ of argon ions on oxygen molecules (the back reaction is almost fully inhibited at room temperature because of a large difference in the ionization potentials of argon (15.75 eV) and molecular oxygen (12.2 eV)) and by the electron dissociative attachment to the oxygen molecule: $O_2 + e \longrightarrow O^- + O + e$. The latter reaction gives

[4] In the absence of gravitation, it is possible to increase materially the sizes of dusty structures and make them more homogeneous. This stipulates the exceeding importance of space experiments.

[5] Negative ions can appear in the discharge in a natural way, e.g., as a result of the erosion of polymeric microparticles that are often used in laboratory experiments and incorporate electronegative compounds in their composition. The electronegative compounds (such as water vapor, molecular oxygen, and carbon dioxide) can penetrate into the discharge from the ambient air if the air tightness of the gas-discharge chamber is broken.

[6] One can show that only the following metastable argon and oxygen atoms and molecules make a contribution to the photochemical properties of the Ar/O_2 mixture: $Ar(^3P_0)$, $Ar(^3P_2)$, $O_2(a^1\Delta_g)$, and $O(^1D)$.

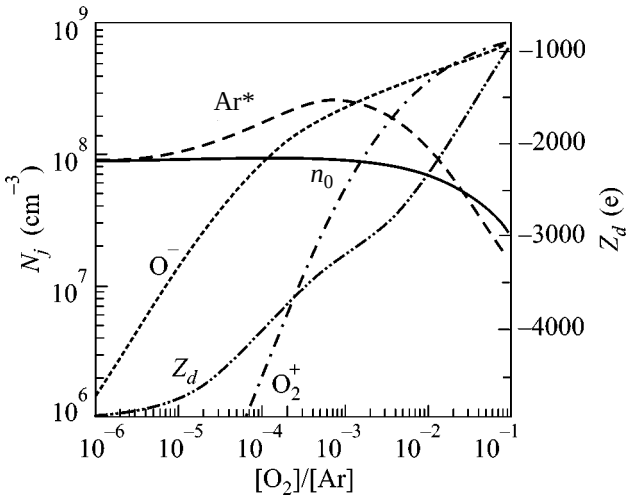

Fig. 1. The composition of an rf discharge plasma in O_2/Ar mixture and the charge Z_d of an individual microparticle as functions of the partial concentration [O_2]/[Ar] of molecular oxygen.

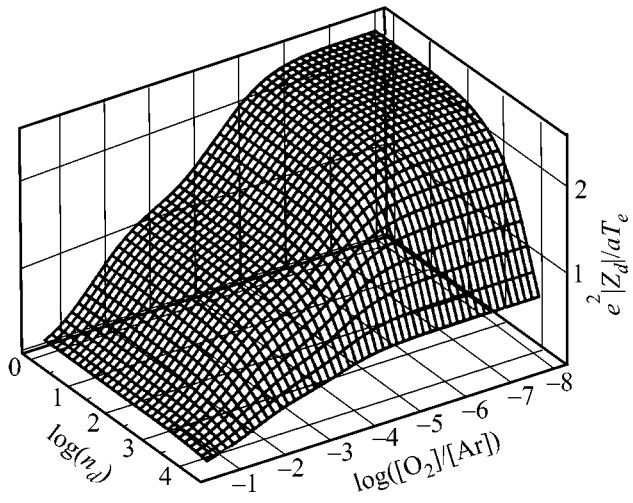

Fig. 2. The charge of a microparticle of size 1 μm in an rf discharge in Ar/O_2 mixture vs. the partial concentration ([O_2]/[Ar]) of molecular oxygen and the microparticle concentration in units of cm^{-3}.

negative ions, which are accumulated in the discharge owing to the above-mentioned electric field configuration. This results in a noticeable decrease in the absolute value of microparticle charge, as compared with plasma in pure argon.

It should be emphasized that such a change in plasma composition can have an appreciable effect on the processes of ion transport in the discharge, because the resonance charge-exchange cross section (scattering of Ar^+ ion by argon atoms) exceeds, by approximately one order of magnitude, the polarization scattering cross section of the O_2^+ ion in argon. This effect can also be of great importance in estimating the momentum transfer from ions to a microparticle for the determination of the ion-drag force. The dimensionless charge (potential) $e^2|Z_d|/aT_e$ of a dusty particle is presented in Fig. 2 as a function of microparticle concentration n_d and partial concentration [O_2]/[Ar] of molecular oxygen. One can see that, for $n_d \sim 10^3$–10^5 cm^{-3}, i.e., for the experimental conditions typical of dusty plasmas, a sizable decrease in the microparticle charge can be caused by the O_2 impurity. Note that the effects considered, likely, show little dependence on the type of electronegative gas M. This is so because the main processes inducing these effects—the formation and accumulation of negative ions in plasma and the fast charge exchange of an argon ions on impurity species ($Ar^+ + M \longrightarrow Ar + M^+$; the back reaction is inhibited because the ionization potential of argon atom is greater than the ionization potential of M)—are efficient for any electronegative gas.

These results qualitatively describe a change in the charge composition of complex plasma in the presence of the O_2 admixture. However, to determine the forces acting on microparticles, it is necessary to know the spatial distribution of complex plasma in the discharge. To this end, we consider a one-dimensional discharge geometry (the coordinate $x = \mp L/2$ corresponds to electrodes, and $x = 0$ corresponds to the discharge center). The ion and electron spatiotemporal distributions can be determined from the set of balance equations after adding to Eq. (1) the term describing the jth-component transport in the diffusional approximation:

$$\frac{\partial n_j(x,t)}{\partial t} + \nabla J_j(x,t) = R_j^{\text{prod}}(x,t) - R_j^{\text{loss}}(x,t) - R_j^d(x,t), \quad (4)$$

$$J_j(x,t) = \mu_j n_j(x,t)E(x,t) - D_j \nabla n_j(x,t), \quad (5)$$

$$\nabla Z_d/\partial t = \nu_p - \nu_n - \nu_e. \quad (6)$$

Here, J_j is the jth charged-component flow, μ_j is the mobility coefficient, and E is the electric field. Inasmuch as the mean free path of ions (both positive and negative) is much smaller than L, the diffusional approximation is quite justified for ions. To determine the electron spatial distribution, the Boltzmann distribution is used, $D_e \nabla n_e(x,t) + \mu_e n_e E(x,t) \approx 0$. For the metastable species, only the diffusional term is taken into account in the transport equation. The boundary conditions for the set of Eqs. (3)–(5) are the following: from the symmetry considerations, $J_j = 0$ and $E = 0$ in the discharge center, and $n_j = 0$ in the electrode sheath.

The ion-concentration, electron-concentration, and electric-field profiles in the discharge are shown in Fig. 3 for various partial concentrations of O_2. As in the case described by the set of Eqs. (1)–(3), the plasma composition strongly changes and the O_2^+ and O^- ions

become dominant. One can see that the presence of negative ions can markedly reduce the electric field. This brings about the breaking of the force balance for a dusty particle. Let us ignore the gravity and thermophoretic forces and consider how the addition of O_2 changes the ratio $\tilde{F} \equiv F_{id}/F_E$ of ion-drag and electrostatic forces, which act in opposite directions and determine the equilibrium configurations of dusty structures. To estimate the ion-drag forces at low ($u \ll v_{T_i}$) ion-drift velocities, we use the expression [11]

$$F_i \approx \frac{4\sqrt{2\pi}}{3}\rho_C n_i m_i v_{T_i} u \Lambda.$$

Here, $\rho_C = Z_d e^2/T_i$ is the Coulomb radius; $\Lambda = \int_0^\infty e^{-x}\ln(1 + 2x/\beta)dx$ is the modified coulombic logarithm ($\beta = \rho_C/\lambda_D$, where λ_D is the Debye ionic radius); and v_{T_i} and u are the ion thermal and drift velocities, respectively. Figure 4 shows the spatial dependence of $\tilde{F}$ for the discharges in pure argon and in argon with an admixture of molecular oxygen ($[O_2]/[Ar]$) = 0.01). The coordinate x_v corresponding to $\tilde{F} = 1$ divides the plasma into two parts: the region $|x| \le x_v$, from which the microparticles are driven out (so-called void),[7] and the region $|x| \ge x_v$ filled with dusty particles. One can see that even a small addition of an electronegative gas to the discharge considerably increases the void size. This is caused by the strong suppression of electrostatic field in the discharge in the presence of negative ions. This result is in excellent agreement with the experimental observations [16].

The thermophoretic force can also make a contribution to the microparticle force balance [17]. One can easily show that the pure argon discharge does not induce any noticeable thermophoretic force, because the temperature inhomogeneity of neutrals is very small for the typical discharge parameters.[8] Indeed, in pure argon, the quenching Ar + Ar* $\longrightarrow$ 2Ar of metastable argon atoms with the rate constant k_q^{Ar} is the main source of heating neutrals. In this case, the neutral gas is heated to $\Delta T_n \simeq k_q^{Ar} n^* \epsilon^* \tau^* \le 0.01$ K, where $\epsilon^* \sim 10$ eV is the energy released in quenching and τ^* is the diffusional lifetime of a metastable atom in the discharge. Due to the resonance character of this reaction, its rate constant is exceedingly small, $k_q^{Ar} \le 10^{-14}$ cm^3 s^{-1}, so that this process cannot lead to a noticeable heating. One can easily show that the charge exchange of the Ar^+ ions accelerated by the near-electrode electric field also makes no contribution to the heating of neutral gas in the discharge. For this reason, the thermophoretic force induced in a pure argon discharge is considerably smaller than the ion-drag and electrostatic forces.

As for the discharge in the Ar/O_2 mixture, the situation with heating the neutral gas becomes cardinally different, because the metastable argon atoms can be efficiently quenched in the reaction O_2 + Ar* $\longrightarrow$ 2O + Ar with rate constant $k_q^{O_2} \sim 10^{-10}$ cm^3 s^{-1}, resulting in

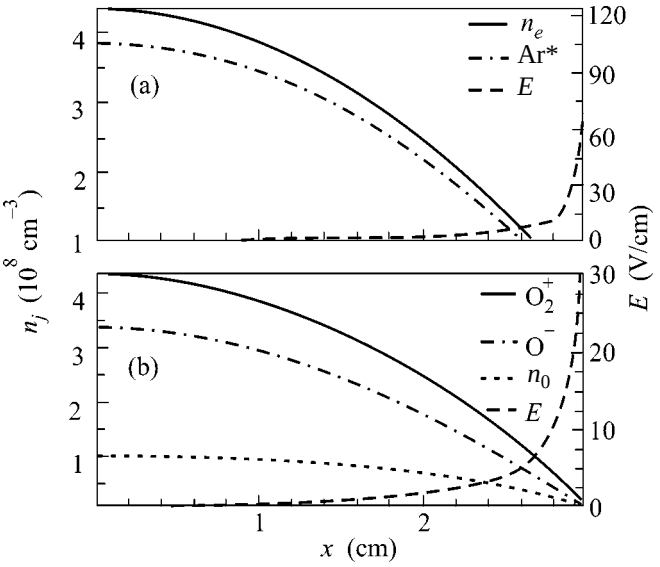

Fig. 3. Spatial dependences of the electric field and the ion and electron densities in an rf discharge in Ar/O_2 mixture. (a) Pure argon discharge and (b) $[O_2]/[Ar] = 0.01$.

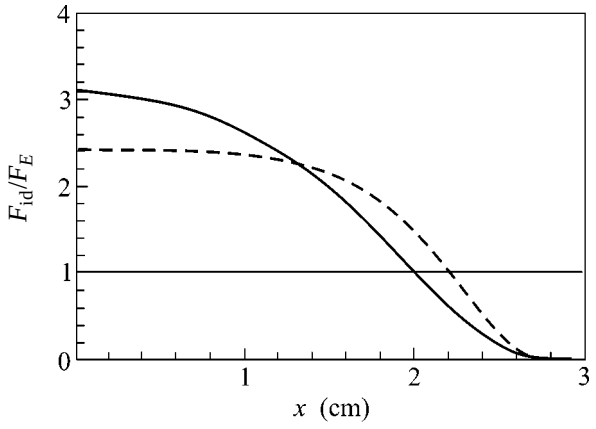

Fig. 4. Spatial dependence of the ratio of forces acting on a microparticle with a diameter of 1 μm in an rf discharge; the ratio of the ion-drag force F_{id} to the electrostatic force F_E as a function of the coordinate x ($x = 0$ corresponds to the center of the discharge zone). The solid line is for the pure argon discharge and the dashed line is for $[O_2]/[Ar] = 0.01$.

[7] Void is a cavity in the discharge central zone, where the dusty particles are absent. Void is often observed in gas-discharge dusty plasmas.

[8] It can easily be shown that the thermophoretic force comparable to the ion-drag and electrostatic forces requires the temperature gradients on the order of 10 K/cm for a microparticle of size 1 μm.

heating of the neutral gases by $\Delta T_n \simeq 1$ K. Even more efficient heating is induced by the metastable oxygen ion O(^{1}D). This effect is caused by a high concentration of O(^{1}D) in the discharge (because of the low excitation energy) and controlled by the rate of the quenching reaction Ar + O(^{1}D) $\longrightarrow$ Ar + O. In the general case, a change ΔT_n in the temperature of neutrals in their reactions of quenching metastable oxygen species is estimated by the formula

$$\Delta T_n \simeq \sum_i k_e^i n_e \frac{[O_2]}{[Ar]} \tau_D \epsilon_i, \quad \tau_D = L^2/D_n, \qquad (7)$$

where k_e^i is the constant for the formation of the ith metastable species (state) by electron impact and ϵ_i is the corresponding transition energy. For $[O_2]/[Ar] = 0.01$, the heating is mainly due to O(^{1}D) and is equal to a few degrees, giving rise to the thermophoretic force $F_T \simeq -a^2/\nu_{T_n} k_T \nabla T$ (k_T is the thermal conductivity coefficient) that can be comparable to the ion-drag forces for particles with size $a \geq 3$ μm. Note that the central zone of the discharge is heated stronger than its periphery, so that the thermophoretic force expels particles from the discharge. It is worth noting that the neutrals in argon plasma are heated by practically any impurity gas M. This heating is caused by the quenching reaction Ar* + M $\longrightarrow$ Ar + M of metastable argon atoms in their collisions with the impurity gas (as a rule, the rate constant k_q^{M} for this reaction markedly exceeds k_q^{Ar}). The efficiency of this process depends on the impurity concentration in the discharge, on the rate constant k_q^{M}, and on the fraction of the excited metastable-state energy expanded for heating the neutrals (a portion of this energy is expanded for the inelastic processes: ionization, dissociation, and excitation of the radiating M levels).

The heating of neutrals by dusty particles can also play a certain role if the concentration of the latter in the discharge is high enough. This is due to the fact that the plasma recombination at the particle surface releases energy that is comparable with the ionization energy. This heats the microparticle surface [18], which is cooled in collisions with neutrals. Assuming that this energy is fully transferred to the neutrals, one can estimate their heating as

$$\Delta T_n^d \approx \pi a \rho_C n_i \nu_{T_i} \epsilon_{\mathrm{ion}} \tau_D (n_d/n_n) \sim (10^{-2}\text{–}3) K. \qquad (8)$$

This heating is proportional to n_d and, hence, gives rise to the thermophoretic force that pushes apart the microparticle segregates.

Thus, the addition of molecular oxygen to argon plasma induces a number of important effects. The composition and transport properties of plasma change substantially: electron–ion plasma transforms to the ion–ion plasma. The appreciable decrease in the microparticle charge can also change the phase state (e.g., melt plasma crystal) and the configuration of dusty structures. The electric field also decreases in the discharge, thereby changing the force balance for the dusty particle; in particular, the void size markedly increases. In addition, the metastable argon and oxygen states initiate heating of the neutral gas, and the corresponding induced thermophoretic force makes a considerable contribution to the force balance for dusty particles.

REFERENCES

1. *Dusty Plasmas*, Ed. by A. Bouchoule (Wiley, Chichester, 1999).
2. J. H. Chu and I. Lin, Phys. Rev. Lett. **72**, 4009 (1994).
3. H. Thomas and G. E. Morfill, Nature **379**, 806 (1996).
4. V. N. Tsytovich, Usp. Fiz. Nauk **167**, 57 (1997) [Phys. Usp. **40**, 53 (1997)].
5. H. M. Thomas and G. E. Morfill, Contrib. Plasma Phys. **41**, 255 (2001).
6. G. Morfill *et al.*, in *Dusty Plasmas in the New Millennium: Third International Conference on the Physics of Dusty Plasmas*, Ed. by R. Bharuthram *et al.* (AIP, Melvill, N.Y., 2002), p. 3.
7. G. E. Morfill, H. M. Thomas, U. Konopka, *et al.*, Phys. Rev. Lett. **83**, 1598 (1999).
8. P. K. Shukla and A. A. Mamun, *Introduction to Dusty Plasma Physics* (Inst. of Physics, Bristol, 2002).
9. S. A. Khrapak, A. V. Ivlev, and G. E. Morfill, Phys. Rev. E **64**, 046403 (2001).
10. I. Schweigert, A. Alexandrov, and F. Peeters, in *Proceedings of 10th Dusty Plasma Workshop, US Virgin Island, USA, 2003*.
11. S. A. Khrapak, A. V. Ivlev, G. Morfill, and H. Thomas, Phys. Rev. E **66**, 046414 (2002).
12. B. Klumov, A. Ivlev, and G. Morfill, in *Dusty Plasmas in the New Millennium: Third International Conference on the Physics of Dusty Plasmas*, Ed. by R. Bharuthram *et al.* (AIP, Melvill, N.Y., 2002), p. 349.
13. M. A. Lieberman and A. J. Lichtenberg, *Principles of Plasma Discharges and Material Processing* (Wiley, New York, 1994).
14. V. N. Tsytovich, G. E. Morfill, and H. Thomas, Plasma Phys. Rep. **28**, 623 (2002).
15. C. W. Gear, *Numerical Initial Value Problem in Ordinary Differential Equations* (Prentice Hall, Englewood Cliffs, N.J., 1971).
16. H. Rothermel, private communication (2002).
17. H. Rothermel, T. Hagl, G. E. Morfill, *et al.*, Phys. Rev. Lett. **89**, 175001 (2002).
18. A. M. Ignatov, Fiz. Plazmy **28**, 919 (2002) [Plasma Phys. Rep. **28**, 847 (2002)].

Translated by V. Sakun

JETP Letters, Vol. 78, No. 5, 2003, pp. 305–308. Translated from Pis'ma v Zhurnal Éksperimental'noĭ i Teoreticheskoĭ Fiziki, Vol. 78, No. 5, 2003, pp. 753–756.

Microscopic Inhomogeneities in a $La_{1-x}Sr_xMnO_3$ ($x = 0.175$) Manganite Crystal and Generation of Coherent Magnetoelastic Oscillations on These Inhomogeneities

Kh. G. Bogdanova[1], A. R. Bulatov[2], V. A. Golenishchev-Kutuzov[1], A. V. Kapralov[2], and A. V. Potapov[2]

[1]*Kazan Physicotechnical Institute, Kazan Scientific Center, Russian Academy of Sciences, Sibirskiĭ trakt 10/7, Kazan 29, Tatarstan, 420029 Russia*

[2]*Kazan State Power Engineering University, Krasnosel'skaya ul. 51, Kazan, Tatarstan, 420066 Russia*

Received July 22, 2003

The temperature dependences of the amplitude and velocity of ultrasonic waves at a frequency of 770 MHz were measured in a $La_{1-x}Sr_xMnO_3$ ($x = 0.175$) manganite single crystal. Magnetoelastic wave generation was observed near the magnetic phase transition. The temperature dependences of the magnetization and magnetostriction correlated with the temperature behavior of the amplitude and velocity of the magnetoelastic wave, which suggests that the coherent magnetoelastic oscillations were generated on microscopic inhomogeneities (magnetoelastic domains) typical for a manganite of the given composition. © *2003 MAIK "Nauka/Interperiodica".*

PACS numbers: 75.80.+q

Unusual physical characteristics of lanthanum–strontium manganites with a Sr content of 0.15–0.18 have long attracted considerable attention of researchers. In this range of x, structural transition from a rhombohedral to an orthorhombic structure occurs. In addition, one or possibly several structural transitions occur with changing temperature at a constant concentration of Sr ions. The magnetic structure also changes; there is a considerable jump in the curve for paramagnetic–ferromagnetic phase-transition temperature T_c (from T_c = 240 K at $x = 0.155$ to T_c = 291 K at $x = 0.185$) [1, 2]. The type of electrical conduction also changes from dielectric ($x \le 0.17$) to metal conduction ($x \ge 0.175$). The transition parameters can be changed considerably by exposure to a magnetic field; for example, colossal magnetoresistance (CMR) is observed. Thus, it can be concluded from the data presented above that manganites of the given compositions have a soft crystal lattice susceptible to structural changes under the action of temperature, magnetic field, and the cooperative Yahn–Teller effect for Mn^{3+} ions.

In recent years, considerable attention has been given to various types of nano- and microsized inhomogeneous states caused by the spin, charge, or orbital ordering. Presumably, the maximal diversity of such inhomogeneities (especially of microscopic size) can be observed in the manganites of the above-mentioned composition because of the competition between different magnetic and structural states. The possibility of microstructures existing within the indicated range of Sr concentration was pointed out by Darling *et al.* [3], who assumed that the microstructures appear in the rhombohedral phase, where small regions with identical rhombohedral distortions, different from the original cubic structure, were formed. Elastic stresses occurring at the boundaries of the structural inhomogeneities indicate that these inhomogeneities can be classified as structural elastic domains. According to the calculations made in [3], the energy difference between the rhombohedral and more distorted orthorhombic lattices is small, so that exposure to a magnetic field of several Tesla can cause the transition from one structure to the other.

The possibility of microscopic structural inhomogeneities appearing due to the coexistence of the orthorhombic and rhombohedral phases was also pointed out in [4]. Inhomogeneous states were experimentally detected in manganites using ^{55}Mn NMR spectroscopy [5], ferromagnetic resonance [6], and neutron diffraction [7]. At present, the majority of scientists accept a model explaining the inhomogeneity by the phase layering caused by the appearance of a region of coexistence of different magnetic or structural phases in certain concentration or temperature ranges.

Ultrasonic studies provide certain additional possibilities for the examination of the specific features of structural and magnetic phase transitions and various inhomogeneities in the spin and charge ordering. First, the ultrasound velocity depends on the type of elastic and magnetoelastic interactions, which change considerably upon phase transition. Second, the interaction with ultrasound is especially strong if the inhomogene-

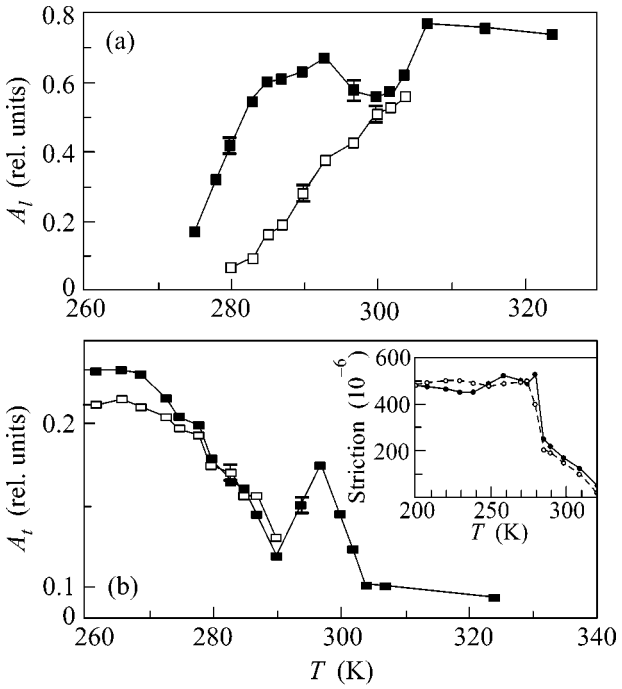

Fig. 1. Temperature dependences of the amplitude of (a) longitudinal and (b) transverse ultrasound modes: (■) zero-field results and (□) results obtained in H = 1 T. The insert in Fig. 1b shows the temperature dependence of magnetostriction in a $La_{0.83}Sr_{0.17}MnO_3$ sample in (●) zero magnetic field and (○) in the field H = 1 T (data taken from [8]).

ity size corresponds to the ultrasound wavelength, so that the use of such high-frequency oscillations makes it possible to study inhomogeneous or multiphase formations in manganites. Third, the high frequency of ultrasound makes it possible to overcome the gap in the spin-wave spectrum and thus use the dynamic interaction between the spin and elastic waves occurring in magnetically ordered manganites [8]. It was not surprising that the conclusions about the structural inhomogeneities made in [3, 4] were based on the results of experiments with ultrasound in a frequency range from 1 to 3 MHz. However, the ultrasound wavelength corresponding to this megahertz range (~5–10 mm) was many orders of magnitude greater than the size of the assumed inhomogeneities.

Taking into account the aforesaid, we used ultrasound at a frequency of 700 MHz for studying the specific features of phase transitions and possible microscopic inhomogeneities [9]. A $La_{1-x}Sr_xMnO_3$ (x = 0.175) single-crystal sample was chosen for the study, because at this concentration of Sr ions, the temperatures of structural and magnetic phase transitions were most close to each other and the maximal value of CMR was observed. The sample had the shape of a rectangular 4.85 × 8.2 × 7.9-mm parallelepiped with faces parallel to an accuracy of several seconds. The sample faces were perpendicular to the cubic axes [100], [010], and [001]. Ultrasound pulses ($\tau \cong$ 0.5–0.8 μs) were excited and received using piezoelectric rod transducers. The pulses propagated along the [100] axis. The temperature dependences of the velocity and attenuation of ultrasound were measured in the range from 260 to 340 K in a magnetic field H = 1 T using the transducer–sample–transducer scheme. The pulse duration was comparable to the time of its propagation through the sample. As a consequence, several oscillation modes could be simultaneously generated in the sample because of elastic or magnetic nonlinearity. These oscillations became coherent due to a high acoustic Q factor ($\geq 10^3$).

Long piezoelectric transducers used in the experiment made it possible to separate in time the ultrasound pulses corresponding to different oscillation modes and, therefore, propagating with different velocities. A broad-band receiver detected the pulses at the output of the receiving piezoelectric transducer. The single crystal used in the experiment was grown in the laboratory of A.M. Balbashov (Moscow Power Institute). X-ray spectral analysis showed that the crystal was phase- and chemically homogeneous.

Study of the propagation of a quasi-longitudinal wave gave the most interesting results. The wave velocity and attenuation changed little in the temperature range from 310 to 340 K (Figs. 1, 2a). The constancy of the ultrasound velocity also indicated that it continued to propagate in the quasi-longitudinal mode. The magnetic field applied to the sample had virtually no effect on the parameters of the acoustic wave.

The first anomaly in the velocity and attenuation of the quasi-longitudinal wave was observed at T = 305 K. Taking into account the temperature hysteresis, this anomaly was explained by a first-order transition (partial transition from the rhombohedral to the orthorhombic phase). This conclusion was based on the fact that the second hysteretic change in the parameters of ultrasonic wave was observed at T = 220 K [10] and indicated the complete transition to the orthorhombic structure.

The second anomaly was observed at T = 283 K. It was caused by the magnetic phase transition to the ferromagnetic phase (this conclusion was substantiated by magnetic measurements [10]). Considerable changes in the amplitude and the velocity of the quasi-longitudinal mode were observed below T = 300 K, excluding the temperature intervals where the changes in the ultrasound parameters were caused by the structural and magnetic phase transitions. Within this temperature range, the application of the magnetic field led to an even sharper decrease in the amplitude and an increase in the velocity of the wave.

Beginning at T = 305 K and below, a new ultrasonic pulse was detected simultaneously with the quasi-longitudinal wave pulse. The phase velocity V_t of the new pulse was determined from the time of its propagation through the sample. It varied in a range (2.5–2.9) ×

10^5 cm/s and depended on the temperature of the sample (Fig. 2b). The amplitude of the new pulse increased as the temperature decreased to $T = 270$ K; further decrease in temperature had almost no effect on the pulse amplitude. The character of an increase in amplitude coincided with the temperature behavior of the sample magnetization. Exposure to the magnetic field led to an increase in the amplitude of the oscillation mode under consideration; thus, the effect of the magnetic field on this mode was opposite to the field effect on the quasi-longitudinal mode and also terminated at $T \leq 270$ K. The velocity of the mode under consideration decreased near the magnetic phase transition and increased as the sample was exposed to the magnetic field (Fig. 2b). Thus, taking into account the phase velocity and the effects of the magnetic field and temperature on the amplitude and V_t, the mode under consideration can be classified as a magnetoelastic mode.

The problem of transformation of the quasi-longitudinal wave to the quasi-transverse magnetoelastic wave is of particular importance. It is well known that a purely longitudinal wave and two degenerate transverse waves propagate in crystals only in high-symmetry directions. Therefore, in the absence of magnetoelastic coupling, the dispersion relations for the velocities of elastic waves with an arbitrary direction of wave vectors are rather complicated. The pattern of propagation of elastic waves becomes even more complicated if the magnetoelastic interaction is taken into account. In the case of wave propagation along high-symmetry directions, only transverse waves are coupled to magnons; but if the wave propagates in an arbitrary direction, the longitudinal elastic mode is also coupled to the magnon spectrum. This is precisely the case that occurs for a quasi-longitudinal ultrasonic wave propagating in a rhombohedral manganite sample of given composition (Figs. 1a and 2a). As follows from [11], the mode transformation observed in the experiment could be most effectively induced by the displacement of the boundaries of magnetoelastic domains or by changes in their size (magnetostriction). The coupled magnetoelastic waves are amplified under conditions of dimensional acoustic resonance, i.e., when the size of the sample or the magnetoelastic inhomogeneities (L) is a multiple of the acoustic wavelength. The acoustic nonlinearity induced in a sample with strong magnetoelastic interaction gives rise to a spectrum of higher harmonics:

$$f_n = V(2n + 1)/2L; \quad n = 0, 1, 2, \ldots.$$

Although the harmonic amplitudes decrease with increasing n, effective oscillations can be expected for the first harmonics. At a frequency $f = 7 \times 10^8$ Hz, the acoustic wavelength falls within the range of several micrometers. Therefore, in principle, the acoustic waves with different polarization propagating along different directions of the crystal can be effectively transformed into magnetoelastic waves on the nanostructures of hundreds or thousands of angstroms in

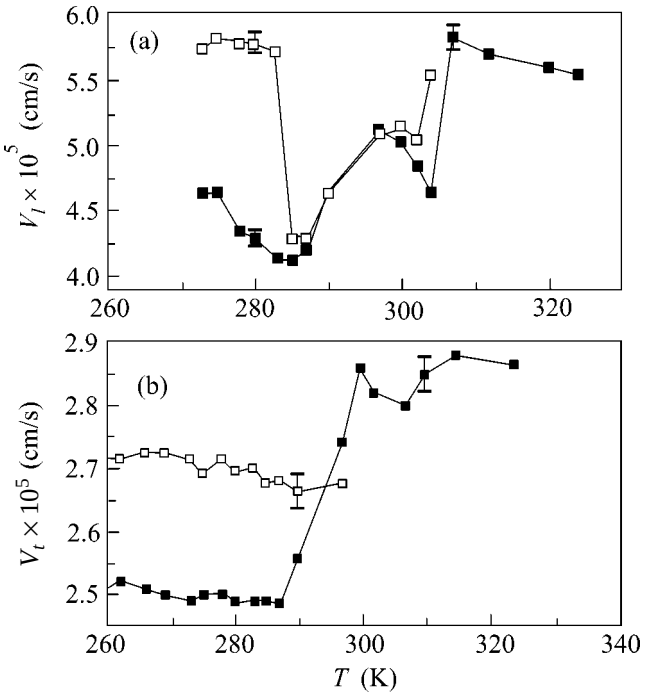

Fig. 2. Temperature dependences of the velocity of (a) longitudinal and (b) transverse ultrasound modes: (■) zero-field results and (□) $H = 1$ T.

size. Assuming that, under certain concentration and temperature conditions, the size of the microscopic inhomogeneities generated in the sample corresponds to the spectrum of magnetoacoustic oscillations, we can expect to observe two types of output acoustic waves transformed due to magnetoelastic interaction. It should be noted that the magnetoelastic oscillations are induced on virtually all magnetic inhomogeneities, but the coherent mode is generated only by the multiple reflection of oscillations from the plane-parallel faces of a sample with a high Q factor (principle of coherence generation in an acoustical resonator). Theoretical calculations and experimental results show that the generation efficiency for the magnetoelastic oscillations in a homogeneous sample is an order of magnitude lower than in a sample containing microscopic inhomogeneities, which act as microscopic magnetoelastic domains. The temperature behavior of magnetostriction provides an additional corroboration of the model suggested, because the magnetoelastic interaction is proportional to magnetostriction, whose temperature behavior was studied in [8]. Thus, there are reasons to believe that an increase in magnetostriction from zero at $T \geq 300$ K to 5×10^{-4} at $T \leq 260$ K observed in a sample with similar composition ($x = 0.17$) and caused by an increase in the ferromagnetic phase volume can lead to effective magnetoelastic wave generation on the inhomogeneities. Such an increase in magnetostriction correlates with a change in the ultrasound velocity,

which is also proportional to the magnetoelastic interaction.

The temperature dependence of the amplitude of magnetoelastic oscillations in magnetic field correlates with the temperature behavior of the sample magnetization and magnetostriction (Fig. 1b). The intensity of magnetoelastic oscillations in the applied magnetic field (H = 1 T) increases at T_c, which correlates with a similar jump in magnetostriction and a sharp decrease in the longitudinal wave intensity at the same temperature. The latter can be caused only by a decrease in the nonmagnetic phase volume. As the temperature decreases to 260 K and the magnetization and striction cease to increase, the amplitude of magnetoelastic oscillations in the magnetic field slightly decreases. This decrease corresponds to a field-induced decrease in magnetostriction with magnetic field in the same temperature range. The maximal change in magnetostriction occurs at $0.8 \le H \le 1.5$ T. Thus, the nature of the detected microscopic inhomogeneities remains open for discussion. In our opinion, their formation is originally caused by a two-phase structural state (rhombohedral and orthorhombic phases) over a broad temperature range. It is the onset of the revealed structural phase transition that correlates with the second ultrasonic mode generation. The internal energy of the orthorhombic phase is somewhat greater than that of the rhombohedral phase, so that the magnetization processes are different for the two phases. Magnetization of the orthorhombic phase competes with the structural scatter of the unit-cell axes. Therefore, it is safe to assume that the compound under consideration contains randomly distributed magnetoelastic domains formed by structural inhomogeneities.

Thus, this work has demonstrated the possibility of generating magnetoelastic domains with elastic stresses at their boundaries. Oscillations of these domains in the ultrasonic wave field lead to magnetoelastic wave generation. If the duration of a quasi-longitudinal ultrasound pulse is comparable to the time of its propagation through a sample with a high acoustic Q factor, a quasi-coherent magnetoelastic wave is generated in the sample.

This work was supported by the Russian Foundation for Basic Research, project no. 02-04-16440.

REFERENCES

1. A. Urushibara, Y. Moritomo, T. Arima, *et al.*, Phys. Rev. B **51**, 14103 (1995).
2. B. Dabrowski, X. Xiong, Z. Bukowski, *et al.*, Phys. Rev. B **60**, 7006 (1999).
3. E. Darling, A. Migliori, E. G. Moshopoupou, *et al.*, Phys. Rev. B **57**, 5093 (1998).
4. R. I. Zainullina, N. G. Bebenin, A. M. Burkhanov, *et al.*, Phys. Rev. B **66**, 064421 (2002).
5. E. Dagotto, T. Hotta, and A. Moreo, Phys. Rep. **344**, 1 (2001).
6. N. A. Viglin, S. V. Naumov, and Ya. M. Mukovskiĭ, Fiz. Tverd. Tela (St. Petersburg) **43**, 1855 (2001) [Phys. Solid State **43**, 1934 (2001)].
7. Y. Yamada, O. Hino, S. Nohdo, *et al.*, Phys. Rev. Lett. **77**, 904 (1996).
8. A. Asamitsu, Y. Moritomo, R. Kutai, *et al.*, Phys. Rev. B **54**, 1716 (1996).
9. Kh. G. Bogdanova, V. A. Golenishchev-Kutuzov, V. E. Leont'ev, *et al.*, Prib. Tekh. Éksp., No. 3, 1 (1997).
10. Kh. G. Bogdanova, A. R. Bulatov, V. A. Golenishchev-Kutuzov, *et al.*, Phys. Solid State **45**, 298 (2003).
11. E. A. Turov and A. A. Lugovoĭ, Fiz. Met. Metalloved. **50**, 903 (1980).

Translated by K. Chamorovskiĭ

JETP Letters, Vol. 78, No. 5, 2003, pp. 309–313. Translated from Pis'ma v Zhurnal Éksperimental'noĭ i Teoreticheskoĭ Fiziki, Vol. 78, No. 5, 2003, pp. 757–762.

On the Possibility of the Direct Study of Local Electron–Phonon Interaction in Semiconductors

V. Gavryushin

Institute of Materials Science and Applied Research and Semiconductor Physics Department, Vilnius University, Vilnius, 2010 Lithuania

e-mail: vg093ff@voruta.vu.lt

Received June 30, 2003; in final form, July 24, 2003

Local electron–phonon interaction in deep-level states of defects in semiconductors was studied by induced absorption spectroscopy. Using ZnS:Cu single crystals as an example, it was shown that the laser modulation of two-step impurity absorption is an efficient technique for direct investigations of phonon relaxation effects in deep-level states. It was shown that the localized states in ZnS are prone to extremely strong electron–phonon coupling. © *2003 MAIK "Nauka/Interperiodica".*

PACS numbers: 71.38.-k; 71.55.Gs

The relaxation of carriers in semiconductors is primarily determined by the electron–phonon interaction (EPI). With an increasing degree of carrier localization, the electron–phonon coupling strength sharply increases, because the area of the overlap between the carrier and phonon states in the *k* space of wave vectors increases. It is known that the spectra and efficiency of radiative recombination essentially depend on the presence and properties of deep local centers (DCs). Correspondingly, the phenomenon of local EPI in the states of DCs are of special interest in the formation of radiationless recombination processes.

In this paper, we report a direct investigation of local EPI by the nonlinear spectroscopy of DCs in wide-band-gap ZnS:Cu single crystals. It was shown experimentally that laser modulation of two-step absorption (LM TSA) is an exceptionally efficient technique for directly studying phonon relaxation processes in the localized states of deep defects. The basic parameters were obtained, and a model of configuration coordinates was constructed for DCs in ZnS:Cu.

The full spectrum of the DCs observed was theoretically reconstructed using the minimum set of their parameters. As a result, it has become possible to correctly describe not only the energies of the edge of optical transitions, which are affected by the Stokes losses due to the Franck–Condon shift, but also the shape of their long-wavelength absorption broadened by electron–phonon interaction.

Earlier, the effect of the local EPI was usually investigated indirectly from the temperature dependence of the broadening of the long-wavelength edge of absorption spectra [1, 2]. A different method of directly studying the scattering of free electrons by phonons is based on the use of subpicosecond Raman spectroscopy [3].

As to the selection of ZnS:Cu as the subject of investigations, these are the crystals that gave rise to studying the phenomena of impurity luminescence (1866, [4]). Two-step processes of anti-Stokes excitation of PL were first observed in these systems. The newest nanotechnologies have also not disregarded this material [5, 6]. This classical phosphor turns out to be in demand for newly designed field-emission displays [7] and optical fiber sensors [8].

DCs are manifested in absorption spectroscopy by transitions to only one of the bands, which is characteristic of DCs. This is either the valence or the conduction band (Fig. 1). The type of the transitions (ionization or neutralization) is determined by the steady-state occupation of DCs or by the degree of compensation of the crystal, that is, the position of the Fermi level with respect to the energy levels of the defects (Fig. 1). Consequently, the same centers can differently manifest themselves in different samples of crystals, never revealing their full spectra. As is evident in Fig. 1, the spectral response will be formed by the photoionization of DCs in uncompensated samples (a) and, on the contrary, by the photoneutralization of DCs in compensated samples (b).

Thus, it is hardly possible to investigate the full absorption spectrum by traditional methods of steady-state spectroscopy. By the word "full" is meant the possibility of simultaneously detecting both neutralization "$v \longrightarrow D$" (Fig. 1b) and ionization "$D \longrightarrow c$" (Fig. 1a) transitions, because they both participate in the response of centers to their optical charge exchange.

During the optical charge exchange of local centers, lattice relaxation in the vicinity of the defect proceeds simultaneously. In other words, localized carriers generate phonons. This is described by the Franck–Condon rule of Stokes losses, which is illustrated by the model

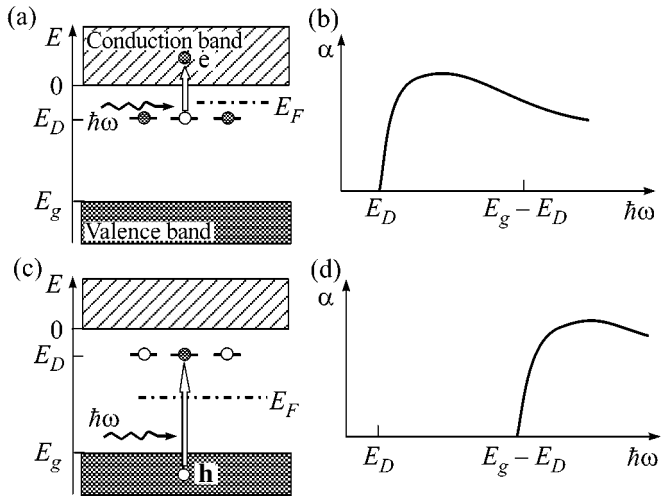

Fig. 1. Schematic diagram of the formation of spectra of steady-state absorption by deep centers (DCs) with differing degrees of occupation, that is, for crystals with differing positions of the Fermi level with respect to the DC states. (a), (b) The formation of the photoionization spectra $\sigma_{Dc}(\omega)$ of an uncompensated sample; (c), (d) the formation of the photoneutralization spectra $\sigma_{vD}(\omega)$ of a compensated crystal.

of diagrams of configuration coordinates (Fig. 2b). The energy losses ΔE_S (expenditures for the formation of phonons) at an interband transition through a localized state are $\Delta E_S = 2\Delta_{FC}$, because phonons are generated at both the stage of carrier localization and the stage of carrier liberation (Fig. 2b).

Thus, I wanted to show that the shape of the full absorption spectrum of DCs is modified by electron–phonon interaction not only as the broadening of the long-wavelength absorption edge but also as a short-wavelength shift of thresholds. In this case, the sum of the threshold energies $E_{vD} + E_{Dc}$ will be larger than the band gap width E_g by the value of the Stokes losses $\Delta E_S = 2\Delta_{FC}$.

Determination of the Stokes losses from measurements of the full absorption spectrum of deep centers is a direct method of studying the local EPI.

The full spectrum of DCs should be measured by transient spectroscopy techniques, using additional pulsed illumination. This creates nonequilibrium partial occupation of the states of the defect. Figure 3 illustrates the formation of the photoinduced spectrum $\Delta\alpha(\omega)$ in the presence of compensated DCs. Here, Figs. 3a and 3b demonstrate the appearance of two-step transitions, and Fig. 3c, their laser modulation. The initial part of the photoneutralization spectrum (Fig. 3d) and the full TSA spectrum (Fig. 3e) are given here. The reaction of two-step transitions (Fig. 3b) and their spectrum (Fig. 3e) to additional modulation by a laser pulse $\hbar\omega_L$ is shown (Fig. 3f) as the change of the absorption spectrum $\alpha(\omega)$ and (Fig. 3g) as the induced absorption spectrum $\Delta\alpha(\omega)$.

The experiments were carried out with the use of the so-called two-beam method of two-photon spectroscopy [9]. A xenon lamp ($\Delta t \approx 200$ μs) with a continuous spectrum, which was monochromatized after passing through the sample, was used as a probe source. The absorption of the probe light was modulated by pulses of a ruby laser ($\hbar\omega_L = 1.78$ eV, $\Delta t_L = 40$ ns). The experimental results are displayed in Figs. 4 and 5. The idea of the method is defined as LM TSA [9, 10] though deep levels. This method provides a possibility of separating out spectral contributions from different DCs using the difference in their effects of saturation with increasing modulation even in the case of the full energy overlap of their spectra [9, 10]. The basic set of phenomenological parameters and the composition of DCs can also be evaluated.

This method was used previously in studying and determining the properties of DCs in ZnTe [11], ZnSe [12], CdS [13], and ZnO [14] crystals. However, the studies [11–14] (modulation by a Nd^{3+} laser with $\hbar\omega_L = 1.17$ eV) were restricted by the fact that there were no possibility of detecting the induced signals with $\hbar\omega < \hbar\omega_L$, that is, in the spectral region in which the photo-

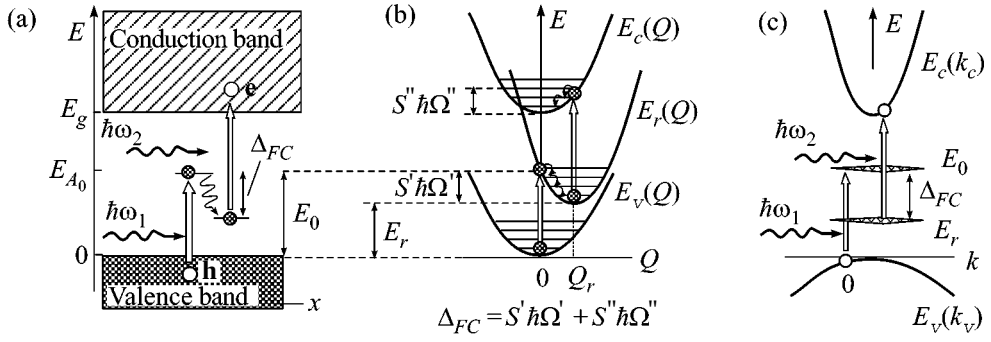

Fig. 2. Two-step optical transitions through deep centers subjected to local lattice relaxation presented within the models of (a) real space, (b) coordination coordinates, and (c) dispersion curves or "reciprocal space." Δ_{FC} designates the Franck–Condon losses due to the emission of S phonons of energy $\hbar\Omega$.

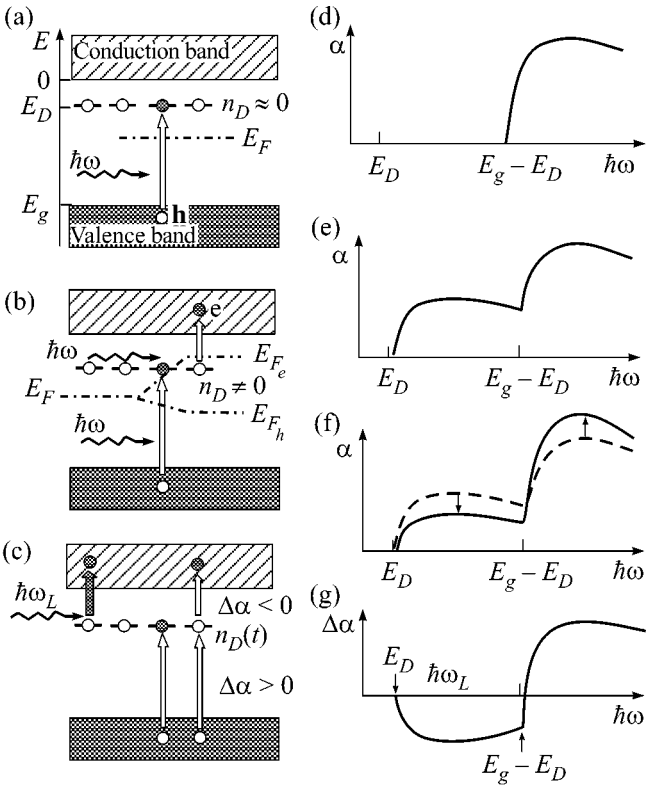

Fig. 3. Schematic diagram of the formation of the photoinduced absorption spectrum $\Delta\alpha(\omega)$ for compensated DCs. (a), (b) Manifestation of two-step transitions and (c) their laser modulation. (d) Photoneutralization spectrum and (e) full TSA spectrum. The reaction of two-step transitions (b) and their spectra (e) to additional modulation by a laser pulse $\hbar\omega_L$ is shown (f) as the change of absorption spectra $\alpha(\omega)$ and (g) as the induced absorption spectrum $\Delta\alpha(\omega)$.

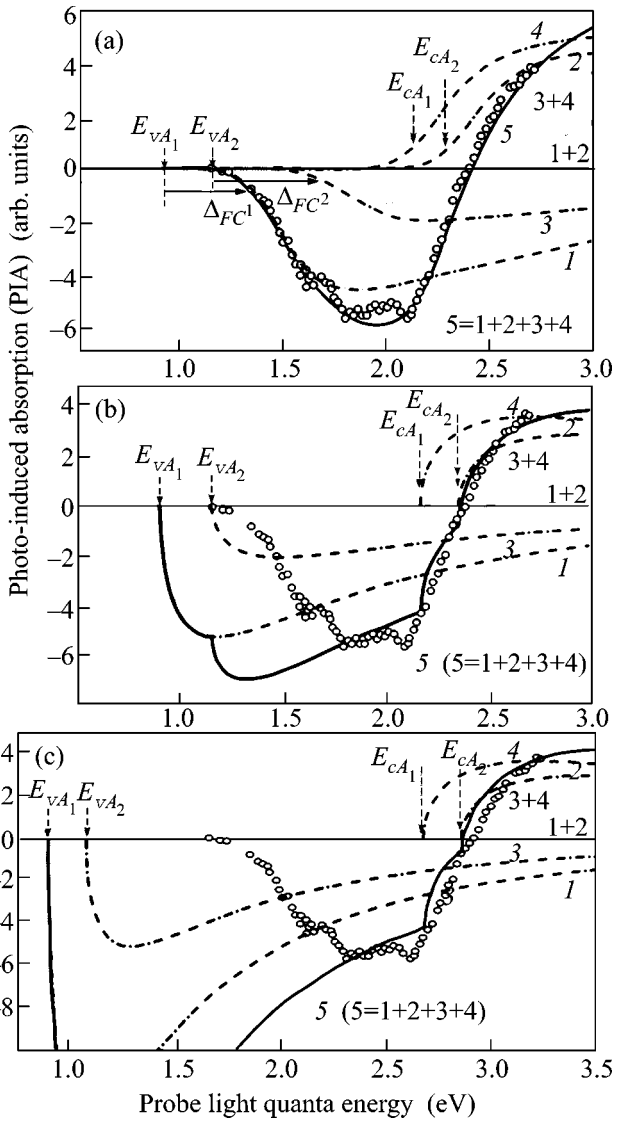

Fig. 4. Comparison of the experimental photoinduced absorption spectrum in ZnS:Cu at 300 K (points) formed by LM TSA processes with the calculated spectra in the form of a combination $\sigma_{Ac}(\omega) - \sigma_{vA}(\omega)$ of photoionization spectra $\sigma_{vA}(\omega)$ and photoneutralization spectra $\sigma_{Ac}(\omega)$ for two deep acceptors with $E_{cA} = 2.67$ eV and 2.83 eV. The spectra are presented for (a) transitions subjected to phonon relaxation according to Eqs. (1)–(3), (b), (c) the same DCs in a hard lattice within the Lucowsky model according to Eq. (4) for the states with the Stokes shift (b), when $E_{vA} + E_{Ac} + \Delta_{FC} = E_g$, and for the case of unrelaxed states (c) with $E_{vA} + E_{Ac} = E_g$. The components forming the spectrum by optical transitions (*1* and *3*) $v \longrightarrow A$ and (*2* and *4*) $A \longrightarrow c$ are shown separately and also in the form of their natural combination. Curve *5* corresponds to the calculated spectra of the resulting LM TSA.

ionization thresholds of DCs can be observed. When the ruby laser was used, two-photon excitation of the crystal and, correspondingly, the modulation of DC occupation by the capture of free carriers [11, 13] dominated in these materials. As a result, it was not possible to study directly the EPI effect in practice.

For ZnS crystals with a wider band gap, two-photon excitation is absent because $2\hbar\omega_L < E_g$. Therefore, this material is suitable for measurements of the full LM TSA spectra and, correspondingly, for studies of local lattice relaxation upon optical charge exchange of DCs.

The experimental results shown in Figs. 4 and 5 confirm that the induced bleaching on the long-wavelength side of the absorption spectra (Fig. 4) along with the extended kinetics of the signals and the saturated intensity dependences (Fig. 5) are typical manifestations of LM TSA [9, 10].

As usual, the spectra (Fig. 4) are complex, being formed by the overlap of the signals of induced bleaching and absorption from each kind of center [6–9]. The spectral dependences correspond to a combination of the spectra of photoionization and photoneutralization cross-sections in the form $[\sigma_{cA}(\omega) - \sigma_{vA}(\omega)]$ (see Fig. 3g). The modulation of TSA occurs as a result of the change of the occupation of DCs due to the direct absorption of laser radiation with $\hbar\omega_L > E_i$ by the impurity center, as is shown in Fig. 3c.

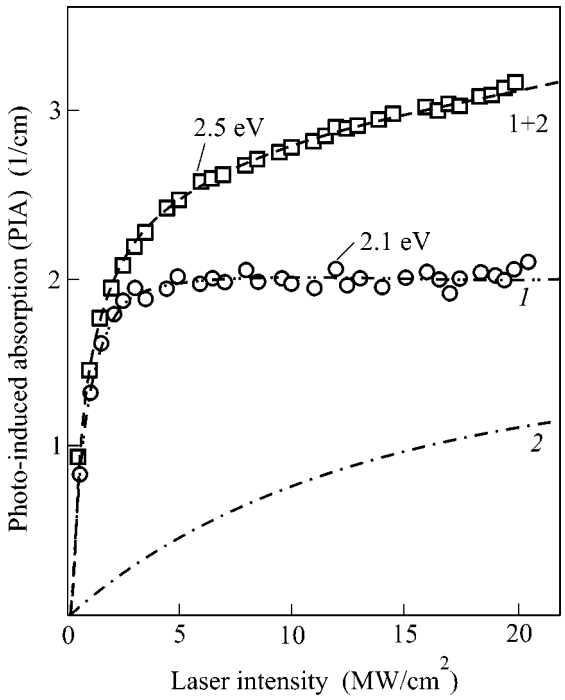

Fig. 5. Dependences of the amplitude of the signals of induced impurity absorption in ZnS:Cu on the optical modulation intensity measured at $\hbar\omega = 2.1$ and 2.5 eV. Curves *1* and *2* are the calculated dependences. Curve *2* was obtained under the assumption that the dependence at 2.5 eV is due to the overlap of the signals from both DCs (1 + 2).

An analysis of the saturating dependences $\Delta\alpha(I_L)$ of the induced signals on the intensity of the modulating laser radiation allows one to determine the absolute values of the photoionization cross-section due to the absorption of laser quanta σ_{vA} (see table). Figure 5 demonstrates experimental dependences $\Delta\alpha(I_L)$ for two spectral regions of photoinduced absorption and the corresponding theoretical curves calculated according to [6–9]. It is evident that the signals with the quantum energies above 2.1 eV are formed by both centers and those below 2 eV by only the deeper DC, which allows their contributions to the full spectrum to be separated with certainty.

Table

Parameters of centers	*1*	*2*
Photoionization cross-section $\sigma_{vA}(\omega_L)$, cm^2	0.63×10^{-17}	0.475×10^{-18}
Lifetimes of localized holes τ, μs	1.2	0.5
Hole binding energy, E_{vA}, eV	1.415	1.65
Photoneutralization edge, E_{cA}, eV	2.83	2.67
Stokes losses due to the Franck–Condon shift, Δ_{FC}, eV	0.515	0.59
Electron–phonon coupling constant a_A	6.55	7.0

The figure shows that both spectra as well as their intensity dependences are formed mainly under the effect of two DC levels. The energy levels of these centers lie in the lower part of the band gap and act as compensated deep acceptors. This follows from special measurements of excitation spectra (are not presented here), which describe the dependence of the bleaching effects on the spectral composition of the probe source maintaining the initial occupation of DCs [12–14].

In our case, the spectrum edge is substantially smeared; hence, it is possible that phonons make an effect on the formation of the spectra [2, 15]. The LM TSA spectra can be described reasonably in the framework of the δ-potential model with regard to electron–phonon interaction [2]. The theoretical spectrum of the photoneutralization cross-section and its temperature variations can be obtained in the following way [2]:

$$\sigma_{cA}(T, \omega) = \frac{\sigma_0}{\hbar\omega\sqrt{\pi\Theta_A}}\int_1^\infty \frac{\sqrt{x-1}}{x^2}\exp\left[-\frac{(x-\Re)^2}{\Theta_A}\right]dx. \quad (1)$$

Here, Θ_A has the meaning of the spectrum smoothing parameter due to EPI

$$\Theta_A(T) = \left(\frac{a_A\hbar\Omega}{\aleph}\right)^2\left[\coth\left(\frac{\hbar\Omega}{2kT}\right) - 1\right], \quad (2)$$

a_A is the dimensionless electron–phonon coupling constant, $\hbar\Omega$ is the energy of local lattice oscillations, and $\hbar\omega$ is the photon energy;

$$\aleph = \frac{m_v^*}{m_c^*}E_{cA}; \quad \Re = \frac{\hbar\omega - E_{vA} + \aleph}{\aleph}. \quad (3)$$

An expression similar to expression (1) but with different $\aleph = E_{vA}$ and $\Re = \hbar\omega E_{vA}^{-1}$ can be obtained for photoionization spectra. Expression (1) can be compared with the spectrum in the simple δ-potential approximation by Lucowsky [16] for deep centers in a "hard" lattice

$$\sigma_{Luc}(\omega) \propto \frac{E_I^{1/2}(\hbar\omega - E_I)^{N/2}}{(\hbar\omega)^3}. \quad (4)$$

Here, $N = 1$ for the allowed transitions and $N = 3$ for the forbidden transitions. E_I is the ionization energy of the DCs.

A comparison of the experimental spectrum (points) and theoretical calculations is given in Fig. 4. Curve *5* in Fig. 4a is the spectrum with the complete consideration of electron–phonon interaction (1) for two centers with $E_{cA} = 2.67$ and 2.83 eV. On the other hand, curves in Figs. 4b and 4c are shown for comparison and correspond to the case of the same centers for the hypothetical "hard" lattice by Lucowsky (4). The components

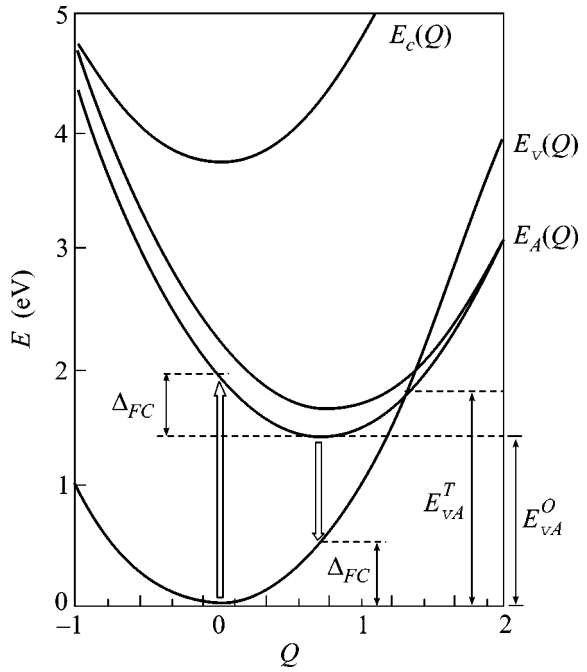

Fig. 6. Model of configuration coordinates for the deep centers studied in the linear approximation.

that form the spectrum by means of optical transitions $v \longrightarrow A$ (*1* and *3*) and $A \longrightarrow c$ (*2* and *4*) are shown separately and also in the form of their natural combinations *1* + *2* and *3* + *4*. Curves *5* are the resulting LM TSA spectra according to expressions (1)–(3).

The spectra of the Lucowsky type (4) presented in Figs. 4b and 4c are characterized by the inclusion of the effect of Stokes losses (b), when $E_{vA} + E_{Ac} + \Delta_{FC} = E_g$. The curves in Fig. 4c correspond to simple unrelaxed states with $E_{vA} + E_{Ac} = E_g$. The differences in the calculated spectra in Fig. 4 demonstrate how strong the EPI effect can be on the formation of the DC spectra in wide-band-gap semiconductors. Thus, without regard for EPI, the error in the estimate of the center binding energy is about $\Delta_{FC} \approx 0.5$–0.6 eV, and the error for the description by the Lucowsky equation (4) is up to 1 eV and more.

In studying deep centers by this method, one can obtain the same parameter of the electron–phonon coupling strength a_A twice: (1) in describing the broadening of the long-wavelength absorption edge and (2) in describing the Stokes losses due to EPI. The coincidence of these parameters in both cases confirms that the identification of the spectra justifies the approximations used.

These calculations form the basis for the model of DC configuration coordinates (Fig. 6), which can be used for determining the energy of the unperturbed states E_m and the corresponding Stokes losses Δ_{FC} due to lattice relaxation upon optical charge exchange. These parameters and the electron–phonon coupling constant a_A were obtained (see table) under the assumption that the energy of local oscillations $\hbar\Omega_{LO}$ equals 33 meV.

Thus, the advantages of nonlinear spectroscopy allows one to observe the full spectra of deep local centers in crystals, that is, to detect simultaneously the interrelated spectra of both photoionization and photoneutralization.

The most important result is that the local electron–phonon interaction in crystals has been studied directly. The data obtained allowed the full experimental spectrum to be theoretically reconstructed with the use of only a minimum set of parameters. Furthermore, with the use of the same parameters of DC binding energies and electron–phonon coupling strengths, it was possible to describe not only the edges of optical transitions shifted by Stokes losses but also the shape of the long-wavelength absorption edge broadened by electron–phonon interaction. The results show that deep localized states in wide-band-gap crystals of the ZnS type are characterized by extremely strong effects of electron–phonon coupling.

REFERENCES

1. H. Kukimoto, C. H. Henry, and F. R. Merritt, Phys. Rev. B **7**, 2486 (1973).
2. A. Kopylov and A. Pikhtin, Fiz. Tverd. Tela (Leningrad) **16**, 1837 (1974) [Sov. Phys. Solid State **16**, 1200 (1974)]; Fiz. Tekh. Poluprovodn. (Leningrad) **10**, 15 (1976) [Sov. Phys. Semicond. **10**, 7 (1976)].
3. K. Tsen, D. Ferry, A. Botchkarev, *et al.*, Appl. Phys. Lett. **71**, 1852 (1997).
4. E. Becquerel, C. R. Acad. Sci. **62**, 999 (1866).
5. A. A. Bol and A. Meijerink, J. Lumin. **87–89**, 315 (2000).
6. W. Que, Y. Zhou, Y. L. Lam, *et al.*, Appl. Phys. Lett. **73**, 2727 (1998).
7. W. B. Choi, D. S. Chung, J. H. Kang, *et al.*, Appl. Phys. Lett. **75**, 3129 (1999).
8. T. Pustelny and B. Pustelny, Opto-Electron. Rev. **10** (3), 193 (2002).
9. R. Baltramiejunas and V. Gavryushin, J. Cryst. Growth **101**, 699 (1990).
10. V. Gavryushin, G. Raciukaitis, D. Juodzbalis, *et al.*, J. Cryst. Growth **138**, 924 (1994).
11. R. Baltramiejunas, J. Vaitkus, and V. Gavryushin, Zh. Éksp. Teor. Fiz. **87**, 74 (1984) [Sov. Phys. JETP **60**, 43 (1984)].
12. R. Baltramiejunas, V. Ryzhikov, G. Raciukaitis, *et al.*, Physica B (Amsterdam) **185**, 245 (1993).
13. R. Baltramiejunas, V. Gavryushin, V. Kubertavicius, and G. Raciukaitis, Physica B (Amsterdam) **185**, 336 (1993).
14. R. Baltramiejunas, V. Gavryushin, V. Kubertavicius, and G. Raciukaitis, Fiz. Tverd. Tela (Leningrad) **25**, 3596 (1983) [Sov. Phys. Solid State **25**, 2068 (1983)].
15. M. Jaros, Phys. Rev. B **16**, 3694 (1977).
16. G. Lucowsky, Solid State Commun. **3**, 299 (1965).

Translated by A. Bagatur'yants

JETP Letters, Vol. 78, No. 5, 2003, pp. 314–318. Translated from Pis'ma v Zhurnal Éksperimental'noĭ i Teoreticheskoĭ Fiziki, Vol. 78, No. 5, 2003, pp. 763–767.

Photoconductivity of 2*D* Electrons over Helium in the Presence of Cyclotron Pumping

V. Shikin

Institute of Solid State Physics, Russian Academy of Sciences, Chernogolovka, Moscow region, 142432 Russia

Received July 24, 2003; in final form, August 6, 2003

Recent measurements of photoconductivity for 2*D* electrons at the helium surface in the presence of a magnetic field orthogonal to the 2*D* plane require a qualitative explanation, because of the very fact of its existence. Various scenarios of the effect are discussed, and arguments in favor of one of these—that which is associated with the emergence of thermoelectric power along a 2*D* charged system in a magnetic field under the effect of a spatially nonuniform external pumping—are presented. The corresponding nonuniform electron distribution δn_s (against the background of the uniform distribution) leads to the effect that is observed with the aid of Corbino disks and which consists in a change in the conductivity of the 2*D* system. © *2003 MAIK "Nauka/Interperiodica".*

PACS numbers: 73.20.-r; 73.50.Pz

Information about the high-frequency-pumping-induced photoconductivity $\delta\tilde{\sigma}$ of 2*D* electron systems in an orthogonal magnetic field appeared in the literature as far back as the 1970s (see the experiments reported in [1, 2] and performed with inversion layers in silicon). These experiments did not reveal anything remarkable, with the exception of the expected photopeak $\delta\tilde{\sigma}$ in the resonance region around $\omega \simeq \omega_c$, where ω and ω_c are, respectively, the external and the cyclotron frequency. In treating data from these experiments, the sensitivity of the current-carrier mobility to the electron temperature T_e was assumed to be obvious, although the fact of this dependence itself was not verified.

Later on, there appeared new photosensitive experiments for low-dimensional systems in a magnetic field. First of all, the experiments performed by Penning *et al.* [3, 4] with 2*D* electrons on helium are worthy of note. Among other things, these experiments revealed that the sign of the photoconductivity $\delta\tilde{\sigma}$ may be different, depending on experimental conditions, and that, on the magnetic axis, the positions of the peaks of cyclotron absorption and of the photoconductivity induced by this absorption do not coincide.

The studies reported in [5–11] and devoted to the details of the photoconductivity in well-conducting degenerate 2*D* electron systems based on GaAs are no less interesting. In the region of weak magnetic fields where $\omega \geq \omega_c$, these experiments reveal oscillations of the photoconductivity $\delta\tilde{\sigma}_{xx}(H)$ whose period is primarily dependent on a parameter γ that has nothing in common with the combination of quantities responsible for Shubnikov–de Haas oscillations, $\gamma = \omega/\omega_c$. The number of such resonances, corresponding to integral values of γ, depends greatly on the quality of the samples used, reaching two-digit numbers for the best of them [8] (which are characterized by an effective mobility in excess of 10^6 cm^2 (V s).

The results obtained in [3–11] suggest that there are a few reasons for the photoexcitation of 2*D* electron systems. Of primary importance is the behavior of the cross section in the scattering of 2*D* electrons by medium defects (impurities, phonons, etc.). If this cross section is energy-dependent, an increase in the electron temperature would inevitably affect the mobility of electrons and, hence, the 2*D* conductivity. An independent source of photosensitivity is associated with the discreteness of the electron spectrum in a magnetic field. Finally, the spatial nonuniformity of the problem due to a nonuniformity of irradiation is also operative. This channel of photosensitivity is less obvious than the preceding two and does not look very fundamental. However, there are some cases (including the case discussed below) in which only upon taking into account the nonuniformity of the problem does there arise the possibility of explaining the existence of photoconductivity and its sign.

Returning to electrons on helium, we note that the authors of [3, 4], as well as the authors of [1, 2], assumed the mobility of electrons on helium to be sensitive to the electron temperature and attributed the deviation of $\tilde{\sigma}$ from the reference level σ_0 predominantly to this. However, the calculation presented below reveals that the 2*D* gas-limited mobility μ_G of electrons, which is of greatest importance for the experiments reported in [3, 4], is independent of T_e in the range explored experimentally:

$$\mu_G = \frac{e\tau_G}{m}, \quad \tau_G = \frac{8meb}{3\pi\hbar a_o^2 N_G(T)}. \qquad (1)$$

0021-3640/03/7805-0314$24.00

Here, b is the electron-localization length in the vertical direction; a_0 is the amplitude for zero-angle electron scattering by an individual gas atom; and $N_G(I)$ is the volume density of gas atoms, which is dependent on the heat-bath temperature T. According to (1), the effective heating of the electrons, which is inevitably caused by the irradiation of the 2*D* system, does not affect their mobility.

Thus, even the original reasons that could be responsible for the effect of cyclotron-resonance-induced conductivity (CRIC) for electrons on helium remain uncertain.

The CRIC scenario proposed in the present study explains, at a qualitative level, the existence of the effect and a correct sign for the experiments reported in [3], which were performed under "unsaturated" conditions (in the case of saturation, the proper field of the electrons compensates the electric field confining the electrons near the surface of helium). It is shown that spatially nonuniform high-frequency radiation heats the 2*D* electron system selectively. The thermoelectric power that arises in this case, as usual (see [12]), between the middle and the periphery of the 2*D* system, is accompanied by a nonuniform (against the background of the mean uniform density n_s) rearrangement of the electron density, δn_s. It is this perturbation that leads to the effect that was observed in [3] with the aid of a system of Corbino disks (*a*, *b*, *c* in the figure) and which consists in a change in the conductivity of the 2*D* system:

$$\delta\tilde{\sigma} \simeq \sigma_o \delta n_s / n_s. \tag{2}$$

Here, σ_o is the conductivity of the 2*D* system in the absence of a high-frequency perturbation.

The thermal scenario of the CRIC effect in the gas region and in the absence of saturation is reasonably matched with more complicated manifestations of the effect [4] under the conditions of saturation.

1. Proceeding to implement the program outlined above, we will first specify, with the aid of the figure, various fields present in the problem. A lower electrode that is formed by a cylindrically symmetric system of Corbino disks *a*, *b*, and *c* is statically grounded. A static potential V, which confines 2*D* electrons to the surface of helium, is applied between an upper electrode (*1*) partly filled with a mesh, a protecting ring (*2*), and the Corbino disks. The equipotential lines of the static field in a resonator are represented by solid lines in the figure. The static features used in the main body of the present article are the radius S of the electron mirror at the surface of helium and the mean electron density n_s in it.

A weak measuring potential difference $\tilde{U}$ oscillating with a frequency Ω is applied between the Corbino electrodes *a*, *b*, and *c*.

An exciting waveguide of radius $L < S$ is connected to the resonator through the permeable mesh. The original high-frequency field of frequency ω has an amplitude E_o. The field $E_\parallel$ actually experienced by the 2*D* electron system must be determined self-consistently from a calculation of the coefficient R of reflection of a high-frequency signal from a flat resonator having a semitransparent upper electrode and an ideal lower electrode and containing a 2*D* charged system at the surface of helium.

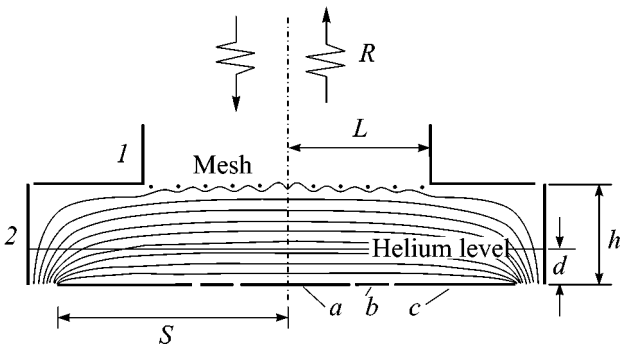

Scheme of the cell in [3] for implementing CRIC experiments: (*1*) upper electrode of the resonator with a "window" of radius L closed by a metallic mesh for the penetration of a high-frequency signal to the volume of the resonator, (*2*) protecting ring, and (*a*, *b*, *c*) electrodes in the base of the resonator that form a system of Corbino disks for measuring the effective conductivity of the electron layer at the surface of helium. The geometric parameters indicated in the figure are the following: S is the approximate radius of the electron disk; d is the thickness of the helium film; and h is the height of the resonator. The solid lines within the resonator give an idea of the shape of static equipotential lines between the upper and the lower plate of the resonator; R indicates the direction of the reflected high-frequency signal.

2. Let us now show that the gas-limited mobility μ_G of the electrons and their ripplon-limited mobility $\mu_\perp$ do not possess properties that are required for explaining the photoeffect observed in [3]. With an eye to the case of low electron densities, where single-electron approximation is valid in electron kinetics, we first present, following the traditional line of reasoning [13], the hierarchy of kinetic equations for an electron in an orthogonal magnetic field in the presence of a linearly polarized high-frequency electric field $E_\parallel$ directed along the 2*D* system. We have

$$f(\mathbf{p}) = f_o(p) + \mathbf{p}\mathbf{f}_1(p)/p + 0(f_2), \tag{3}$$

$$\frac{\partial f_o}{\partial t} - \frac{e}{2p}\frac{\partial}{\partial p}(p\mathbf{E}_\parallel \mathbf{f}_1) - \frac{1}{p}\frac{\partial}{\partial p}\left[pA\left(\frac{\partial f_o}{\partial p} + \frac{p}{mT}f_o\right)\right] = 0, \tag{4}$$

$$\frac{\partial \mathbf{f}_1}{\partial t} - e\mathbf{E}_\parallel \frac{\partial f_o}{\partial p} - \frac{e}{mc}[\mathbf{H}\mathbf{f}_1] + \nu\mathbf{f}_1 = 0. \tag{5}$$

.....

The kinetic coefficients A and ν for various types of collisions are defined below. In analyzing the properties of the mobilities μ_G and $\mu_\perp$, the field $E_\parallel$ is assumed to be uniform.

Equations (4) and (5) enter into an infinite hierarchy of coupled relations between distribution functions f_i. According to [13], the possibility of truncating this hierarchy at the level of Eqs. (4) and (5) is determined by the requirement

$$\delta(T_e)\frac{T_e - T}{T} \ll 1, \tag{6}$$

where $\delta(T_e)$ is the mean energy fraction lost per collision with a gas atom or a ripplon. Under the condition $\delta(T_e) \ll 1$, which is well satisfied in the case being considered, the inequality in (6) and, hence, formulas (7), (9), and (10) below remain meaningful even at sizable deviations of T_e from T.

Solving Eq. (5) for the case where the field $E_\parallel$ oscillates with a frequency ω, we obtain

$$\mathbf{f}_1(p) = -\mathbf{u}_G \partial f_o/\partial p, \tag{7}$$

$$\mathbf{u}_G = -e\mathbf{E}_\parallel[\tau'(\omega, \omega_c) + i\tau''(\omega, \omega_c)]/m, \tag{8}$$

$$\tau'(\omega, \omega_c) = \frac{1 + \omega^2\tau_G^2 + \omega_c^2\tau_G^2}{(1 - \omega^2\tau_G^2 + \omega_c^2\tau_G^2)^2 + 4\omega^2\tau_G^2}, \tag{8a}$$

$$\tau''(\omega, \omega_c) = \frac{1 + \omega^2\tau_G^2 - \omega_c^2\tau_G^2}{(1 - \omega^2\tau_G^2 + \omega_c^2\tau_G^2)^2 + 4\omega^2\tau_G^2}, \tag{8b}$$

$$\nu_G^{-1} = \tau_G = \frac{8meb}{3\pi\hbar a_o^2 N_G(T)}, \tag{8c}$$

where τ_G is the relaxation time for electron collisions with gas atoms.

Taking into consideration formulas (7) and (8), we can easily write a time-independent solution to Eq. (4) [14, 15]

$$\frac{\partial f_o}{\partial t} \simeq 0, \quad f_o(p) = \text{const} \times \exp\left\{-\frac{1}{mT}\int p dp\left[1 + \frac{(e\mathbf{u}_G(p)\mathbf{E}_\parallel)}{2A_G(p)}\right]^{-1}\right\}, \tag{9}$$

$$A_G(p) = \frac{\pi\hbar a_o^2 N_G(\epsilon_b + 3\epsilon/2)}{2mb}, \quad \epsilon_b = \hbar^2/2mb^2, \quad \epsilon = p^2/2m. \tag{9a}$$

According to (8c) and (9a), the properties of τ_G and A_G for electron collisions with helium atoms are independent of p (for A_G, this statement is valid as long as the inequality $\epsilon_b \gg T$ is satisfied). As a result, the distribution $f_o(p)$ (9) has a Maxwellian form, with the electron temperature T_e being

$$T_e = T[1 + (e\mathbf{u}_G\mathbf{E}_\parallel)/2A_G^o], \quad A_G^o = \pi\hbar a_o^2\epsilon_b N_G/2mb, \tag{10}$$

where $\mathbf{u}_G$ is given by (8).

The quasistatic mobility μ_g of electrons for the CRIC effect arises from a calculation of the impedance of the Corbino disks (*a*, *b*, and *c* in the figure) upon applying, between them, a small potential difference $\tilde{U}$ oscillating with a frequency Ω, this impedance being sensitive to the state of the 2*D* electron system in question. An analytic solution to this problem has not yet been obtained. In performing absolute measurements of the mobility, one has to employ, for the impedance, the numerical results obtained in [16]. As to the relative measurements reported in [3], it is sufficient in that case to calculate the ohmic quasi-static electron mobility by using the Maxwellian symmetric part of the distribution function in (9) and (10). This mobility is given by formula (1), which is independent of T_e.

In the case of the electron–ripplon interaction (which can also affect CRIC)

$$V_\perp = e\mathbf{E}_\perp\xi(r) \tag{11}$$

with $\xi(r)$ having the meaning of the ripplon amplitude, the required solution to the kinetic equation is given by (3), (7), and (9), with the functions involved being

$$\tau_\perp^{-1} = \frac{m}{2\pi\hbar}\int_0^{2\pi} d\varphi|V_q|^2(2N_q + 1)(1 - \cos\varphi) \simeq \frac{mT}{2\alpha\hbar p^2}e^2E_\perp^2, \tag{12}$$

$$A_\perp(p) = \frac{m}{4\pi\hbar}\int_0^{2\pi} d\varphi\left(\frac{m\hbar\omega_q}{p}\right)|V_q|^2(2N_q + 1) \simeq \frac{2m^3Te^2E_\perp^2}{\pi\hbar^2\rho p}, \tag{13}$$

$$q = 2\frac{p}{\hbar}\sin(\varphi/2), \quad V_q = \int_0^\infty dz_1\psi_1^2(z)V_q(z),$$

$$V_q(z) = Q_q eE_\perp, \quad Q_q = (\hbar qth(qd)/2\rho\omega_q)^{1/2}, \quad N_q \simeq T/\hbar\omega_q, \quad \omega_q^2 \simeq \alpha q^3/\rho.$$

Here, T is the temperature of helium; α and ρ are its surface tension and density, respectively; $\psi(z)$ is the z component of the electron wave function; and ω_q is the ripplon spectrum.

Obviously, the function $f_o(p)$ (9), with $\tau_\perp$ and $A_\perp(p)$ being given by (12) and (13), respectively, is not Max-

wellian; therefore, it is impossible here to introduce an effective electron temperature. If one nevertheless adopts this qualitative simplification, the quasi-static electron mobility corresponding to the interaction in (11) in the region $T_e > T$ proves to be [15]

$$\mu_\perp = \frac{8\alpha\hbar}{meE_\perp^2}(T_e/T). \tag{14}$$

The magnetomobility of electrons characterized by $\mu_\perp$ from (14) decreases with increasing T_e; that is, its behavior is inverse to that which was observed experimentally in [3].

3. Having exhausted the possibilities for explaining the photosensitivity of a 2*D* electron system on helium in terms of relaxation mechanisms (we mean here the electron-temperature dependence of the electron mobility), we now consider alternative scenarios. As was indicated above, one of these may be associated with a nonuniformity of the distribution of the exciting high-frequency field along the 2*D* system being considered. In the scheme of the cell, the high-frequency field of amplitude $E_\parallel$ penetrates to the charged surface of helium in a region of radius $L < S$ and heats it to the temperature T_e (10) (for the sake of simplicity, the heat flux along the surface of helium is disregarded, in which case the electron temperature (10) becomes a local function of $E_\parallel$). Under steady-state conditions, a nonuniform heating of a conductor is accompanied by the emergence of a thermoelectric power and, hence, by a redistribution of the electron density, δn_s, between the central part of the 2*D* system with a radius L and its periphery (up to a radius of $S > R$). It only remains to note that the measuring part of the cell (electrodes *a*, *b*, and *c* in the figure) is localized in the central region and is therefore sensitive to local changes in the electron density.

A formal estimate of δn_s follows from the requirement that the nonuniform excited state of the 2*D* system be stationary. For the problem where the electron density n_s is low and where the electron temperature T_e has the value given by (10), this condition reduces to the requirement that the quasi-electrochemical potential be constant along the conductor (see [12, 17]). In the case being considered, this is the condition

$$\mu = e\varphi + \zeta = \text{const}, \quad \zeta = -T_e\ln(1/\nu), \qquad \nu = \pi l_H^2 n_s \ll 1, \tag{15}$$

where l_H is the magnetic length.

The growth of the electron temperature reduces the potential ζ (15); therefore, the general requirement that the electrochemical potential remain constant along the charged surface of helium will be accompanied by a growth of the electron density in the region of an elevated electron temperature, and this is what was necessary to prove from the point of view of the sign of the effect observed in [3] (see comments to formula (2)).

Assuming that the electrostatic problem of the perturbation $\delta n(x)$ is time-independent and one-dimensional (rather than cylindrically symmetric, as is the case in the figure), we can easily find the explicit form of $\delta n(x)$. The result is

$$\frac{e\delta n(x)d}{|\delta\xi_o|} = \frac{1}{4\pi} + \frac{1}{2\pi}\left[\frac{\exp(-\pi x/d)}{\exp(+\pi w/d) - \exp(-\pi x/d)} + \frac{\exp(+\pi x/d)}{\exp(+\pi w/d) - \exp(+\pi x/d)}\right],$$

$$|\delta\zeta_o| = (T_e - T)\ln 1/\nu_o), \quad \nu_o = \pi l_H^2 n_s^o, \tag{16}$$

where d is the helium-film thickness, $L \longrightarrow 2w$, and $S \longrightarrow \infty$.

For $d/w \gg 1$, expression (16) reduces to

$$\delta n(x) \propto \frac{w}{w^2 - x^2}. \tag{16a}$$

In the opposite limiting case of $d \ll w$, the contribution of the second term on the right-hand side of (16) far off the points $x = \pm w$ is exponentially small against the first term, and we have the distribution $\delta n(x)$ typical of the flat-capacitor problem.

It is instructive to note that, in the case of a Maxwellian structure of the symmetric part $f_o(p)$ of the distribution function, the requirements $\partial f_0/\partial t = 0$ and $\partial f_0/\partial r = 0$ on the nonhomogeneous equation (4) are equivalent to the condition in (15) (see, for example, [17]). In this sense, the kinetic formalism described above makes it possible to validate the introduction of the nonequilibrium quasi-electrochemical potential (15). But if there is no separate electron temperature, as is the case when Eqs. (12) and (13) are valid, the requirement that Eq. (4) be time-independent takes the place of the condition in (15).

Yet another interesting comment concerns the amplitude dependence of the CRIC effect. According to (16), we have $\delta n(x) \propto (T_e - T) \propto E_\parallel^2$. It follows that, within the scenario specified by Eq. (2), the photoconductivity must be a linear function of $E_\parallel^2$. At the same time, experimental data reported in [3] are indicative of a nonlinear relationship between $\delta\tilde{\sigma}$ and the power of pumping, the latter being proportional to the square E_o^2 of the exciting field (according to Fig. 2b from [3], $\delta\tilde{\sigma} \propto \ln E_o^2$). The last two statements are compatible if the quantities $E_\parallel^2$ and E_o^2 are not identical, and this is indeed so. Since the main objective here is to draw only qualitative conclusions, the geometric details of the problem are simplified, at this stage, to the maximum possible degree. Omitting intermediate calculations aimed at determining the coefficient R of reflection of a high-frequency signal from the resonator in the figure in the presence of 2*D* electrons, we only quote the even-

tual result for the field $E_{\|}$ in terms of R and E_o. Its specific form is

$$E_{\|} = E_o(1-R)\sin(kd)/f(kh, kd, \sigma), \quad (17)$$

$$R = \frac{\gamma - i}{\gamma + i}, \quad (18)$$

$$\gamma = \sigma_m + \frac{\cos(kh) + \sigma\sin(kd)\cos k(h-d)}{f(kh, kd, \sigma)},$$

$$f(kh, kd, \sigma) = \sin(kh) - i\sigma\sin(kd)$$
$$\times [\sin(kd)\cos(kh) - \cos(kd)\sin(kh)],$$

$$\sigma = 4\pi\sigma_{xx}/c, \quad k = \omega/c,$$

where σ_m is the effective conductivity of the mesh covering the inlet of the waveguide in the figure and the function $f(kh, kd, \sigma)$ determines the resonance properties of the cell in the figure for the case where this cell contains electrons. The vanishing of this function,

$$f(kh, kd, \sigma) = 0, \quad (19)$$

determines the eigenfrequencies of the resonator containing electrons. It is obvious that, for $\sigma_m \longrightarrow \infty$, the reflection factor in (18) tends to unity. At finite values of σ_m, the quantity R begins to feel the properties of the resonator. In particular, we have

$$R_o = \frac{\gamma_o - i}{\gamma_o + i}, \quad \gamma_o = \sigma_m + \cot(kh) \quad (20)$$

for an empty resonator, in which case $\sigma_{xx} \longrightarrow 0$. If, in addition, the external frequency satisfies the requirement

$$\sin(k_o h) \longrightarrow 0, \quad (21)$$

then

$$R_o \longrightarrow 1 \quad (22)$$

even in the case of a limited conductivity of the mesh (the total reflection of the external signal occurs at the lower plate of the resonator).

Returning to the relationship in (17), we recall the conditions prevalent in the experiment reported in [3]. Fixing the frequency ω and varying the magnetic-field strength, one can find an extremum of R at a minimum level of pumping (the function $f(kh, kd, \sigma)$ is resonantly small here). After that, this tuning is preserved, with only the level of pumping being changed. It is clear that, as T_e is increased, which is naturally accompanied by an increase in the scale of the thermoelectric power between the center and the periphery of the electron disk, the conductivity of the central part of the disk grows. This entails a sharp change in the function $f(kh, kd, \sigma)$ toward greater values (shift to an off-resonance region). It follows that, with an increased level of pumping, the amplitude $E_{\|}$ from (17) grows more slowly than E_o, and this is what one observes experimentally.

In summary, various scenarios of the emergence of the classical CRIC effect have been discussed in the present study for electrons on helium. A CRIC mechanism has been proposed that takes into account the presence of a thermoelectric power in a nonuniformly heated $2D$ electron disk. This thermal scenario provides a qualitatively correct explanation of the sign and scale of the photoconductivity observed experimentally in [3].

This work was supported in part by the Russian Foundation for Basic Research (project no. 030216121).

REFERENCES

1. H. Bluyssen, J. Mann, L. Ruyven, *et al.*, Solid State Commun. **25**, 895 (1978).
2. J. Mann, T. Englert, D. Tsui, and A. Gossard, Appl. Phys. Lett. **40**, 609 (1982).
3. F. Penning, O. Tress, H. Bluyssen, and P. Wyder, J. Low Temp. Phys. **110**, 185 (1998).
4. F. Penning, O. Tress, H. Bluyssen, *et al.*, Phys. Rev. B **61**, 4530 (2000).
5. M. Zudov, R. Du, J. Simmons, and J. Reno, cond-mat/9711149 (1997).
6. M. Zudov, R. Du, J. Simmons, and J. Reno, Phys. Rev. B **64**, 201311 (2001).
7. M. Zudov, R. Du, L. Pfeifer, and K. West, cond-mat/0210034 (2002).
8. R. Mani, J. Smet, K. von Klitzing, *et al.*, Nature **420**, 646 (2002).
9. M. Zudov, R. Du, L. Pfeiffer, and K. West, Phys. Rev. Lett. **90**, 046807 (2003).
10. A. Durst, S. Sachdev, N. Read, and S. Girvin, cond-mat/0301569.
11. A. Andreev, I. Aleiner, and J. Mils, cond-mat/0302063.
12. L. D. Landau and E. M. Lifshitz, *Course of Theoretical Physics*, Vol. 8: *Electrodynamics of Continuous Media*, 2nd ed. (Nauka, Moscow, 1982; Pergamon Press, Oxford, 1984).
13. B. Davydov, Zh. Éksp. Teor. Fiz. **7**, 1070 (1937).
14. M. Saitoh, J. Phys. Soc. Jpn. **44**, 71 (1978).
15. V. B. Shikin and Yu. P. Monarkha, *Two-Dimensional Charged Systems in Helium* (Nauka, Moscow, 1989).
16. L. Willen and R. Gianetta, J. Low Temp. Phys. **72**, 353 (1988).
17. V. L. Bonch-Bruevich and S. G. Kalashnikov, *Physics of Semiconductors* (Nauka, Moscow, 1977).

Translated by A. Isaakyan

JETP Letters, Vol. 78, No. 5, 2003, pp. 319–321. Translated from Pis'ma v Zhurnal Éksperimental'noĭ i Teoreticheskoĭ Fiziki, Vol. 78, No. 5, 2003, pp. 768–771.

Supersensitive Electronic Transition in Impurity Nd–Nd Nanoclusters in CaF_2 Crystal

T. T. Basiev, A. Ya. Karasik*, A. A. Kornienko, A. G. Papashvili, and K. K. Pukhov

Laser Materials and Technologies Research Center of General Physics Institute, Russian Academy of Sciences, Moscow, 119991 Russia

**e-mail: karasik@lst.gpi.ru*

Received July 28, 2003

A comparison of the theoretical calculations with the results of experiments on high-resolution laser spectroscopy made it possible to reveal the fine structure that arises in the supersensitive $^4I_{9/2} \longleftrightarrow {}^4G_{5/2}$ transition as a result of a strong coherent interaction in the Nd^{3+} ion pair in the CaF_2 crystal and construct the level splitting diagram for the ground and excited states of impurity Nd–Nd nanoclusters. *© 2003 MAIK "Nauka/Interperiodica".*

PACS numbers: 73.21.-b; 61.72.Ss

It is well known that some electronic transitions of trivalent rare-earth (RE) ions are supersensitive to the surrounding ligand field [1]. Two mechanisms were proposed to explain the supersensitivity of these transitions. (1) The inhomogeneity of dielectric environment of the RE ions can sizably increase the transition intensity ("inhomogeneous" dielectric mechanism) [2]; (2) the dynamic interaction of 4*f* electrons with ligands [1–5] polarizes the latter, which then interact with the radiation field. Later on, it was shown [6, 7] that both these mechanisms are identical.

In this work, we examine the supersensitive Nd^{3+} $^4I_{9/2} \longleftrightarrow {}^4G_{5/2}$ transition. We first consider the theoretical aspects of the problem and estimate the most important parameters of the transition in CaF_2, where the Nd^{3+} ions are clustering into two- and four-particle aggregates with subnanometer distances between the trivalent impurity ions [8]. Due to the strong coherent interaction between the Nd^{3+} ions, the ground and excited states of the indicated transition are split into sublevels with gaps between them ranging from hundredths to several cm^{-1} [9–11]. We will compare the theoretical estimates with the results of high-resolution laser spectroscopy to reveal the fine-splitting structure and construct the level-splitting diagram for the ground and excited states of the Nd–Nd dimer. These studies are of importance from both fundamental and applied points of view and, in particular, for the discussion of the prospects of using inorganic crystals containing impurity RE ions as optical memory cells and elements of quantum computational devices.

Theoretical. Following the model [6], we consider the contribution of dynamic interaction to the intensity of the supersensitive Nd^{3+} $^4I_{9/2} \longleftrightarrow {}^4G_{5/2}$ transition. The electric vector **E** of the radiation field induces dipole moment $\alpha\mathbf{E}$ in a ligand situated at the distance R from the RE nucleus (α is assumed to be the polarizability of a spherically symmetric ligand). The dipole moment $\alpha\mathbf{E}$ produces the potential

$$V = -\alpha\mathbf{E}(\mathbf{r} - \xi)|R - \xi|^{-3} \quad (1)$$

at the position ξ of the 4*f* electron. It follows from [6] that the potential V increases the electronic dipole moment by

$$\mathbf{D} = \sum_s \sum_a \alpha_s (R_s - \xi_a)|R_s - \xi_a|^{-3}. \quad (2)$$

Following Judd, we write the Judd–Ofelt parameter Ω_2 for the dipolar interaction as

$$\Omega_2 = \frac{28}{15} \sum_{s,\,s'} \alpha_s \alpha_{s'} \frac{\langle \xi^2 \rangle^2}{R_s^4 R_{s'}^4} P_3(\mathbf{n}_s \mathbf{n}_{s'}). \quad (3)$$

Here, $\langle \xi^2 \rangle$ is the mean square 4*f*-electron radius averaged over the 4*f* wave function, R_s is the equilibrium distance between the RE ion and the *s*th ligand, $n_s = R_s/R_s$, and $P_k(z)$ is the Legendre polynomial.

Let us estimate the parameter Ω_2 for a CaF_2:M center composed of a pair of Nd^{3+} ions that substitute for a pair of Ca^{2+} ions situated in two neighboring sites of the cationic sublattice and arranged in the crystallographic $\langle 110 \rangle$ direction. The separation $R(Nd^{3+}–Nd^{3+})$ between the ions in the pair is 0.385 nm. The excess positive charges arising upon substituting Nd^{3+} for Ca^{2+} are compensated by a pair of negatively charged fluorine ions situated in the neighboring interstitial sites. The crystal field of the resulting M cluster has orthorhombic symmetry [8]. Assume that the polarizability α of the interstitial F^- ions coincides with the polarizability of

the ions in the lattice sites. Due to the inversion symmetry, eight lattice F^- ions make no contribution to Ω_2, while the contribution from the two neighboring interstitial F^- ions is

$$\Omega_2 = \frac{56}{5}\frac{\langle\xi^2\rangle^2}{(a/2)^8}\alpha_F^2. \quad (4)$$

Here, a is the lattice constant and α_F is the polarizability of the F^- ion. Note that Eq. (4) has the same form for any MeF_2 (Me = Ca, Sr, etc.) crystal. Using the values $\langle\xi^2\rangle = 1.001$ a.u. [12], $a = 0.546$ nm [13], and $\alpha_F = 0.87$ Å$^3 = 0.87 \times 10^{-30}$ m^3 [14], one gets $\Omega_2 = 2.19 \times 10^{-20}$ cm^2.

Let us now use the matrix element $|({}^4I_{9/2}\|U^{(2)}\|{}^4G_{5/2})|^2 = 0.8779$ [15] to calculate the transition line strength caused by the dynamic interaction mechanism:

$$S_{th}({}^4I_{9/2}, {}^4G_{5/2}) = \Omega_2\left|(4I_{9/2}\left\|U^{(2)}\right\|{}^4G_{5/2})\right|^2$$
$$= 1.92 \times 10^{-20}\text{cm}^2.$$

Using the expression

$$\sigma_{abs}(J \longrightarrow J') = \frac{4\pi^2}{3}\frac{e^2}{\hbar c}\frac{(n^2+2)^2}{9n}E\frac{S(J,J')}{2J+1}, \quad (5)$$

where e is the electron charge, c is the velocity of light in vacuum, $n = 1.43$ is the refractive index, $E = 17255$ cm^{-1} is the energy of the excited ${}^4G_{5/2}$ state, and $J = 9/2$, the above theoretical estimate of the line strength can be compared with the value obtained from the experimentally measured integrated cross section for the ${}^4I_{9/2} \longleftrightarrow {}^4G_{5/2}$ transition. This cross section was determined from the absorption spectrum of the CaF_2:Nd^{3+} (0.3 wt %) crystal obtained at 9 K [9] for the transition between the lowest sublevels of the ground (${}^4I_{9/2}$) and excited (${}^4G_{5/2}$) Stark manifolds. With allowance for the EPR-based concentration of M centers $N = 1.44 \times 10^{18}$ cm^{-3} [16], we find that $\sigma_{abs}(J - J') = 1.32 \times 10^{-18}$ cm. As a result, the value obtained from Eq. (5) coincides, to a good accuracy, with the experimentally measured line strength $S_{\text{exp}}({}^4I_{9/2}, {}^4G_{5/2}) = 1.87 \times 10^{-20}$ cm^2. However, it was pointed out in [6] that one should, generally, introduce the factor $(1 - \sigma_2)^2$ into Eq. (3) to correct for a quadrupole field that is screened by the outer electronic shells. At present, the corresponding data are not available. Moreover, it follows from the discussion in [6, 7] that it is even unclear how this parameter changes upon the transition from the static to the dynamic field.

To construct the level-splitting diagram, one should take into account the character of splitting and the selection rules for the dynamic interaction model of intraconfiguration transitions of the M center. The lowest sublevel of the ${}^4I_{9/2} \times {}^4I_{9/2}$ Stark manifold of a noninteracting pair of Kramers' Nd ions is fourfold degenerate. Due to the spin–spin magnetic dipole–dipole and exchange interactions, this level splits into the triplet ($\chi(T_+)$, $\chi(T_-)$, and $\chi(T_0)$) and singlet ($\chi(S)$) states [10]. The electrostatic (mainly quadrupole–quadrupole) interaction of the supersensitive optical transition in the ion pair generally removes the eightfold degeneracy of the excited ${}^4I_{9/2} \times {}^4G_{5/2}$ level, resulting in the splitting of this transition into the maximum possible number of lines $4 \times 8 = 32$ [10]. The expressions for the zero-order wave functions Ψ_i ($i = 1, 2, \ldots, 8$) and the corresponding eigenvalues $E_i = E_0 + \Delta_i$ of the excited ${}^4I_{9/2} \times {}^4G_{5/2}$ level are given in [10]. This level splits in such a way that the energy distances Δ_i from the center-of-gravity of the resulting manifold are related by $\Delta_5 = -\Delta_1$, $\Delta_6 = -\Delta_2$, $\Delta_7 = -\Delta_3$, and $\Delta_8 = -\Delta_4$. In the dynamical coupling model, the interaction of f electrons with the radiation field can be written for the M center as

$$H = -\mathbf{E}(D_a + D_b), \quad (6)$$

where D_a and D_b are given by Eq. (2) for ions a and b. The ground-level triplet states of the ${}^4I_{9/2} \times {}^4I_{9/2}$ pair are symmetric, while the singlet state is antisymmetric with respect to the permutation of ions $a \Leftrightarrow b$. For the interaction (6), the transitions between the symmetric triplet and excited symmetric Ψ_1, Ψ_2, Ψ_3, and Ψ_4 states of the Nd–Nd pair are forbidden. Likewise, the transitions between the antisymmetric singlet and the antisymmetric Ψ_5, Ψ_6, Ψ_7, and Ψ_8 states are also forbidden. These selection rules are analogous to the rules considered in our work [10] for the induced electric dipole transitions in the model of Nd^{3+}–Nd^{3+}-pair interaction in CaF_2. Note that the selection rules for the magnetic dipole and electric quadrupole transitions are quite the reverse. The transitions between the symmetric states, as also the transitions between the antisymmetric states, are allowed, whereas the transitions between the symmetric and antisymmetric states are forbidden.

For the transitions caused by the dynamic coupling mechanism (DCM), additional selection rules appear (the $S \longrightarrow \Psi_4$ and $T_0 \longrightarrow \Psi_5$ transitions are forbidden). However, these rules are strict if one takes into account only the contribution from the compensating interstitial F^- ions. If the F^- ions in the nearest surrounding of the Nd^{3+} ions of M center are shifted from their equilibrium positions, the selection rules become the same as for the electric dipole transitions (see [10]).

Energy level diagram. The CaF_2:NdF_3 (0.04 wt %) ${}^4I_{9/2} \longrightarrow {}^4G_{5/2}$ excitation spectrum recorded at 10 K (luminescence was recorded for the ${}^4F_{3/2} \longrightarrow {}^4I_{9/2}$ transition) by a laser spectrometer based on a tunable nanosecond $LiF : F_2^-$ laser is shown in the figure. The laser cavity with a diffraction grating set at the grazing incidence regime allowed tunable oscillation in the ranges 1090–1230 and 545–615 nm with a spectral width of ~0.03 cm^{-1}. The linewidths of 0.1–0.2 cm^{-1} in the excitation spectrum correspond to the inhomogeneous

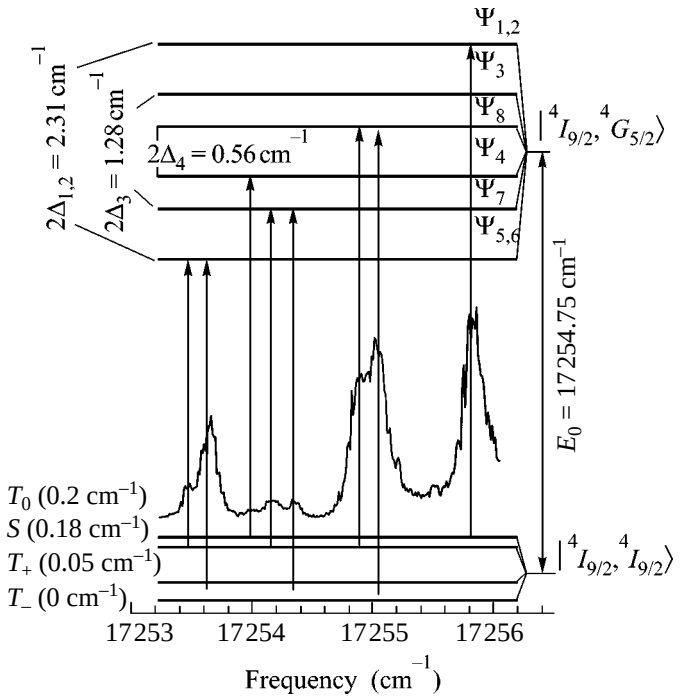

Luminescence excitation spectrum of the CaF_2:NaF_3 (0.04 wt %) crystal at 10 K and the energy level scheme of Nd^{3+} ion pairs for the supersensitive $^4I_{9/2} \longrightarrow {}^4G_{5/2}$ transition. Arrows indicate the spectral lines corresponding to the allowed transitions between the singlet (S) and triplet (T) ground- and excited-state (Ψ) levels split due to the strong coherent interaction in the ion pair.

broadening, while the homogeneous width of these lines, as obtained by the method of picosecond accumulated photon echo (APE) [9], was much smaller at 10 K (0.0017 cm^{-1}). The analysis of the spectrum and the above considerations made it possible to construct an energy level diagram for the Nd-ion pair with strong coherent interaction (figure). When constructing the diagram, the APE results [9] were taken into account. In the APE experiments, the interference of the transitions between the split ground-state singlet–triplet sublevels and the excited-state Ψ sublevels brings about temporal echo-signal beats with a period of tens and hundreds of picoseconds. The splittings of the excited Ψ_i (1–2.3 cm^{-1}) and singlet–triplet (0.05–0.2 cm^{-1}) levels are shown in the figure and correlate well with the experimentally observed APE beats.

Note that the ground-level splitting into triplet sublevels with energies $E(T_-) = 0$, $E(T_+) = 0.05$ cm^{-1}, and $E(T_0) = 0.2$ cm^{-1} (figure) is in agreement with the EPR data [17]. The EPR technique is incapable of determining the position of singlet level because of the forbiddenness of the singlet–triplet spin–spin transitions, whereas the same transitions are observed in the APE temporal beats [9, 10]. The position of the singlet level E(S) (figure) was determined by using the excitation spectrum and the APE data. We failed to determine the splitting of the excited Ψ_1, Ψ_2, Ψ_5, and Ψ_6 levels with accuracy better than the spectrometer resolution (0.03 cm^{-1}), probably, because of spectrum inhomogeneous broadening or level degeneracy.

Note in conclusion that the theoretical analysis presented above and high-resolution laser spectroscopy, in conjunction with photon echo and EPR spectroscopies, allowed us to construct a splitting diagram for the supersensitive transition of the Nd^{3+}–Nd^{3+} pair in CaF_2 crystal.

REFERENCES

1. R. D. Peacock, Struct. Bonding (Berlin) **22**, 43 (1975).
2. C. K. Jorgensen and B. R. Judd, Mol. Phys. **8**, 281 (1964).
3. S. F. Mason, R. D. Peacock, and B. Stewart, Chem. Phys. Lett. **29**, 149 (1974).
4. S. F. Mason, R. D. Peacock, and B. Stewart, Mol. Phys. **30**, 1829 (1975).
5. T. R. Faulkner and F. S. Richardson, Mol. Phys. **35**, 1141 (1978).
6. B. R. Judd, J. Chem. Phys. **70**, 4830 (1979).
7. B. R. Judd, Phys. Scr. **21**, 543 (1979).
8. V. V. Osiko, Yu. K. Voron'ko, and A. A. Sobol, *Crystals* (Springer, Berlin, 1984), Vol. 10.
9. T. T. Basiev, A. Ya. Karasik, V. V. Fedorov, *et al.*, Zh. Éksp. Teor. Fiz. **113**, 278 (1998) [JETP **86**, 156 (1998)].
10. T. T. Basiev, V. V. Fedorov, A. Ya. Karasik, *et al.*, J. Lumin. **81**, 189 (1999).
11. V. V. Fedorov, T. T. Basiev, A. Ya. Karasik, *et al.*, Chem. Phys. **257**, 275 (2000).
12. A. J. Freeman and R. E. Watson, Phys. Rev. **127**, 2058 (1962).
13. *Acoustical Crystals*, Ed. by M. P. Shaskol'skaya (Nauka, Moscow, 1982).
14. C. Kittel, *Introduction to Solid States Physics*, 5th ed. (Wiley, New York, 1976; Fizmatlit, Moscow, 1963).
15. W. T. Carnall, P. R. Fields, and K. Rajnak, J. Chem. Phys. **49**, 4424 (1968).
16. T. T. Basiev, V. V. Fedorov, Yu. V. Orlovskii, *et al.*, in *Abstracts of XI Feofilov Symposium on Spectroscopy of Crystals Activated by Rare Earth Ions, 2001*, PF-18.
17. N. E. Kask, L. S. Kornienko, and E. G. Lariontsev, Fiz. Tverd. Tela (Leningrad) **8**, 2572 (1966) [Sov. Phys. Solid State **8**, 2058 (1966)].

Translated by V. Sakun

JETP Letters, Vol. 78, No. 5, 2003, pp. 322–326. Translated from Pis'ma v Zhurnal Éksperimental'noĭ i Teoreticheskoĭ Fiziki, Vol. 78, No. 5, 2003, pp. 772–776.

Spin Waves in Layered Conductors

V. G. Peschansky* and D. I. Stepanenko

Verkin Physicotechnical Institute of Low Temperatures, National Academy of Sciences of Ukraine, Kharkov, 61164 Ukraine

**e-mail: vpeschansky@itl.kharkov.ua*

Received July 28, 2003

The spectrum of spin waves propagating in layered conductors with a quasi-bidimensional law of charge carrier dispersion was determined for the case of an arbitrary correlation function and an external magnetic field perpendicular to the conducting layers. © *2003 MAIK "Nauka/Interperiodica"*.

PACS numbers: 75.30.Ds; 75.40.Gb

A wide class of layered structures with metallic conduction and strong anisotropy of the kinetic coefficients are currently known. This class includes organic conductors belonging to the family of tetrathiafulvalene salts, transition-metal dichalcogenides, graphite intercalated with various elements, etc. Experimental studies of the galvanomagnetic properties of such substances (in particular, observation of the Shubnikov–de Haas oscillations [1, 2]) showed that their kinetic and electrodynamic properties at low temperatures could be described using the concept of a system of quasiparticles similar to the conduction electrons in normal metals, but having a strongly anisotropic energy spectrum. In layered conductors, the charge carrier-energy depends only slightly on the momentum projection $p_z = \mathbf{pn}$ onto the normal $\mathbf{n}$ to the layers. The carrier energy can be described with a rapidly converging power series in the quasi-bidimensionality parameter η:

$$\varepsilon(\mathbf{p}) = \varepsilon_0(p_x, p_y) + \sum_{n=1}^{\infty} \varepsilon_n(p_x, p_y, \eta)\cos\left(\frac{np_z}{p_0}\right), \quad (1)$$

where $\varepsilon_n(p_x, p_y, \eta) \sim O(\eta\varepsilon_F)$, $\varepsilon_{n+1}(p_x, p_y, \eta) \ll \varepsilon_n(p_x, p_y, \eta)$, ε_F is the Fermi energy, $p_0 = \hbar/a$, $\hbar$ is the Planck's constant, and a is the interlayer distance. The parameter η is a measure of the energy spectrum anisotropy. Its square is equal to the ratio of the electrical conductions along and across the layers to a factor of the order of unity. The numerical value of the parameter η squared ranges from 10^3 to 10^5.

Different underdamped collective Bose modes, such as magnetohydrodynamic and cyclotron waves, can be generated in normal metals exposed to a strong magnetic field and a low temperature. The majority of these modes have their analogues in gas plasma. However, spin waves, which were predicted by Silin [3] and experimentally discovered by Schultz and Dunifer [4], are typical only for the conduction-electron plasma. There is a considerable literature on the subject of spin waves in quasi-isotropic metals without any magnetic order (see, for example, [5] and references therein for a review). In this work, we measured the spin wave spectrum in layered conductors exposed to a constant magnetic field perpendicular to the conducting layers (*xy* plane). The interaction between the charge carriers in a conducting layer is considerably stronger than the interaction between the quasiparticles belonging to different layers. Therefore, not only the energy in the single-electron approximation (1), but also the Landau correlation function can be expanded in an asymptotic power series of η, with the first asymptotic term independent of p_z. This assumption considerably simplifies the equations involved in the problem and makes it possible to solve them for a quite general form of correlation function.

The kinetic properties of a fermion system exposed to an electromagnetic field are described by an equation for the density matrix and a set of Maxwell equations. Let us consider the case of $\hbar\omega_B \lesssim T \ll \eta\varepsilon_F$ (ω_B is the cyclotron frequency of the conduction electrons and T is the temperature), when the quantization of the charge-carrier energy levels has only slight effect on the magnetization M. Under these conditions, the density matrix can be considered as an operator in the space of spin variables and as a quasi-classical coordinate- and momentum-dependent function. The additional energy of a quasiparticle caused by the electron–electron interaction effects

$$\delta\hat{\varepsilon}(\mathbf{p}, \mathbf{r}, t) = \mathrm{Sp}_{\sigma'}\int \frac{d^3p'}{(2\pi\hbar)^3} L(\mathbf{p}, \hat{\boldsymbol{\sigma}}, \mathbf{p}', \hat{\boldsymbol{\sigma}}')\delta\hat{\rho}(\mathbf{p}', \mathbf{r}, \hat{\boldsymbol{\sigma}}', t) \quad (2)$$

is determined, in the framework of the Landau–Silin theory of Fermi liquid [6, 7], by the correlation function

$$L(\mathbf{p}, \hat{\boldsymbol{\sigma}}, \mathbf{p}', \hat{\boldsymbol{\sigma}}') = N(\mathbf{p}, \mathbf{p}') + S(\mathbf{p}, \mathbf{p}')\hat{\boldsymbol{\sigma}}\hat{\boldsymbol{\sigma}}',$$

where $\delta\hat{\rho}$ is the non-equilibrium addition to the density matrix and $\hat{\boldsymbol{\sigma}}$ are the Pauli matrices. To a zero approximation in the small parameter η, the functions $N(\mathbf{p}, \mathbf{p}')$ and $S(\mathbf{p}, \mathbf{p}')$ do not depend on p_z and can be represented as the series

$$N(\mathbf{p}, \mathbf{p}') = \sum_{n=-\infty}^{\infty} N_n(\varepsilon_F) e^{in(\varphi-\varphi')},$$
$$S(\mathbf{p}, \mathbf{p}') = \sum_{n=-\infty}^{\infty} S_n(\varepsilon_F) e^{in(\varphi-\varphi')}. \quad (3)$$

The integrals ε and p_z of the charge-carrier motion in a magnetic field and the electron velocity phase $\varphi = \omega_B t_1$ (t_1 is the time of motion along the trajectory $\varepsilon = \varepsilon_F$, p_z = const) were selected as the variables in the $\mathbf{p}$ space. Because $L(\mathbf{p}, \hat{\boldsymbol{\sigma}}, \mathbf{p}', \hat{\boldsymbol{\sigma}}')$ is symmetric with respect to the permutation of its argument, the coefficients in Eqs. (3) are related to one another as $N_{-n} = N_n$ and $S_{-n} = S_n$. Only minor corrections to the kinetic coefficients can be obtained by taking into account the next terms of expansion of the correlation function in terms of η.

The distribution function $f(\mathbf{r}, \mathbf{p}, t) = \mathrm{Sp}_\sigma\hat{\rho}$ and the spin density $\mathbf{g}(\mathbf{r}, \mathbf{p}, t) = \mathrm{Sp}_\sigma(\hat{\boldsymbol{\sigma}}\hat{\rho})$ can conveniently be used instead of the density matrix $\hat{\rho}$. For small deviations from the equilibrium state, the function $\mathbf{g}$ can be represented as the sum of the equilibrium component $\mathbf{g}_0(\varepsilon) = -\mu\mathbf{B}_0(\partial f_0/\partial\varepsilon)$ and a minor non-equilibrium addition $-\boldsymbol{\xi}(\mathbf{r}, \mathbf{p}, t)(\partial f_0/\partial\varepsilon)$, where $f_0(\varepsilon)$ is the Fermi function, $\mu = \mu_0/(1 + S_0^{\sim})$, μ_0 is the magnetic moment of a conduction electron, $S_0^{\sim} = \nu(\varepsilon_F)S_0$, and $\nu(\varepsilon_F)$ is the density of states at the Fermi level. The integral of $\mu_0\mathbf{g}_0(\varepsilon)$ over a unit cell of the $\mathbf{p}$ space is equal to the magnetization $\mathbf{M}_0 = \chi_0\mathbf{B}_0$ in a uniform magnetic field with induction $\mathbf{B}_0 = (0, 0, B_0)$; $\chi_0 = \mu_0\mu\nu(\varepsilon_F)$ is the static paramagnetic susceptibility.

According to [3], if the spin density disturbance $\boldsymbol{\xi}$ is perpendicular to $\mathbf{B}_0$, the linearized kinetic equation takes the form

$$\frac{\partial\boldsymbol{\xi}}{\partial t} + \left(\mathbf{v}\frac{\partial}{\partial\mathbf{r}} + \frac{e}{c}(\mathbf{v}\times\mathbf{B}_0)\frac{\partial}{\partial\mathbf{p}}\right)$$
$$\times(\boldsymbol{\xi} + \langle S\boldsymbol{\xi}\rangle) - \frac{2\mu}{\hbar}[\mathbf{B}_0\times(\boldsymbol{\xi} + \langle S\boldsymbol{\xi}\rangle)] \quad (4)$$
$$-\mu_0\mathbf{v}\frac{\partial\mathbf{B}^{\sim}}{\partial\mathbf{r}} + \frac{2\mu\mu_0}{\hbar}[\mathbf{B}_0\times\mathbf{B}^{\sim}] = \hat{I}_{\mathrm{coll}},$$

where

$$\langle S\boldsymbol{\xi}\rangle = \int\frac{2d^3p'}{(2\pi\hbar)^3}\left(-\frac{\partial f_0(\varepsilon')}{\partial\varepsilon'}\right)S(\mathbf{p}, \mathbf{p}')\boldsymbol{\xi}(\mathbf{r}, \mathbf{p}', t),$$

e is the electron charge, $\mathbf{v} = \partial\varepsilon(\mathbf{p})/\partial\mathbf{p}$ is the electron velocity, c is the velocity of light, and $\mathbf{B} = \mathbf{B}_0 + \mathbf{B}^{\sim}(r, t)$, where $\mathbf{B}^{\sim}(r, t)$ is the high-frequency field. The collision integral $\hat{I}_{\mathrm{coll}}$ determines two characteristic relaxation times: momentum randomization time τ_1 and spin-density relaxation time τ_2. In the subsequent discussion, we consider the processes in a frequency range

$$kc \gg \omega \gg \tau^{-1} = \tau_1^{-1} + \tau_2^{-1},$$

where the asymptotic behavior of the spectrum of collective modes is independent of the specific form of collision integral; $\mathbf{k} = (k_x, 0, k_z)$ is the wave vector. Under these conditions, the Fourier component of the variable magnetic field produced by the spin oscillations is determined by the equation

$$\mathbf{B}^{\sim}(\omega, \mathbf{k}) = 4\pi\left(\mathbf{M}^{\sim}(\omega, \mathbf{k}) - \frac{\mathbf{k}}{k^2}(\mathbf{k}\mathbf{M}^{\sim}(\omega, \mathbf{k}))\right), \quad (5)$$

where $\mathbf{M}^{\sim}(\omega, \mathbf{k}) = \mu_0\langle\boldsymbol{\xi}(\mathbf{p}, \omega, \mathbf{k})\rangle$ is the Fourier component of the high-frequency magnetization.

Expanding the functions $\boldsymbol{\Phi} = \boldsymbol{\xi} + \langle S\boldsymbol{\xi}\rangle$ and $\boldsymbol{\xi}$ into Fourier series in terms of the variable φ and using Eqs. (3), we obtain:

$$\boldsymbol{\xi} = \boldsymbol{\Phi} - \sum_{m=-\infty}^{\infty}\lambda_m\overline{\boldsymbol{\Phi}}_m e^{im\varphi},$$
$$\lambda_m = \frac{S_m^{\sim}}{1 + S_m^{\sim}},$$
$$\overline{\boldsymbol{\Phi}}_m = \frac{1}{(2\pi)^2}\int_0^{2\pi}d\varphi\int_{-\pi}^{\pi}d\theta e^{-im\varphi}\boldsymbol{\Phi}(\varepsilon_F, \theta, \varphi) \quad (6)$$
$$\equiv\langle e^{im\varphi}\Phi\rangle_{\theta,\varphi}, \quad \theta = \frac{p_z}{p_0}.$$

Substituting Eq. (6) into Eq. (4) we find that the components of the renormalized spin density $\Phi^{(\pm)} = \Phi_x \pm i\Phi_y \sim \exp(-i\omega t + i\mathbf{k}\mathbf{r})$ of conduction electrons satisfy the integral equations

$$\Phi^{(\pm)} = \int_{-\infty}^{\varphi}d\varphi'\exp\left(-\frac{i}{\omega_B}\int_{\varphi'}^{\varphi}d\varphi''(\tilde{\omega}\mp\Omega - \mathbf{k}\mathbf{v}(\varphi'', \theta))\right)$$
$$\times\left(i\frac{\mu_0}{\omega_B}(\mathbf{k}\mathbf{v}\pm\Omega)B_{\pm}^{\sim} - i\frac{\omega}{\omega_B}\sum_{p=-\infty}^{\infty}\lambda_p\overline{\Phi}_p^{(\pm)}e^{ip\varphi'}\right), \quad (7)$$

where $\tilde{\omega} = \omega + i0$, $B_{\pm}^{\sim} = B_x \pm iB_y$, $\Omega = \omega_s/(1 + S_0^{\sim})$, and $\omega_s = -2\mu_0B_0/\hbar$ is the spin paramagnetic resonance frequency. Multiplying this equation by $e^{-in\varphi}$ and integrating with respect to $d\theta$ and $d\varphi$, we obtain an infinite set

of linear equations for the coefficients $\overline{\Phi}_n^{(\pm)}$ in the Fourier series expansion of the function $\langle \Phi^{\pm}(\varepsilon_F, p_z, \varphi)\rangle_\theta$:

$$\sum_{p=-\infty}^{\infty}\left(\delta_{np}-\lambda_p\frac{\omega}{\omega_B}\langle f_{np}(\theta)\rangle_\theta\right)\overline{\mathbf{\Phi}}_p^{(\pm)} = \mu_0 B_\pm^{\sim} F_n$$

$$\equiv -\mu_0 B_\pm^{\sim}\left\langle \frac{1}{2\pi i}\frac{\int_0^{2\pi}\int_0^{2\pi} d\varphi d\varphi_1(\mathbf{kv}(\theta,\varphi-\varphi_1)\mp\Omega)\exp(i(p-n)\varphi - ip\varphi_1 + iS(\varphi,\varphi_1))}{1-\exp\left(2\pi i\frac{(\tilde{\omega}-\langle \mathbf{kv}\rangle_\varphi \mp\Omega)}{\omega_B}\right)}\right\rangle_\theta, \quad (8)$$

where

$$f_{np}(\theta) = \frac{1}{2\pi i}\frac{\int_0^{2\pi}\int_0^{2\pi} d\varphi d\varphi_1 \exp(i(p-n)\varphi - ip\varphi_1 + iS(\varphi,\varphi_1))}{1-\exp\left(2\pi i\frac{\tilde{\omega}-\langle \mathbf{kv}\rangle_\varphi\mp\Omega}{\omega_B}\right)}, \quad (9)$$

$$\langle f_{np}(\theta)\rangle_\theta = \frac{1}{2\pi}\int_{-\pi}^{\pi} d\theta f_{np}(\theta) \equiv \bar{f}_{np},\ S(\varphi,\varphi_1) \equiv \frac{1}{\omega_B}\int_{\varphi-\varphi_1}^{\varphi} d\varphi'(\tilde{\omega}\mp\Omega - \mathbf{kv}(\theta,\varphi')),$$

and δ_{np} is the Kronecker delta. This equation makes it possible to determine the magnetic susceptibility

$$\chi_\pm(\omega,\mathbf{k}) \equiv \frac{\partial M_\pm^{\sim}(\omega,\mathbf{k})}{\partial B_\pm^{\sim}} = \mu\nu(\varepsilon_F)\frac{\overline{\mathbf{\Phi}}_0^{(\pm)}(\omega,k)}{B_\pm^{\sim}},$$

which takes into account the spatial and time dispersion:

$$\chi_\pm(\omega,k) = \chi_0\frac{\det\left[\delta_{0p}F_n + \left(\delta_{np}-\lambda_p\frac{\omega}{\omega_B}\langle f_{np}(\theta)\rangle_\theta\right)(1-\delta_{0p})\right]}{\det\left[\delta_{np}-\lambda_p\frac{\omega}{\omega_B}\langle f_{np}(\theta)\rangle_\theta\right]}. \quad (10)$$

The set of equations (5) and (10) describes the natural oscillations of the electromagnetic field caused by the spin-density oscillations in layered conductors with an arbitrary energy spectrum and correlation function. The Fourier coefficients of the smooth function $\nu(\varepsilon_F)S(\mathbf{p}, \mathbf{p}')$ decrease rapidly as their number increases. Therefore, the series in Eq. (8) can be truncated to a finite number of terms.

Let us omit the small inhomogeneous term proportional to $\mu_0 B_\pm^{\sim}$ in Eq. (8) and designate the solution of the obtained homogeneous equation as ϕ. The dispersion equation for the free oscillations of spin density ϕ is written as

$$D(\omega^{(0)},\mathbf{k}) \equiv \det\left[\delta_{np}-\lambda_p\frac{\omega^{(0)}}{\omega_B}\langle f_{np}(\theta)\rangle_\theta\right] = 0. \quad (11)$$

The frequency ω of the natural oscillations of magnetization coincides to the terms proportional to $\chi_0 \sim \mu_0^2\nu(\varepsilon_F)$, with the frequency $\omega^{(0)}$ of spin-density free oscillations. At this frequency, the magnetic susceptibility has a sharp maximum $D(\omega, \mathbf{k}) = O(\chi_0)$.

The condition for the absence of collisionless damping of spin waves, as well as other Bose excitations, is reduced to the following inequality:

$$|\omega - n\omega_B \mp \Omega| > \max|k_z v_z|. \quad (12)$$

Outside the region of ω and $\mathbf{k}$ values meeting the condition (12), the functions $f_{n,p}(\theta)$ have a pole. Upon integration with respect to p_z, the dispersion equation acquires an imaginary part responsible for strong wave absorption.

Equations (8) describe spin waves of different polarizations. These equations are symmetric in frequency Ω, so that we can restrict our consideration to the first of them. The second equation can be obtained by the following substitutions: $\Omega \longrightarrow -\Omega$, $\Phi^{(+)} \longrightarrow \Phi^{(-)}$, and $B_+ \longrightarrow B_-$.

In the case of strong spatial dispersion, Eqs. (9) can be simplified. If $\mathbf{kv_m} \gg \omega_B$ and $\omega - \Omega > \mathbf{kv_m}$ (where $\mathbf{v_m}$ is the maximal electron velocity in the $\mathbf{k}$ direction), the phase of the rapidly oscillating component does not have stationary points, and the asymptotic behavior of

(9) is calculated by the integration by parts. Let us consider the scalar product $\mathbf{kv}$ as $\mathbf{kv}(\theta, \varphi) = \mathbf{kv_m}u(\theta, \varphi)$, where $u(\theta, \varphi)$ is a dimensionless function smaller than unity in absolute value. In this case, the spin-density oscillation frequencies are

$$\omega = \gamma_i(\lambda_0, \lambda_1, \ldots)\mathbf{kv_m}, \tag{13}$$

where the constants γ_i are the roots of the equation

$$\det\left[\delta_{np} - \lambda_p\left\langle \frac{e^{i(n-p)\varphi}}{1-\gamma^{-1}u(\theta, \varphi)}\right\rangle_{\theta, \varphi}\right] = 0.$$

Real constants γ_i greater than unity in absolute value correspond to the wave processes. The asymptotic formula (13) describes spin oscillations in the absence of an external magnetic field.

In the region of ω and $\mathbf{k}$ values meeting the inequalities $\mathbf{kv_m} \gg \omega_B$ and $\omega - \Omega > \mathbf{kv_m}$, the asymptotic expressions for the integral in the numerator of Eq. (9) can be obtained by the stationary phase method. If the additional conditions $k_z v_z \ll \omega_B$ and $\omega \ll k_x v_x$ are met, the spin-wave frequencies are determined by the following expressions:

$$\begin{aligned} \omega^{(\pm)} &= m\omega_B + \Omega + \Delta\omega, \\ \Delta\omega \ll \omega_B, &\quad m = 0, 1, 2, \ldots. \end{aligned} \tag{14}$$

Taking into account only the first two terms of the dispersion law in Eq. (1) and neglecting the in-plane anisotropy of the layers, we can write the components of the conduction-electron velocity along the axes x and z as follows:

$$\begin{aligned} v_x &= v_0(\varepsilon_F)(1 + \beta\eta\cos(p_z/p_0))\cos\varphi, \\ v_z &= \eta v_1(\varepsilon_F)\sin(p_z/p_0), \end{aligned} \tag{15}$$

where the constants v_1 and v_0 are on the order of the minimal electron velocity along the layers and β is a dimensionless factor on the order of unity depending on the specific form of functions ε_0 and ε_1. Using Eqs. (15), we find for not-too-high values of n and p that

$$\bar{f}_{n,p} = \frac{1}{k_x r_0}\left(\cot\frac{\pi(\tilde{\omega}-\Omega)}{\omega_B}\cos\frac{\pi}{2}(n-p) + J_0(\epsilon k_x r_0)\frac{\sin\left(2k_x r_0 + \frac{\pi}{2}(n+p)\right)}{\sin\frac{\pi(\tilde{\omega}-\Omega)}{\omega_B}}\right), \tag{16}$$

where $\epsilon = 2\beta\eta(v_0 p_0/\varepsilon_F)$, $J_0(x)$ is the Bessel function and $r_0 = v_0/\omega_B$. Substituting expressions (16) and (14) into the dispersion equation (11), we obtain:

$$\Delta\omega = \frac{m\omega_B + \Omega}{\pi k_x r_0}\gamma_i\left(1 + O\left(\frac{1}{k_x r_0}\right)\right), \tag{17}$$

where γ_i satisfies the equation

$$\det\left[\delta_{np} - \lambda_p\gamma^{-1}\left\{\cos\frac{\pi}{2}(n-p) + (-1)^m J_0(\epsilon k_x r_0)\sin\left(2k_x r_0 + \frac{\pi}{2}(n+p)\right)\right\}\right] = 0. \tag{18}$$

In the model determining the correlation function by the zero and first Fourier harmonics

$$S(\mathbf{p}, \mathbf{p}') = S_0 + 2S_1\cos(\varphi - \varphi')$$

for $\epsilon k_x r_0 \ll 1$, the asymptotic form of Eq. (18) has a single root

$$\gamma = (\lambda_0 + 2\lambda_1 + (-1)^m(\lambda_0 - 2\lambda_1)\sin(2k_x r_0)). \tag{19}$$

As is seen from Eqs. (17) and (19), in the vicinity of the resonance (14) the frequency is a rapidly oscillating function of k_x. It should be noted that even if the magnetic field is not strong, the inequality $k_z v_z \sim \eta k_z v_1 \ll \Omega$ is met over a wide range of values of k_z because of the smallness of the parameter η.

If the condition $k_x v_0 \ll \omega_B$ is met, the dispersion equation is considerably simplified, and simple analytic expressions for the frequencies at arbitrary values of $\eta k_z v_1$ can be obtained. Expanding the exponential function in Eq. (9) in powers of $k_x v_0/\omega_B$, we obtain, after simple manipulations, that the matrix $\bar{f}_{np}$ is diagonal:

$$\begin{aligned} \bar{f}_{np} &\equiv f_n(\omega, k_x, k_z)\delta_{np} \\ &= \delta_{np}\left(f_n(\omega, 0, k_z) - (k_x r_0)^2 \times \sum_{m=-1,0,1}(-1)^m\frac{(1+\delta_{m0})}{4}f_{n+m}(\omega, 0, k_z)\right), \end{aligned} \tag{20}$$

where

$$f_n(\omega, 0, k_z) = \frac{\omega_B\,\mathrm{sgn}(\omega - n\omega_B - \Omega)}{\sqrt{(\omega - n\omega_B - \Omega)^2 - (\eta k v_1)^2}},$$

and the set of Eqs. (8) splits into a set of independent equations. The homogeneous integral equation for the free spin-density oscillations has solutions of the form

$\phi_n(\theta, \varphi) = \tilde{\phi}_n(\theta)e^{in\varphi}$. The frequencies ϕ_n corresponding to ω_n are determined by the following relationship:

$$1 - \lambda_n \frac{\omega_n}{\omega_B} f_n(\omega_n, \mathbf{k}) = 0. \quad (21)$$

If the wave propagates in a longitudinal direction, it is more convenient to proceed directly from Eq. (7), which takes the following form for $\mathbf{k} = (0, 0, k_z)$:

$$\mathbf{\Phi}^{(+)} = -\frac{\mu_0 \tilde{B_+}(k_z v_z + \Omega)}{\tilde{\omega} - k_z v_z - \Omega} + \omega \sum_{m=-\infty}^{\infty} \lambda_m \frac{\bar{\mathbf{\Phi}}_m^{(+)} e^{im\varphi}}{\tilde{\omega} - k_z v_z - m\omega_B - \Omega}. \quad (22)$$

Using this equation to determine $\langle \mathbf{\Phi}^{(+)} \rangle_{\theta, \varphi}$, we obtain the high-frequency magnetic susceptibility:

$$\chi_+(\omega, \mathbf{k}) = \chi_0 \frac{\sqrt{(\omega - \Omega)^2 - (\eta k_z v_1)^2} - \omega \operatorname{sgn}(\omega - \Omega)}{\sqrt{(\omega - \Omega)^2 - (\eta k_z v_1)^2} - \lambda_0 \omega \operatorname{sgn}(\omega - \Omega)}. \quad (23)$$

The spectrum of the transverse electromagnetic waves propagating along the magnetic field and due to the spin-density oscillations is determined from Eqs. (5) and (23):

$$\omega = \frac{\Omega + \sqrt{\lambda_0^2 \Omega^2 + (\eta k_z v_1)^2 (1 - \lambda_0^2)}}{(1 - \lambda_0^2)} + O(\chi_0 \omega). \quad (24)$$

It can easily be seen that the frequency of natural oscillations of the electromagnetic field coincides, to terms proportional to χ_0, with the frequency ϕ_0 of the free spin-density oscillations.

If $\eta k_z v_1 \gg \Omega$ (i.e., spin waves propagate in the absence of an external magnetic field), it follows from Eq. (24) that

$$\omega = \eta k_z v_1 / \sqrt{1 - \lambda_0^2}. \quad (25)$$

According to Eq. (25), the frequency at $\mathbf{B}_0 = 0$ is real if $\tilde{S_0} > -1/2$, whereas the phase velocity should exceed the maximal velocity ηv_1 of electron drift in the $\mathbf{k}$ direction. In the long-wavelength limit $\eta k_z v_1 \ll \Omega$, the frequency (24) coincides with the spin-resonance frequency ω_s for free quasiparticles.

Under the conditions of weak spatial dispersion in the $\mathbf{x}$ direction, the shift in the frequency (24), proportional to $(k_x v_0/\omega_B)^2$, can easily be found from Eq. (21):

$$\Delta\omega = \frac{\lambda_0^3 \omega^3}{\omega_B \sqrt{\lambda_0^2 \Omega^2 + (\eta k_z v_1)^2 (1 - \lambda_0^2)}} \Delta f(\omega, \mathbf{k}), \quad (26)$$

where ω is determined by Eq. (24) and $\Delta f(\omega, \mathbf{k}) = f_0(\omega, k_x, k_z) - f_0(\omega, 0, k_z)$.

Spin waves can be detected experimentally by monitoring the selective transparency of thin films in the vicinity of the frequencies of magnetic susceptibility resonance. Comparison of the values of $\omega(\mathbf{k})$ for different $\mathbf{k}$ would make it possible to determine the constant $\tilde{S_0}$ which characterizes the exchange interaction between the charge carriers.

REFERENCES

1. M. V. Kartsovnik, V. N. Laukhin, V. N. Nizhanovskiĭ, *et al.*, Pis'ma Zh. Éksp. Teor. Fiz. **47**, 302 (1988) [JETP Lett. **47**, 363 (1988)].
2. M. V. Kartsovnik, P. A. Kononovich, V. N. Laukhin, and I. Shchegolev, Pis'ma Zh. Éksp. Teor. Fiz. **48**, 498 (1988) [JETP Lett. **48**, 541 (1988)].
3. V. P. Silin, Zh. Éksp. Teor. Fiz. **35**, 1243 (1958) [Sov. Phys. JETP **8**, 870 (1958)].
4. S. Schultz and G. Dunifer, Phys. Rev. Lett. **18**, 283 (1967).
5. N. P. Zyryanova, V. I. Okulov, and V. P. Silin, Tr. Inst. Fiz. Met., Akad. Nauk SSSR **31**, 38 (1975).
6. L. D. Landau, Zh. Éksp. Teor. Fiz. **30**, 1058 (1956) [Sov. Phys. JETP **3**, 920 (1956)].
7. V. P. Silin, Zh. Éksp. Teor. Fiz. **33**, 495 (1957) [Sov. Phys. JETP **6**, 387 (1957)].

Translated by K. Chamorovskiĭ

JETP Letters, Vol. 78, No. 5, 2003, pp. 327–331. Translated from Pis'ma v Zhurnal Éksperimental'noĭ i Teoreticheskoĭ Fiziki, Vol. 78, No. 5, 2003, pp. 777–781.

Sticking of Carbon Nanotube Y Junction Branches

L. A. Chernozatonskii and I. V. Ponomareva

Institute of Biochemical Physics, Russian Academy of Sciences, Moscow, 119991 Russia

e-mail: cherno@sky.chph.ras.ru; iponomar@sky.chph.ras.ru

Received July 30, 2003

The coalescence of branches in the Y junctions of single-wall carbon nanotubes (10 nm long) is predicted to occur when the branches approach each other under the action of a load (~10 nN) applied to their ends. A transition to the new state with parallel branches bound by molecular interactions was simulated and the energy characteristics were calculated by the molecular dynamics method. The Y junctions with parallel branches are stable at temperatures up to 2000 K. It is established that there is a threshold distance between the branch ends, below which the branches exhibit spontaneous sticking under the action of molecular attraction forces. If the branches are unloaded before this threshold distance is reached, they oscillate (acting as a nanodimensional "tuning fork") at a frequency of ~100 GHz. © *2003 MAIK "Nauka/Interperiodica".*

PACS numbers: 61.46.+w; 81.07.De

The Y junctions of carbon nanotubes have drawn the interest of researchers due to the unusual geometry and unique electronic properties [1–3]. In these junctions, three nanotubes are matched at the expense of topological defects (pentagons, heptagons and/or octagons) introduced into the perfect hexagonal lattice of carbon atoms, so that the sp^2 electron configuration of each atom is retained [4–7]. The interest in these structures was stimulated primarily by the possibility of macroscopic synthesis of carbon nanotubes with Y junctions and by observations of the nonlinear current–voltage characteristics of such junctions [7–9]. However, mechanical characteristics of the Y junctions of carbon nanotubes were studied neither theoretically nor experimentally.

We have simulated by the molecular dynamics method the Y junctions of single-wall carbon nanotubes (SWCNs) with a length of up to a few tens of nanometers and an acute angle between the branches and their behavior under the action of an external load. When a load is applied to the Y junction branch ends, the distance between the branches decreases to 3.4 Å. It was found that weak van der Waals forces between the branches are sufficient to keep them parallel upon unloading. This effect indirectly confirms the prediction made by R. Feynman in 1960 [10], according to which nanomaterials will encounter the problem of coalescence as a result of intermolecular interactions, which may lead to effects that are impossible on a macroscopic scale.

Formulation of the problem. Molecular dynamics (MD) simulation was carried out using the Brenner potential [11] for covalent bonds between carbon atoms and the Lennard-Jones potential for long-range interactions. It should be noted that the Brenner potential was used for the description of dynamics [12] and mechanical properties [13, 14] of carbon nanotubes, because this potential allows simulation a systems with large numbers of atoms (~10^4) and gives reliable results when compared to those obtained by more precise quantum-mechanical calculations [15–18].

We have considered two types of Y junctions of the armchair SWCNs [19], both comprising (20,20) SWCN stems branched into (13,13) branches. Both structures possessed the same configuration of topological defects, representing six heptagons situated in the

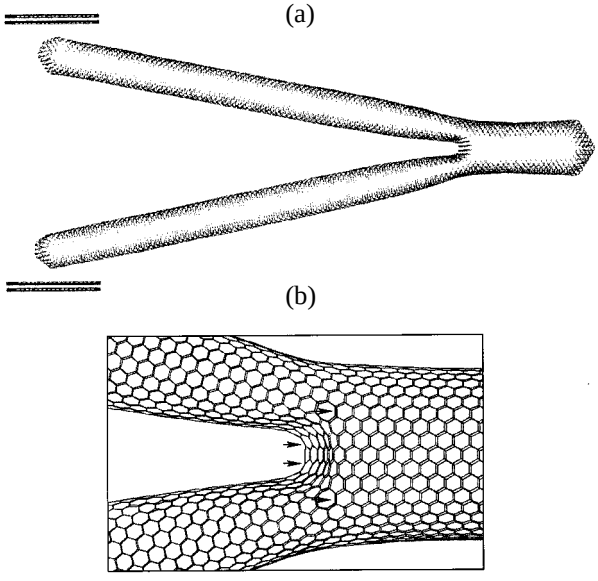

Fig. 1. (a) Mutual arrangement of the graphite planes and the long-branch Y junction at the beginning of simulation; (b) defect structure of the branching region of the Y junction (arrows indicate the positions of heptagons).

0021-3640/03/7805-0327$24.00

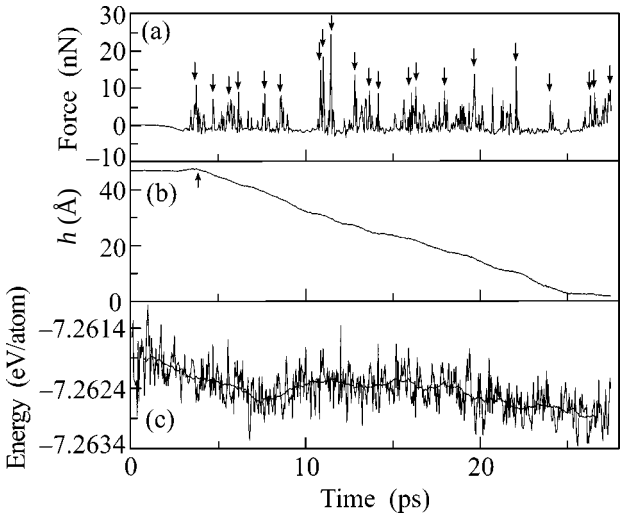

Fig. 2. Time variation of the main characteristics determined in the course of MD simulation: (a) the force with which a GPs acts upon the SBJ branch (arrows indicate the peaks used for averaging); (b) the distance between SBJ branches; (c) total energy of the system.

branching region (see Fig. 1b), but had different branch lengths of 100 and 210 Å. The former structure will be referred to as the short-branch junction (SBJ) and the latter as the long-branch junction (LBJ). Optimization of the system geometry by MD simulation showed that this topology corresponds to an angle of 23° between the branches, in good agreement with the experimentally observed geometry of Y junctions [7, 8].

Prior to MD simulation, each Y junction was placed between two graphite planes (GPs) parallel to the stem axis (Fig. 1a) so that the initial distance from each plane to the nearest carbon atom of the nanotube branch was 8 Å. The applied load was simulated by moving the GPs toward each other with a preset velocity. In each MD simulation step (5×10^{-4} ps), the coordinates of the GPs were fixed, so as to model the interaction of the Y junction with large planes. The motion of GPs with a preset velocity was modeled by changing their coordinates prior to each MD simulation step.

In order to determine the optimum GP velocity, we carried out a series of preliminary simulations using various velocities. It was found that moving GPs with a velocity above 2 Å/ps leads to the fracture of nanotube structure, while velocities too small allow the Y junction to rotate and slip off the GPs. Note that, in experiments, Y junctions usually lie on a substrate surface and no such slippage takes place. However, simulation of a system with substrate would significantly increase the number of atoms in the system and, hence, the computational time, but not lead to any qualitative changes in the simulated process. Therefore, the above value should be considered as a GP velocity effective for a numerical experiment.

As a result of loading in the chosen regime, the Y-junction branches approach each other without any significant shape deformation. The velocity of mutual approach is close to the relative velocity of GP motion. It was found that the prolonged action of load gave rise to a new geometric configuration of the Y junction, namely, to a junction with parallel branches. This configuration is stable at temperatures up to 2000 K.

Short-branch Y junctions. At the beginning of simulation, the distance between GPs was 92 Å. The total simulation time was 27.5 ps. Time variation of the force acting upon one branch of a SBJ under load is shown in Fig. 2a. Here, a negative value of the force corresponds to the branch attraction to the GP. As can be seen from this graph, the force initially exhibits (within 3 ps) a smooth decrease from 0 to –1.7 nN. Then, the character of the force shows a sharp change, as manifested by the appearance of numerous "repulsion" peaks. In order to explain these features, let us consider the interaction between the SBJ branches and GPs in the course of simulation.

Note that the minimal force (–1.7 nN) is observed when the branch–GP distance corresponds to an interlayer spacing in the graphite structure (3.4 Å). At the same time, the distance h between the SBJ branches (Fig. 2b) somewhat increases (indicated by the arrow), which is evidence of the attraction between the GP and the branch. Here, by the distance h between branches we imply the minimum distance between the atoms belonging to different branches and situated near the branching region. Figure 2b shows a projection of this distance onto the direction of GP motion. At a time of 3.4 ps after the beginning of simulation, the force changes sign (to become repulsive) and, after 0.4 ps (800 simulation steps), the branches start to approach each other and the force starts to oscillate. The distance between branches decreases almost linearly (Fig. 2b), and the rate of mutual approach (2.08 Å/ps) is close to the relative velocity of GP motion (2.00 Å/ps). Starting from this moment, the distance between SBJ branches and GPs exhibits oscillations within the graphite interlayer spacing (3.3–3.5 Å), thus providing the van der Waals interaction. A decrease in the branch–GP distance below 3.4 Å leads to the appearance of a repulsive force, while an increase above this value gives rise to attraction.

Thus, the van der Waals interaction serves as a mediator of the motion transfer from the GPs to the branches of the Y junction. This mutual motion of the junction branches and GPs will be called the stable interaction regime. The two main assumptions about the behavior of the interaction force in this regime are as follows: (i) the force oscillations in the stable interaction regime are caused by simulation: discrete GP motions lead to a discrete change in the distance between the GP and the Y junction branches and, hence, to a discrete variation in the interaction force; (ii) under real conditions, the force with which the GP acts upon the junction

branches must be constant and directed along the GP motion direction. In order to check for the validity of both assumptions, the total energy of the system was plotted against the simulation time, as depicted in Fig. 2c. As can be seen from this plot, the energy of the system also oscillates, confirming the artificial nature of these oscillations (the first assumption). Behavior of the average energy (thick solid curve in Fig. 2c) shows that the process is barrierless and, hence, the force acting on the Y junction must be constant (the second assumption).

Based on the second assumption, we averaged over the main repulsion peaks (indicated by arrows in Fig. 2a) to estimate the force required for changing the Y junction shape. Note that the repulsion peaks are responsible for the resistance of the Y junctions to deformation. Averaging gives an upper estimate of 10 nN for the force, which corresponds to a pressure of 1 GPa acting on the interaction area of 10 nm^2.

After 27.5 ps, the distance between SBJ branches decreases to 3.4 Å, which corresponds to a Y junction with parallel branches. Then, the GPs were removed and the MD simulation of this system was continued for 25 ps at 300 K. Figure 3a shows the SBJ shape after this procedure. The energy of this parallel configuration is 5.5 eV lower than that of the initial configuration with an angle of 23° between branches. In order to characterize the transition between these states, we (i) constructed the potential energy curve of the Y junction versus the distance between branches (see inset in Fig. 4) and (ii) studied the behavior of the Y junction in the states corresponding to the vicinity of the expected extremum on this curve. For this purpose, the entire SBJ loading process (0 to 27.5 ps) was divided into four sequential intervals. At the end of each interval, the GP was removed (to exclude the GP–SBJ interaction) and the potential energy of the Y junction was calculated. As can be seen from the inset in Fig. 4, the transition is likely barrierless. A plateau on the potential energy curve indicates that the transition requires applying a constant external force (in our case, this action was provided by GPs). As the distance between SBJ branches further decreases, the energy plateau changes to a monotonic decrease in energy, which implies a transition to the local energy minimum in the absence of an external force. Thus, the energy extremum point lies in the interval from 14.5 to 23 Å.

In order to check for this assumption, we performed additional simulation. At the time moment when the distance between branches reached 23 Å (right boundary of the above interval), the GP motion direction changed to the opposite (i.e., the GPs began to move apart), thus gradually decreasing to zero the force acting on the Y junction. After a 20-ps simulation, the distance between SBJ branches increased to 50 Å. In the course of the subsequent 60 ps, the SBJ branches exhibit oscillations about an equilibrium distance of 42 Å (estimated from the average distance between the

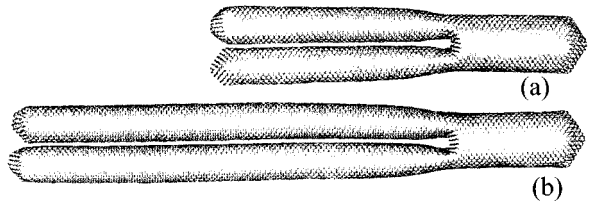

Fig. 3. The Y junctions with (a) short and (b) long branches spaced by 3.4 Å upon unloading.

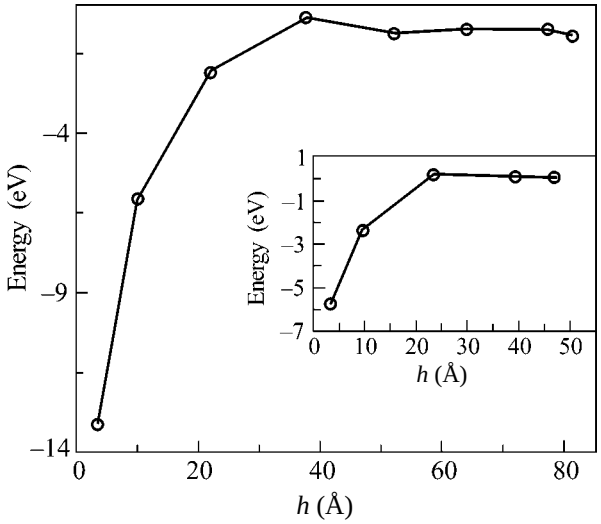

Fig. 4. A plot of the potential energy of LBJ versus distance between branches. The inset shows an analogous curve for SBJ.

first maximum and first minimum). This value is very close to the distance between branches at the beginning of simulation (see inset in Fig. 4), suggesting that the system will return to the initial state (with an acute angle between branches) after termination of oscillations. However, investigation of the entire oscillation process would be computationally exhaustive.

In the next run of the simulation, we reversed the GP motion direction at the moment when the distance between the SBJ branches reached 14.5 Å (left boundary of the interval containing the expected point of extremum). Within the subsequent 5 ps, the Y junction passed to the state with parallel branches, irrespective of the direction of GP motion.

Thus, the results of these simulations confirmed that there exists a critical distance between SBJ branches (14.5–23 Å), below which the branches spontaneously approach each other even in the absence of the external force. The possibility of such process is caused by a decrease in the potential energy of the deformed junction (see inset in Fig. 4).

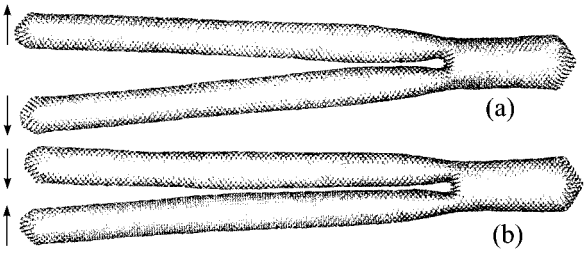

Fig. 5. LBJ configurations at various steps of simulation (arrows indicate the direction of GP motion): (a) the distance between branches is 25.3 Å and only about quarter of the branch length is involved in the van der Waals interaction; (b) the distance between branches is 14 Å and more than half of the branch length is involved in the van der Waals interaction (the junction behaves as a zipper, the branches approach each other irrespective of the direction of GP motion).

In order to check for the stability of the Y junction with parallel branches, we performed MD simulations at temperatures of 600, 800, 1000, and 2000 K. It was established that the SBJ branches did not move apart under these conditions.

Long-branch Y junctions. All calculations described above were repeated for the Y junction with long branches (Fig. 1) confined between GPs moving with a velocity of 2 Å/ps. The total simulation time was 45 ps. Similar to the case of SBJ, the force with which the GP acted on the LBJ exhibited an irregular oscillation character. After 5.05 ps, the distance between the LBJ branches began to decrease linearly with time and reached 3.4 Å (as in SBJ) at the end of simulation. Here, the Y junction with parallel branches (Fig. 3b) provides a 12.2 eV energy gain, as compared to the initial configuration with an acute angle between branches.

A potential energy curve for the LBJ is depicted in Fig. 4, where the extreme right point corresponds to the initial junction with an angle of 23° between branches and the extreme left point, to the Y junction with coalesced branches. As can be seen in this curve, the energy plateau changes to an 0.5-eV barrier, which is followed by a gradual decrease in energy. Because of the presence of a barrier, the simulations with GPs moving apart were performed for three initial configurations corresponding to h = 38, 25, and 14 Å.

For h = 38 and 25 Å (Fig. 5a), the LBJ branches diverge when the direction of GP motion changes to opposite. Since the system comprising the LBJ and the GPs contains 13274 atoms, the continuation of the simulation for studying the stage of oscillations would be an extremely cumbersome procedure. For this reason, the possible equilibrium distance between the LBJ branches was not estimated after the termination of oscillations, as it was done in the case of SBJ. The main conclusion drawn from the results of this MD simulation is that the distance between the Y-junction branches increases upon unloading. This implies that the spontaneous attraction of branches is impossible and they approach each other only in the presence of a constant external force.

The subsequent MD simulation showed that the initial LBJ configuration with h = 14 Å (Fig. 5b) ensured spontaneous mutual approach irrespective of the direction of GP motion. Thus, this junction, as also with the SBJ, is characterized by a certain critical distance between the branches (14–25 Å), below which the branches may spontaneously approach each other even without applying an external force. Energetically, this process is driven by lowering of the potential energy after traversing the energy plateau (Fig. 4). In order to explain the existence of this critical distance, let us consider Figs. 5a and 5b. As can be seen, the region between branches involved in the van der Waals interaction accounts for only about quarter of the branch length in Fig. 5a and for more than half of the branch length in Fig. 5b.

Based on the above analysis, we may conclude that the van der Waals forces play a key role in the process of spontaneous attraction of the LBJ branches: as soon as more than half of the branch length is covered by this interaction, the branches coalesce (like a zipper), whereby the intermolecular forces acting between nanotubes drive them to spontaneously approach each other. The stabilizing role of the van der Waals forces is confirmed by the fact that the energy difference between the state with an acute angle between branches and the state with parallel branches increases with the branch length (5.5 and 12.2 eV for SBJ and LBJ, respectively).

It was established that the Y junctions unloaded before the distance between their branches (~10 nm long) approach the threshold value execute oscillations (like a tuning fork) at a frequency of ~100 GHz.

Thus, in contrast to the macroscopic systems where the Y-shaped configuration can behave as a spring with the ends always diverging upon unloading, whereby the system returns to the initial state, the molecular interaction between closely spaced nanotubes is an important factor in the analogous nanosystem. The examples considered above show that the intermolecular attraction between the branches of a Y junction can prevail over the restoring elastic force caused by the deformation of the system. This accounts for the effect of coalescence that is impossible on the macroscopic level. The new state with parallel branches bonded by a weak intermolecular interaction is stable up to a temperature of 2000 K and is energetically more favorable than the state of Y junction with diverging branches. These results show that the van der Waals interaction plays a key role in nanotube Y junctions with closely spaced branches.

We are grateful to N.G. Lebedev and M. Menon for fruitful discussions and valuable remarks.

This study was supported by the Federal Scientific-Technological Program “Currently Important Direc-

tions in Physics of Condensed Media" (Fullerenes and Atomic Clusters) and by the Federal Program "Low-Dimensional Quantum Structures" (project no. 9.21).

REFERENCES

1. A. N. Andriotis, M. Menon, D. Srivastava, and L. Chernozatonskii, Phys. Rev. Lett. **87**, 066802 (2001).
2. A. N. Andriotis, M. Menon, D. Srivastava, and L. Chernozatonskii, Phys. Rev. B **65**, 165416 (2002).
3. M. Menon and D. Srivastava, Phys. Rev. Lett. **79**, 4453 (1997).
4. L. A. Chernozatonskii, Phys. Lett. A **172**, 173 (1992).
5. G. E. Scuseria, Chem. Phys. Lett. **195**, 543 (1992).
6. V. H. Crespi, Phys. Rev. B **58**, 12671 (1998).
7. C. Papadopoulos, A. Rakitin, J. Li, *et al.*, Phys. Rev. Lett. **85**, 3476 (2000).
8. J. Li, C. Papadopoulos, and J. Xu, Nature **402**, 253 (1999).
9. B. C. Satishkumar, P. J. Thomas, A. Govindraj, and C. N. Rao, Appl. Phys. Lett. **77**, 2530 (2000).
10. R. F. Feinman, Ross. Khim. Zh. **46**, 4 (2002).
11. D. W. Brenner, O. A. Shendorova, J. A. Harrison, *et al.*, J. Phys.: Condens. Matter **14**, 783 (2002).
12. M. B. Nardelli, B. I. Yakobson, and J. Berholic, Phys. Rev. Lett. **81**, 4656 (1998).
13. D. H. Roberston, D. W. Brenner, and J. W. Mintmire, Phys. Rev. B **45**, 12592 (1992).
14. D. Srivastava, C. Wei, and K. Cho, Appl. Mech. Rev. **56** (2), 215 (2003).
15. Q. Zhao, M. B. Nardelli, and J. Bernholic, Phys. Rev. B **65**, 144105 (2002).
16. D. Sanchez-Portal, E. Artacho, J. M. Solex, *et al.*, Phys. Rev. B **59**, 12678 (1999).
17. E. Hernandez, C. Goze, P. Bernier, and A. Rubio, Phys. Rev. Lett. **80**, 4502 (1998).
18. P. Zhang, P. E. Lammert, and V. Crespi, Phys. Rev. Lett. **81**, 5346 (1998).
19. R. Satio, M. Fujita, G. Dresselhaus, and M. S. Dresselhaus, Phys. Rev. B **46**, 1804 (1992).

Translated by P. Pozdeev

JETP Letters, Vol. 78, No. 5, 2003, pp. 332–335. Translated from Pis'ma v Zhurnal Éksperimental'noĭ i Teoreticheskoĭ Fiziki, Vol. 78, No. 5, 2003, pp. 782–785.

Phenomenological Description of a Giant Temperature Hysteresis of Ultrasound Velocity and Internal Friction in Lanthanum Manganite

A. P. Saiko* and S. A. Markevich

Institute of Solid State and Semiconductor Physics, National Academy of Sciences of Belarus, Minsk, 220072 Belarus
**e-mail: saiko@ifttp.bas-net.by*

Received July 31, 2003

We propose an explanation for the experimentally observed [1] giant temperature hysteresis of the ultrasound velocity and internal friction in single crystals of lanthanum manganite ($La_{0.8}Sr_{0.2}MnO_3$). The effect is interpreted within the framework of a phenomenological model based on the notion of two coexisting sublattices of the oxygen octahedra performing cooperative tilting-rotational oscillations in bistable potential fields. © *2003 MAIK "Nauka/Interperiodica".*

PACS numbers: 43.35.Cg; 62.65.+k

Manganese perovskites $R_{1-x}A_xMnO_3$ (*R* = La or another rare earth element; A = Ca, Sr, Ba, …) have recently drawn much attention due to the phenomenon of colossal magnetoresistance (CMR) that makes these compounds promising materials for magnetic sensors and data-reading devices. Now it is commonly accepted that an important role in the formation of a CMR response in manganites is played by the interaction of a crystalline lattice with the electron and spin degrees of freedom. However, despite a very large body of experimental data, there are still many open questions related to the quantitative description of the metal–dielectric transition, phase coexistence, and some features in the elastic properties of these compounds.

Recently [1], temperature hysteresis of a giant width (extending over a temperature interval from 80 to 350 K) of the longitudinal ultrasonic wave velocity and the internal friction was observed in a single crystal of lanthanum manganite $La_{0.8}Sr_{0.2}MnO_3$ possessing CMR properties. According to this, the sound velocity in a sample on heating from 80 to 105 K is significantly lower than that on cooling in the same temperature interval, while in the 105–350 K range, a difference in sound velocities is several times smaller. The curve of the internal friction exhibits a sharp peak at 105 K (on heating) and less pronounced peaks at 350 K (on heating) and 80 K (on cooling).

The presence of a giant temperature hysteresis in the elastic properties of lanthanum manganite can be explained within the framework of the phenomenological model of a correlated bistable sublattice [2].

Consider a crystal lattice with a polyatomic basis, in which atoms (ar atomic groups) of one sort perform optical oscillations in an asymmetric double-well potential formed in the core (matrix lattice) field. If the motion of such atoms is strongly correlated and possesses a cooperative character (e.g., due to a long-range order), this will suppress the fluctuational over-barrier transitions between the potential wells. For this reason, and because of the potential asymmetry, the atomic ensemble under consideration may occur in metastable states forming a bistable sublattice. On heating, the sublattice exhibits evolution from oscillations in the global minimum to overbarrier oscillations with almost excluded slower movement (transitions from the global minimum of the seeding potential to the local minimum and vice versa).

It is suggested that octahedra of the perovskite structure of lanthanum manganite, with oxygen ions at the vertices and manganese ions at the center, perform tilting-rotational motions in the double-well asymmetric potential. These oscillations of the octahedra are strongly correlated because of the strong interaction between the charge, spin, and lattice degrees of freedom characteristic of this compound. A transition from the global to metastable minimum of the free energy on heating corresponds to the appearance of rhombohedral distortions in the initially orthorhombic low-temperature structure. There are two types of bistable sublattices of the oxygen octahedra with different positions of metastable minima of the seeding potentials (Fig. 2), which is evidenced by (i) the appearance of experimentally observed rhombohedral component in the orthorhombic phase in a sample heated from zero temperature and (ii) the absence of orthorhombic inclusions on cooling from $T > 350$ K down to 105 K (the two types of bistable sublattices can be related to the presence of two kinds of positive ions, La^{3+} and Sr^{2+}). Bistable oscillations of the oxygen octahedra modulate frequencies of the vibrational spectrum of the matrix lattice,

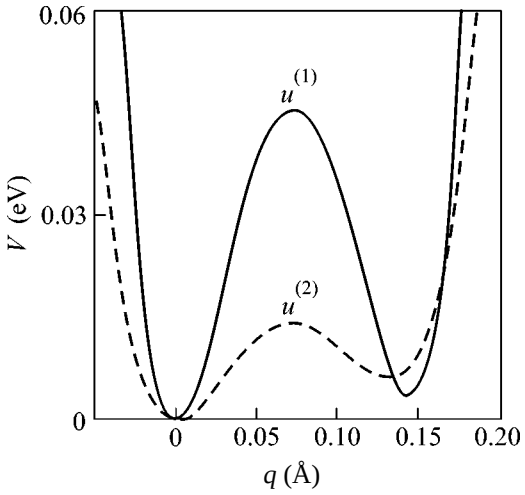

Fig. 1. Double-well seeding potentials for the two sublattices of oxygen octahedra: $u^{(1)} = 0.045$ eV (potential barrier height); $q_1^{(1)} = 0.073$ Å and $q_2^{(1)} = 0.144$ Å (coordinates of the maximum and metastable minimum of the seeding potential for the first sublattice); the corresponding values for the second sublattice are $u^{(2)} = 0.014$ eV, $q_1^{(2)} = 0.073$ Å, $q_2^{(2)} = 0.132$ Å.

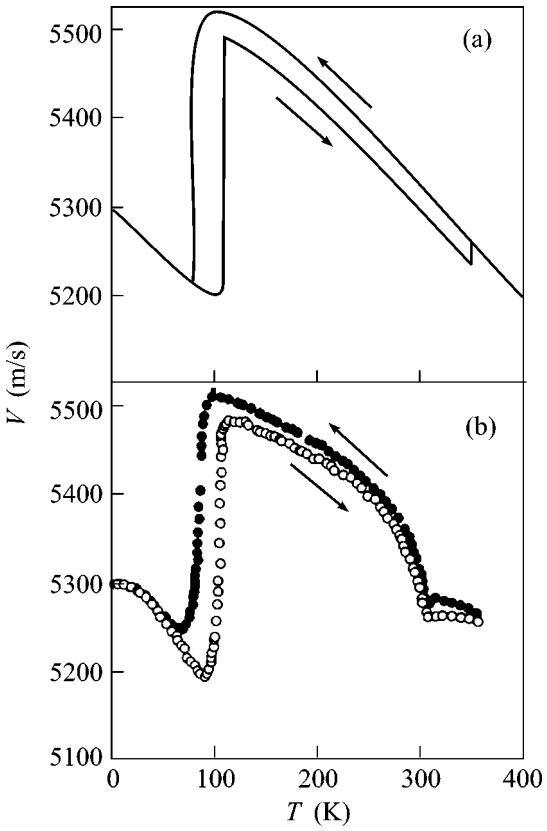

Fig. 2. Temperature dependence of the ultrasonic wave velocity: (a) calculated using formula (4) for a crystal with two bistable sublattices coupled by a quartet interaction (5); formula (4) was corrected by adding a contribution from the matrix sublattice, $A–BT$, where $A = 2996$ ms^{-1}, $B = 1.58$ ms^{-1} K^{-1}, and (determined from experimental data [1]) $\lambda_{kk}^{(1)}/\mu_k\omega_k^2 = 2$ Å^{-2} and $\lambda_{kk}^{(2)}/\mu_k\omega_k^2 = 30$ Å^{-2}; $u^{(1)} = 0.045$ eV, $q_1^{(1)} = 0.073$ Å, $q_2^{(1)} = 0.144$ Å, $u^{(2)} = 0.014$ eV, $q_1^{(2)} = 0.073$ Å, $q_2^{(2)} = 0.132$ Å; (b) experimental velocity of ultrasound measured for $La_{0.8}Sr_{0.2}MnO_3$ [1].

which is manifested by anomalies in the elastic properties.

The theory of a temperature hysteresis of the elastic properties of lanthanum manganite can be constructed based on the following phenomenological model using a spin Hamiltonian (reduced to a single octahedron) of the type

$$H = H_h + H_{anh} + H_{\text{int}}. \tag{1}$$

Here, the first term, H_h, represents the matrix lattice Hamiltonian and is selected in the form of a Hamiltonian of the set of harmonic oscillators with the parameters normalized to the empirical values of lattice constants of the compound under consideration. The second term, H_{anh}, is an effective Hamiltonian of the oxygen octahedra performing tilting-rotational oscillations in the asymmetric double-well potentials of the two types (Fig. 1):

$$V^{(i)} = \frac{\alpha^{(i)}}{2}(q^{(i)})^2 - \frac{\beta^{(i)}}{3}(q^{(i)})^3 + \frac{\gamma^{(i)}}{4}(q^{(i)})^4, \tag{2}$$

where $q^{(i)}$ are the generalized coordinates describing the vibrational motion of the octahedra in a potential with the higher (lower) barrier and the deep (shallow) metastable minimum, $i = 1$ ($i = 2$); $\alpha^{(i)}$, $\beta^{(i)}$, and $\gamma^{(i)}$ (>0) are the parameters.

Interaction between the lattice oscillators and the nonlinear oscillations of the oxygen octahedra is described by the third term in Eq. (1), which is selected in the following form:

$$H_{\text{int}} = \sum_i (q^{(i)})^2 \sum_{k,k'} (\lambda_{kk'}^{(i)})^2 x_k x_{k'}, \tag{3}$$

where x_k is the displacement of the kth oscillator (mode) and $\lambda_{kk'}^{(i)}$ are the force constants of the bonds. An analysis shows that the effective frequency ε_k of the longwave phonons (or the sound velocity) in this model significantly depends on the temperature and exhibits temperature hysteresis. This is related to a temperature-dependent distortion of the asymmetric potentials (2) and the occupation of metastable states of the oxygen octahedra.

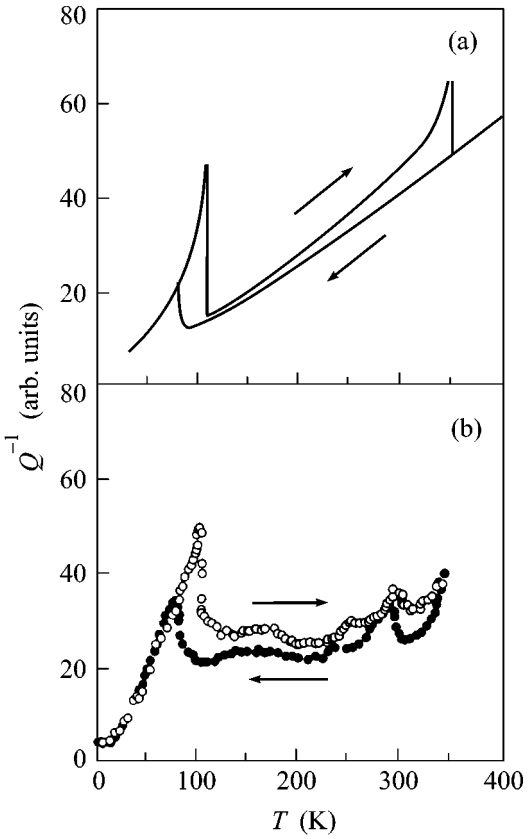

Fig. 3. Temperature dependence of the internal friction: (a) calculated for a crystal with two bistable sublattices using formula (7) with $u^{(1)} = 0.045$ eV, $q_1^{(1)} = 0.073$ Å, $q_2^{(1)} = 0.144$ Å, $u^{(2)} = 0.014$ eV, $q_1^{(2)} = 0.073$ Å, $q_2^{(2)} = 0.132$ Å (the contribution of the matrix sublattice is subtracted as background); (b) experimental internal friction curve measured for $La_{0.8}Sr_{0.2}MnO_3$ [1].

The velocity v of an ultrasonic wave is determined from the temperature-dependent frequency ε_k renormalized by the interaction H_{int}:

$$v(T) \sim \varepsilon_k(T) = \omega_k\left[1 + \sum_i \frac{\lambda_{kk}^{(i)}}{\mu_k\omega_k^2}(\sigma^{(i)} + \langle q^{(i)}\rangle^2)\right], \quad (4)$$

where k is the wavevector of the mode for which the ultrasonic measurements are performed; ω_k and μ_k are the seeding frequency and the mass of the kth oscillator in the matrix lattice, respectively; $\langle q^{(i)}\rangle$ and $\sigma^{(i)} = \langle(q^{(i)} - \langle q^{(i)}\rangle)^2\rangle$ are the statistical mean values of the generalized coordinates and the corresponding dispersions, determined from a system of self-consistent equations,

$$(\beta^{(i)} - 3\gamma^{(i)}\langle q^{(i)}\rangle)\sigma^{(i)} = \alpha^{(i)}\langle q^{(i)}\rangle - \beta^{(i)}\langle q^{(i)}\rangle^2 + \gamma^{(i)}\langle q^{(i)}\rangle^3,$$

$$\sigma^{(i)} = \frac{1}{2m\Omega^{(i)}}\coth\frac{\Omega^{(i)}}{2\theta}, \quad (5)$$

where

$$(\Omega^{(i)})^2 = \frac{1}{m}[\alpha^{(i)} - 2\beta^{(i)}\langle q^{(i)}\rangle + 3\gamma^{(i)}(\sigma^{(i)} + \langle q^{(i)}\rangle^2)]$$

are the frequencies of oscillations of the octahedra (the temperature dependences of these frequencies and the $\langle q^{(i)}\rangle$ and $\sigma^{(i)}$ values exhibit hysteresis) and $\theta = k_BT$. The quantum-statistical expressions for $\sigma^{(i)}$ (5) in the regime of strong correlations can be replaced by the corresponding classical limits, $\sigma^{(i)} = \theta/m(\Omega^{(i)})^2$, since the cooperative behavior of the oxygen octahedra extends over several unit cells and, hence, the quantum fluctuations can be ignored in the calculation of means.

Apparently, the temperature hysteresis of the elastic constants of the matrix lattice in the temperature interval from 105 to 350 K will be provided by the cooperative oscillations of octahedra in the anharmonic potential with a higher barrier, while the behavior in the 80–105 K interval will be determined by the cooperative oscillations of octahedra in the potential with a lower barrier. The relative number of octahedra performing oscillations in the anharmonic potential of the first type can be estimated from the experimental data as a fraction of the orthorhombic phase in the rhombohedral phase at $T > 105$ K (this fraction amounts to about 6% [1]). Some other experimental data, such as the relative difference between the elastic characteristics observed on heating and cooling in the temperature interval of bistability and the temperature range of hysteresis, allow the obtaining of realistic estimates for the parameters of bistable potentials modeling the correlated motions of the oxygen octahedra: $u^{(1)} = 0.045$ eV (potential barrier height); $q_1^{(1)} = 0.073$ Å and $q_2^{(1)} = 0.144$ Å (coordinates of the maximum and metastable minimum of the seeding potential for the first sublattice); the corresponding values for the second sublattice are $u^{(2)} = 0.014$ eV, $q_1^{(2)} = 0.073$ Å, and $q_2^{(2)} = 0.132$ Å; $\lambda_{kk}^{(1)}/\mu_k\omega_k^2 = 2$ Å^{-2} and $\lambda_{kk}^{(2)}/\mu_k\omega_k^2 = 30$ Å^{-2} (normalized constants of coupling of the first and second sublattices to the matrix lattice).

Figure 2a shows a plot of the ultrasonic wave velocity calculated using formula (4). As can be seen, the theoretical temperature dependence well describes the experimental behavior depicted in Fig. 2b. Indeed, in the region of hysteresis, the higher velocities are observed on cooling and the lower, on heating. In the heating mode, there is a sharp increase in v in the region of 105 K, which is related to the appearance of rhombohedral distortions during the tilting-rotational oscillations of correlated octahedra in the bistable potential with a lower barrier $u^{(2)}$. A lower magnitude of the hysteresis in the interval from 105 to 350 K is related to a smaller contribution to the renormalized phonon frequencies from the oxygen octahedra moving in the bistable potential with a higher barrier $u^{(1)}$ (see the legend to Fig. 2). Thus, for reasonable values of the

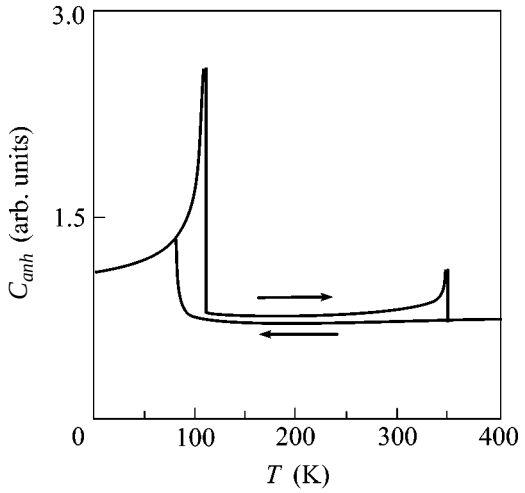

Fig. 4. Temperature dependence of the total heat capacity calculated for two bistable sublattices with the parameters (1) $u^{(1)} = 0.045$ eV, $q_1^{(1)} = 0.073$ Å, $q_2^{(1)} = 0.144$ Å and (2) $u^{(2)} = 0.014$ eV, $q_1^{(2)} = 0.073$ Å, $q_2^{(2)} = 0.132$ Å. The weight contribution of the first sublattice is 10% relative total of the second sublattice.

model parameters, both the magnitude and the characteristic temperature intervals (80–105 K and 105–350 K) of the hysteresis, and the direction of traversing this loop in the heating–cooling cycle agree with the experiment.

For an ultrasonic wave with a frequency of ω_k = 80 kHz, we have $\omega_k\tau_{ph} \ll 1$ (τ_{ph} is the lifetime of thermal phonons). For this reason, a comparison of the theoretical temperature dependence of the viscous friction (ultrasound damping) Q^{-1} with the experimental curve (Fig. 3) was performed using a relation [3]

$$Q^{-1} \sim TC_{anh}. \tag{6}$$

Here, C_{anh} is the heat capacity related to the excitation of anharmonic oscillations in the oxygen octahedra (in Fig. 3a, the Debye contribution of the matrix sublattice is subtracted as background), which is calculated using the average energy of these oscillations:

$$\langle H_{anh}\rangle = \sum_{i=1.2} [\alpha^{(i)}\langle q^{(i)}\rangle^2/2 - \beta^{(i)}\langle q^{(i)}\rangle^3/3 + \gamma^{(i)}\langle q^{(i)}\rangle^4/4 + m(\Omega^{(i)})^2\sigma^{(i)} - 3\gamma^{(i)}(\sigma^{(i)})^2/4]. \tag{7}$$

Figure 4 shows the heat capacity C_{anh} calculated (in the classical limit) for the two sublattices of oxygen octahedra. The peaks on the $Q^{-1}(T)$ curve are obviously correlated with the behavior of $C_{anh}(T)$ (cf. Figs. 3 and 4). A more pronounced increase in the internal friction with the temperature in the interval from 105 to 350 K on the calculated dependence as compared to the experimental curve can be related to the temperature-dependent coefficients [3] entering into the formula for Q^{-1}, which are difficult to calculate exactly.

Thus, the temperature hysteresis of a giant width in the ultrasound velocity and the internal friction observed in a single crystal of lanthanum manganite $La_{0.8}Sr_{0.2}MnO_3$ can be explained by the cooperative tilting-rotational motions of oxygen octahedra in the bistable potentials of two types (differing by the barrier heights). Interaction of the metastable states of the octahedra with the longwave phonons leads to a temperature-dependent bistable renormalization of the phonon frequencies and, hence, of the ultrasonic wave velocity. The anharmonic contribution from the two oxygen sublattices to the heat capacity, which has a hysteresis character with peaks at the boundaries of the temperature intervals of bistability, accounts for the corresponding temperature behavior of the viscous friction. The calculated and experimental dependences show a good semiquantitative agreement for realistic values of the model parameters.

REFERENCES

1. R. I. Zaĭnullina, N. G. Bebenin, A. M. Burkhanov, *et al.*, Pis'ma Zh. Éksp. Teor. Fiz. **74**, 120 (2001) [JETP Lett. **74**, 115 (2001)].
2. A. P. Saĭko and V. E. Gusakov, Zh. Éksp. Teor. Fiz. **116**, 168 (1999) [JETP **89**, 92 (1999)]; Zh. Éksp. Teor. Fiz. **108**, 757 (1995) [JETP **81**, 413 (1995)].
3. *Physical Acoustics. Principles and Methods*, Vol. 3B: *Lattice Dynamics* (Academic, New York, 1965; Mir, Moscow, 1968).

Translated by P. Pozdeev

JETP Letters, Vol. 78, No. 5, 2003, pp. 336–338. Translated from Pis'ma v Zhurnal Éksperimental'noĭ i Teoreticheskoĭ Fiziki, Vol. 78, No. 5, 2003, pp. 786–788.

Hole Mobility in a Homogeneous Nucleotide Chain

V. D. Lakhno and N. S. Fialko

Institute of Mathematical Problems of Biology, Russian Academy of Sciences, Pushchino, Moscow region, 142290 Russia
e-mail: lak@impb.psn.ru; fialka@impb.psn.ru

Received August 5, 2003

The conductivity of molecular DNA-based conductors has been calculated. Charge motion is described by quantum-mechanical equations, and macromolecular vibrations are described by classical equations of motion with dissipation and a source of temperature fluctuations. In a homogeneous sequence of G–C nucleotide pairs, the calculated hole mobility at $T = 300$ K equals ≈ 2 cm^2 V^{-1} s^{-1}. © *2003 MAIK "Nauka/Interperiodica".*

PACS numbers: 87.14.Gg; 81.07.Nb; 36.20.-r

In a number of experiments carried out in recent years, it has been found that the DNA molecule can conduct a charge [1–4]. Hence, this opens the possibility of using DNA as a molecular wire in nanoelectronics [5]. In this connection, it seems important to understand the magnitude of the mobility of charge carriers in the "DNA conductor" and to estimate the molecular chain length at which charge transport is efficient.

At present, no experimental data is available on the magnitude of electron and hole mobility in DNA. The reported experiments on charge transfer in DNA provide information on the relative transfer reaction rates rather than mobilities [2–4].

In this paper, we report the results of calculations of hole mobilities at room temperature in a synthetic DNA molecule composed of only guanine (G)–cytosine (C) nucleotide pairs. In such chains, a hole moves over guanine bases, which possess a lower oxidation potential than cytosine bases [6]. The regular arrangement of similar nucleotides in the chain under consideration allows us to estimate the maximum mobility value, which is a limiting one for irregular sequences. In modeling the transfer process, we consider nucleotide sequences as a system of sites in which each site corresponds to a pair of bases. The Hamiltonian H of charge transfer along a chain of sites has the form [7–9]

$$H = H_e + T_K + U_P, \tag{1}$$

$$H_e = \sum_i \alpha_i a_i^+ a_i + \sum_{i,j} \nu_{i,j}(a_i^+ a_j + a_j^+ a_i),$$

$$\alpha_i = \alpha_i^0 + \alpha_i' u_i,$$

$$T_K = \sum_i M_i \dot{u}_i^2/2, \quad U_P = \sum_i K_i u_i^2/2,$$

where H_e is the Hamiltonian of a hole, a_i^+ and a_i are the operators of hole creation and annihilation at the ith site, α_i is the energy of a hole at the ith site, $\nu_{i,j}$ are the matrix elements of the transition from the ith to the jth site, T_K is the kinetic energy of the sites, M_i is the mass of the ith site, u_i is the displacement of the ith site from its equilibrium position, U_P is the potential energy of the sites, K_i are elastic constants. We assume that the energy of a hole at the sites is a linear function of displacements of the sites u_i from their equilibrium positions, and α_i' is the hole–site displacement coupling constant; $i = 1, \ldots, N$; and N is the number of sites in the chain.

Choosing the hole wave function $|\Psi\rangle$ in the form

$$|\Psi\rangle = \sum_{n=1}^{N} b_n |n\rangle, \tag{2}$$

where b_n is the probability amplitude of finding a hole at the nth site, from Hamiltonian (1) in the nearest neighbor approximation, we obtain the following equations of motion [8, 9]:

$$i\hbar \frac{db_n}{dt} = (\alpha_n + \alpha_n' u_n) b_n + \nu_{n,n+1} b_{n+1} + \nu_{n-1,n} b_{n-1}, \tag{3}$$

$$M_n \frac{d^2 u_n}{dt^2} = -K_n u_n - \gamma_n \frac{du_n}{dt} - \alpha_n' |b_n|^2 + A_n(t). \tag{4}$$

Equations (3) are the Schrödinger equations for the probability amplitudes. To take into account dissipation processes in the classical equations of motion for site displacements (4), we added the term $-\gamma_n \dot{u}_n$, where γ_n is the friction coefficient, and the random force $A_n(t)$ with the following statistical properties:

$$\langle A_n(t) \rangle = 0,$$
$$\langle A_n(t) A_m(t + t') \rangle = 2k_B T \gamma_n \delta_{nm} \delta(t'), \tag{5}$$

where T [K] is temperature; that is the motion of the sites described by the Langevin equation.

When modeling the motion of holes in a GG…G sequence, we assumed the same values of the parameters as in [9]: $\alpha_n^0 = 0$, $\omega_n^2\tau^2 = 0.0001$, where $\omega_n^2 = K_n/M_n$, $\alpha_n' = 0.02\sqrt{M_n\hbar/\tau^3}$ (for $M_n = 10^{-21}$ g, respectively, $\alpha_n' \approx 1.3 \times 10^{-4}$ eV/Å), $\tau = 10^{-1}$ s. The matrix elements were taken from [10], $\nu_{n,n\pm1} = 0.084$ eV.

The scheme from [11] was used for the numerical integration of the Cauchy system reduced to a dimensionless form. In the calculations, the normalization condition was accurate to three significant figures: $\left|\sum |b_n|^2 - 1\right| < 0.001$. The initial conditions for the site displacements and velocities were taken according to the equilibrium distribution for the specified temperature; at the initial instant of time, the charge was considered to be localized at the middle of the chain consisting of 99 sites (at the 50th site). Various values of the friction coefficient $\omega_n' = \tau\gamma_n/M_n$ were considered. The results given below were obtained for $\omega_n' = 0.03$, $\omega_n' = 0.006$ (as in [9]), and $\omega_n' = 0.001$.

For each value, the calculation was performed for 1000 realizations at the specified temperature T = 300 K for a time of 2 ps.

The coefficients $b_n(t)$ found in this way were used for the calculation of the mean-square hole displacement $X^2(t)$

$$X^2(t) = \langle\Psi(t)|n^2a^2|\Psi(t)\rangle = \sum_n |b_n(t)|^2 n^2a^2, \quad (6)$$

where a is the distance between neighboring sites ($a \approx$ 3.4 Å).

The time dependence of the mean-square hole displacement (averaged over 1000 realizations) is shown in Fig. 1 for the case of $\omega_n' = 0.006$ on the interval of 2 ps. In the initial part of this interval (<0.02 ps), the ballistic regime of hole motion is observed, at which $X^2(t) \approx t^2$ (Fig. 2). After ~ 0.2 ps, the time dependence of the mean-square displacement can be considered linear. At $t \geq 2$ ps, the effects associated with the finiteness of the chain under consideration become notable.

For the homogeneous chain considered in this work, the hole mobility can be found by the Kubo equation [12]

$$\mu(\Omega) = -\frac{e\Omega^2a^2}{2k_BT}, \mathrm{Re}\left[\int_0^\infty \langle X^2(t)\rangle \exp(-i\Omega t)dt\right], \quad (7)$$

where e is the electron charge, Ω is the angular frequency of the alternating electric field, T is temperature (K). $\langle X^2\rangle$ designates ensemble averaging (in our case, over 1000 realizations). In the steady-state case, the following expression follows for the mobility from Eq. (7): $\mu = eD/k_BT$, where $D = \langle X^2(t)\rangle/2t$ is the diffusion coefficient determined by the slope of the straight line approximating the dependence $\langle X^2(t)\rangle$ in the interval [0.2, 2] ps (Fig. 1). At the selected values of parameters, the hole mobility equals $\mu \cong 2.4$ cm^2 V^{-1} s^{-1} for $\omega_n' = 0.001$, $\mu \cong 2.3$ cm^2 V^{-1} s^{-1} for $\omega_n' = 0.006$, and $\mu \cong 2$ cm^2 V^{-1} s^{-1} for $\omega_n' = 0.03$. Note that the hole mobility in a homogeneous G–C chain was found to be equal to $\mu \cong 10$ cm^2 V^{-1} s^{-1} in [13] (on the time interval of the same order). The higher mobility value is apparently associated with the fact that dissipation was not included in the model system considered in [13].

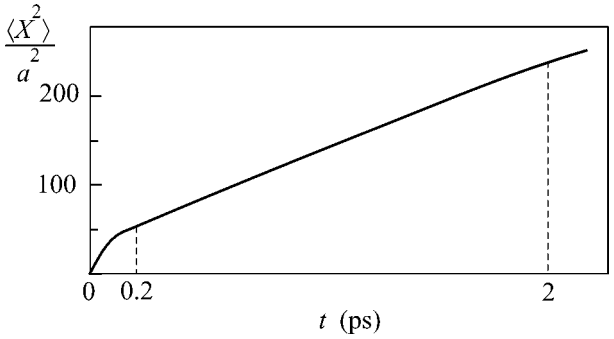

Fig. 1. Plot of the time dependence of the mean-square hole displacement on the interval of 2 ps.

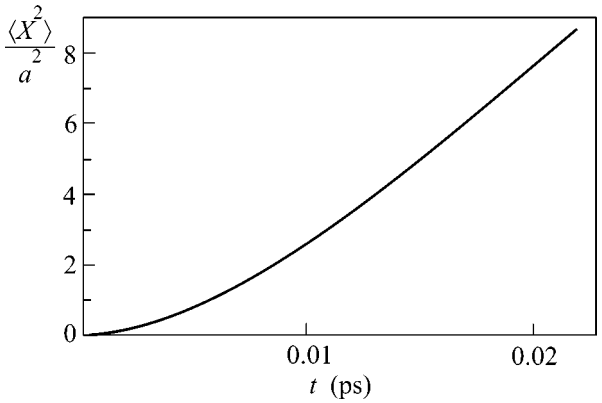

Fig. 2. Plot of the time dependence of $\langle X^2\rangle/a^2$ at small values of t.

Despite the not-too-high mobility value, the holes in DNA can be transferred for long distances, because the main mechanism of their capture in the process of transfer along the nucleotide sequence is the chemical reaction of a hole with water, whose rate is $K_{reac} \approx 10^6$ s^{-1} [14]. This leads to the following estimate for the distance at which a hole can be transferred before it is cap-

tured by water: $l = \sqrt{2D/K_{reac}}$. With the use of the results obtained, we find $l \approx 5 \times 10^4$ Å.

This work was supported by the Russian Foundation for Basic Research, project nos. 01-07-90317 and 03-04-49225.

REFERENCES

1. F. D. Lewis, R. L. Lestinger, and M. R. Wasielewski, Acc. Chem. Res. **34**, 159 (2001).
2. B. Giese, Acc. Chem. Res. **33**, 631 (2000).
3. P. F. Barbara and E. J. Olson, Adv. Chem. Phys. **107**, 647 (1999).
4. G. B. Schuster, Acc. Chem. Res. **33**, 253 (2000).
5. C. Dekker and M. A. Ratner, Phys. World **14**, 29 (2001).
6. F. D. Lewis and Y. Wu, J. Photochem. Photobiol. **2**, 1 (2001).
7. V. Mujica, M. Kemp, and A. Ratner, J. Chem. Phys. **101**, 6849 (1994).
8. V. D. Lakhno, *Computers and Supercomputers in Biology*, Ed. by V. D. Lakhno and M. N. Ustinin (Inst. Komp'yut. Issled., Moscow–Izhevsk, 2002), p. 137.
9. N. S. Fialko and V. D. Lakhno, Phys. Lett. A **278**, 108 (2000).
10. A. A. Voityuk, N. Rösch, M. Bixon, and J. Jortner, J. Phys. Chem. **104**, 9740 (2000).
11. H. S. Greenside and E. Helfand, Bell Syst. Tech. J. **60**, 1927 (1981).
12. J. C. Dyre and T. B. Schroder, Rev. Mod. Phys. **72**, 873 (2000).
13. F. Grozema, L. D. A. Siebbeles, Y. A. Berlin, and M. Ratner, Chem. Phys. Chem. **3** (6), 536 (2002).
14. F. D. Lewis, X. Liu, J. Liu, *et al.*, Nature **406**, 51 (2000).

Translated by A. Bagatur'yants

JETP Letters, Vol. 78, No. 5, 2003, pp. 339–341. Translated from Pis'ma v Zhurnal Éksperimental'noĭ i Teoreticheskoĭ Fiziki, Vol. 78, No. 5, 2003, pp. 789–791.

Electronic Structure of the Surface of Rare Earth Metals

V. A. Gerasimov and V. V. Gerasimov

Institute of Atmospheric Optics, Siberian Division, Russian Academy of Sciences, Tomsk, 634050 Russia

Tomsk State University, Tomsk, 634050 Russia

Received August 7, 2003

A qualitative model describing the surface of rare earth metals with an uncompleted 4*f* electron shell (Ce–Yb) and the process of thermal evaporation from this surface is proposed. The model is based on a correlation established between the energies of the lowest-lying levels of the $4f^{N-1}5d6s^2$ configuration and the temperatures of equal saturated-vapor pressures of these metals. © *2003 MAIK "Nauka/Interperiodica"*.

PACS numbers: 73.20.-r; 64.70.Hz; 71.20.Eh

Investigation of the surface properties of metals, including the electronic structure of the surface layer, is an important field in solid state physics. A number of methods used for the investigation of solid surfaces are based on probing the surface with a particle beam or radiation. One of these techniques is associated with the photoevaporation effect that was originally reported in [1], where exposure of a sodium film to optical radiation led to an emission of neutral metal atoms that was not related to thermal evaporation. The photoevaporation phenomenon was further studied (including other metals) in [2, 3], where a similar effect was observed for a cesium film.

The photoevaporation phenomenon was characterized by the following experimental facts:

(i) The photodetachment process is associated with the presence of certain structural defects on the metal surface. These defects represent separate atoms (adatoms) that are less strongly bound to the metal surface than the surface atoms are with each other. The number n of such defects, determining the photoevaporation process, depends exponentially on the temperature: $n = N\exp(-E/kT)$, where N is the total number of surface atoms and E is the energy of formation of such defects with allowance for the entropy factor (200 cm^{-1}).

(ii) The photoevaporation rate (w), defined as the reciprocal time it takes for reducing the Na film thickness by half, grows with decreasing radiation wavelength (i.e., with increasing excitation energy) under isothermal conditions, linearly increases with the radiation power, and exponentially depends on the temperature as $w \sim \alpha\exp(-\Delta E/kT)$, where $\Delta E = 1000 \pm 200$ cm^{-1}.

Based on these results, Bonch-Bruevich *et al.* [3] developed a qualitative model of the surface layer and proposed a mechanism explaining the photodetachment of intrinsic sodium atoms.

Matthew *et al.* [4] showed that electron emission from the surface of metallic calcium bombarded by inert gas ions is caused by the decay of neutral excited atoms occurring in the $3p^5 3d 4s^2$ state. This result suggests that neutral calcium atoms in this excited state are present on the sample surface.

As is known, the subgroup of rare earth metals (REMs), which represent chemically identical elements, exhibits a significant scatter in the energy required for atom detachment from the surface, even for the neighbors in the Periodic Table (e.g., gadolinium vs. europium). Taking into account the results described above, we suggested that the REM surface, similar to calcium, contains neutral atoms in the excited state and that these atoms account for the evaporation process. The detachment energy of an REM atom from the surface is related to the excitation energy of these atoms [2, 3].

In order to check for this hypothesis, we attempted to establish correlation between the temperatures of equal saturated-vapor pressures of REMs (i.e., the energies of atom detachment from the surface) and the level excitation energies of various electronic configurations. There are many papers devoted to the search for correlations between various properties of metals and their atomic numbers (see, e.g., [5]). In REMs, such correlations were established between thermodynamic and spectroscopic properties [6, 7]. These data facilitated the search for the aforementioned correlation.

We have analyzed the data for a large number of levels belonging to various electronic configurations for both atoms and ions. The analysis was based on the data presented in [8–11]. As a result, we established that the only configuration correlated to the characteristic behavior of the temperatures of equal saturated-vapor pressures of REMs is $4f^{N-1}5d6s^2$.

A plot of the temperature of equal saturated-vapor pressures (P_{sat} = 1.0 Torr) of REMs is given in Fig. 1.

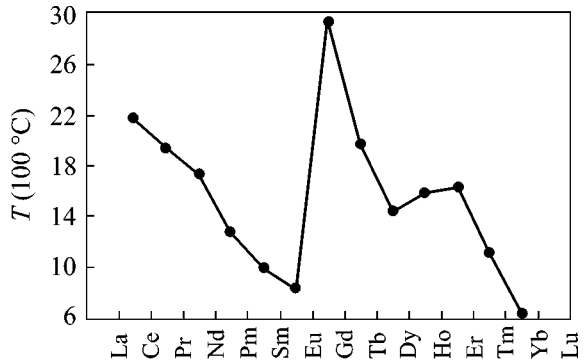

Fig. 1. Plot of the temperature of equal saturated-vapor pressures versus atomic number in the REM subgroup (P_{sat} = 1.0 Torr).

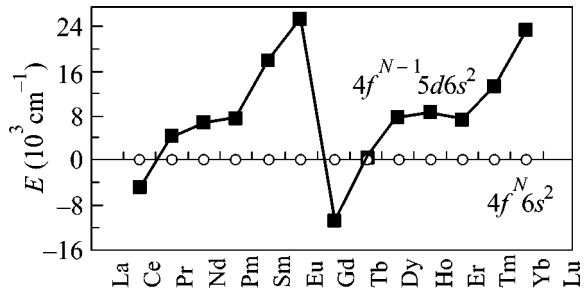

Fig. 2. The energies of the lowest-lying levels of the $4f^{N-1}5d6s^2$ configuration relative to the energies (taken as zero) of the $4f^N6s^2$ configuration.

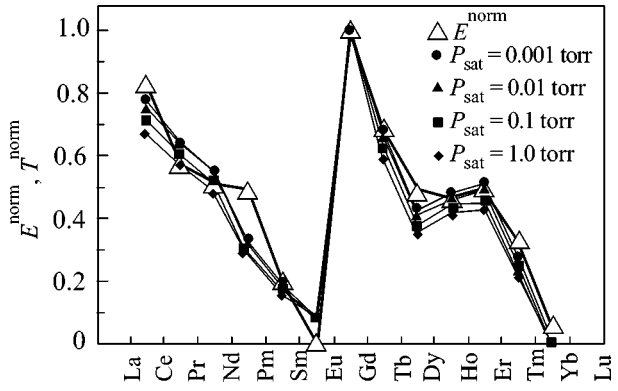

Fig. 3. The inverted and normalized graph of energies presented in Fig. 2, in comparison to the normalized temperatures of equal saturated-vapor pressures versus element number for four values of the saturated-vapor pressure.

Figure 2 gives the energies of the lowest-lying levels of the $4f^{N-1}5d6s^2$ electronic configuration relative to the energies (taken as zero) of the $4f^N6s^2$ configuration. Figure 3 presents the inverted and normalized graph of the corresponding energies, $E^{norm} = 1 - (E - E_{min})/(E_{max} - E_{min})$, in comparison with the curves for the normalized temperature of equal saturated-vapor pressures, $T_p^{norm} = (T_p - T_{p^{min}})/(T_{p^{max}} - T_p^{min})$, versus element number for four values of the saturated-vapor pressure. The curves in Fig. 3 were normalized using the values of E, E_{max}, and E_{min} representing the level energies of an arbitrary element and the highest and lowest energies in the subgroup under consideration, respectively. The values of T_p, $T_{p^{max}}$, and $T_{p^{min}}$ are the temperatures of equal saturated-vapor pressures of an arbitrary element and the maximum and minimum temperatures among all elements of the subgroup, respectively.

The observed correlation implies that the T_p value for any element of the REM subgroup is determined by E_{min}^k, the energy of the lowest-lying level of the $4f^{N-1}5d6s^2$ configuration of this element:

$$T_p = f[E_{min}^k(4^{N-1}5d6s^2)].$$

The higher the level energy, the lower the T_p (and the energy of atom detachment from the surface). Note that Ce and Gd, for which this configuration corresponds to the ground state, are characterized by the maximum values of T_p.

Summarizing the above results, we have drawn the following conclusions:

(i) The intrinsic neutral REM atoms in the indicated states occur on the ionic surface and determine the thermal evaporation process, similar to the structural defects (adatoms) determining photoevaporation from the sodium surface [2, 3].

(ii) The mechanisms of the formation of structural defects in sodium and neutral atoms in the $4f^{N-1}5d6s^2$ electronic state on the REM surface are identical and show thermal character.

(iii) Evaporation from the REM surface is a two-stage process, involving the formation of a neutral atom in the $4f^{N-1}5d6s^2$ state on the surface followed by the thermal detachment.

It should be noted that, at a saturated-vapor pressure of P_{sat} = 0.001 Torr, most REMs (except for Gd, Nd, Pr, Tb, and Ce) occur in the solid state, while at P_{sat} = 1.0 torr only three elements (Yb, Sm, and Tm) remain solids. However, this circumstance does not influence the correlation presented in Fig. 3. This fact is indicative of the identical character of processes involved in the formation of atoms in the states determining evaporation from both liquid and solid phases.

An experimental verification of the model may consist in the observation that in thullium, for example, of the atomic transition line at a wavelength of 762.0 nm on the background of the continuous spectrum of the vacuum-heated sample. This line corresponds to the transition from the lowest level of the P_{sat} configuration with an energy of 13119 cm^{-1} to the ground state. Note that this transition is allowed by the selection rules.

We are grateful to Prof. G.F. Karavaev and Prof. V.G. Bagrov for fruitful discussions and critical remarks.

REFERENCES

1. I. N. Abramova, E. B. Aleksandrov, A. M. Bonch-Bruevich, *et al.*, Pis'ma Zh. Éksp. Teor. Fiz. **39**, 172 (1984) [JETP Lett. **39**, 203 (1984)].
2. A. M. Bonch-Bruevich, Yu. N. Maksimov, S. G. Przhibel'skiĭ, *et al.*, Zh. Éksp. Teor. Fiz. **92**, 285 (1987) [Sov. Phys. JETP **65**, 161 (1987)].
3. A. M. Bonch-Bruevich, T. A. Vartanyan, Yu. N. Maksimov, *et al.*, Zh. Éksp. Teor. Fiz. **97**, 1761 (1990) [Sov. Phys. JETP **70**, 993 (1990)].
4. J. A. D. Matthew, M. A. Gallon, and T. E. Gallon, Phys. Rev. B **55**, 2697 (1997).
5. V. S. Arakelyan, Dokl. Akad. Nauk **364**, 67 (1999).
6. L. Brewer, J. Opt. Soc. Am. **61**, 1101 (1971).
7. V. I. Spitsyn and G. V. Ionova, Dokl. Akad. Nauk SSSR **285**, 945 (1985).
8. A. I. Efimov, L. P. Belorukova, I. V. Vasil'kova, *et al.*, *Properties of Inorganic Compounds: Handbook* (Khimiya, Leningrad, 1983).
9. J. F. Wyart, J. Opt. Soc. Am. **68**, 197 (1978).
10. W. C. Martin, R. Zalubas, and L. Hagan, Natl. Stand. Ref. Data Ser. (U.S. Natl. Bur. Stand.) **60** (1978).
11. L. Brewer, J. Opt. Soc. Am. **61**, 1666 (1971).

Translated by P. Pozdeev